Metalens Integrated Photonics

by

Ramin Yazdaanpanah

A Dissertation Submitted to the
Graduate School of Sciences and Engineering
in Partial Fulfillment of the Requirements for
the Degree of

Master of Science

in

Materials Science Engineering

KOÇ ÜNİVERSİTESİ

August 10, 2021

Metalens Integrated Photonics

Koç University

Graduate School of Sciences and Engineering

This is to certify that I have examined this copy of a master's thesis by

Ramin Yazdaanpanah

and have found that it is complete and satisfactory in all respects,
and that any and all revisions required by the final
examining committee have been made.

Committee Members:

_____

Assist. Prof. Serap Aksu Ramazanoğlu (Advisor)

_____

Prof. Ali Serpengüzel

_____

Assoc. Prof. Mustafa Türkmen

Date: _____

*To my **"Family"** that are the most precious ones in my life*

ABSTRACT

Metalens Integrated Photonics
Ramin Yazdaanpanah
Master of Science in Materials Science Engineering
August 10, 2021

This thesis investigates the optical metasurfaces utilized for lensing (metalens) and their potential to integrate with photonic circuits. In recent years, a plethora of studies have been done on metalenses, especially in the visible region. However, there are still rooms to discover the metalenses working in the mid-IR and ultraviolet (UV) spectra. Due to the applications in these regions, from biosensing in mid-IR to lithography in UV, the development of metalenses operating in these ranges is essential. One aspect of metalenses that requires further investigation is to analyze the deviation of the measured focal spot from the simulated value, which can affect the focusing quality. As this deviation becomes smaller, a more homogeneous airy-disk pattern can be achieved. Unlike the previous studies that have suggested the Fresnel number is the only relevant factor for the possible focal shift, we numerically show that for mid-IR metalenses, the numerical aperture (NA) of metalenses is an essential parameter to predict the focal spot deviation from the simulated value. We also introduce a critical NA (between 0.55-0.65) in which the deviation of the simulated and measured focal spot can reach zero value. The other aspect of metalenses addressed in this thesis is to find a fine-tuning method to multiply the number of focal sites, which is a practical concept for polarization filtering applications. The single-material-base metalenses are numerically investigated in the UV regime. Moreover, a design method to have full spatial control on phase, polarization, and focal spots is carefully implemented to attain multifocal metalenses. These single-material metalenses are composed of Al_2O_3 nanoblocks on the Al_2O_3 substrates, which can facilitate the fabrication process.

Finally, by taking advantage of focal shift prediction and multifocal design principle, we propose a metalens-integrated photonic device. On one side of such device, a metalens structure is incorporated, and a plasmonic antenna array is patterned on its other side. We numerically study this device and show that this new compact

design could offer an excellent lens-free illumination mechanism for plasmonic structures. Also, as it is possible to focus the incident light on the plasmonic structure, the near field intensity is significantly increased in this device. In addition, utilizing multifocal metalenses on the backside also allows us to illuminate multiple chips on the surface with different polarization modes. Considering the plasmonic structure applications for biosensing purposes, we can increase the sensitivity and selectivity of biodetection in these integrated devices while avoiding complicated measurement techniques.

ÖZETÇE

Metalens Tümleşik Fotonik
Ramin Yazdaanpanah
Malzeme Bilimi ve Mühendisliği , Yüksek Lisans
10 Ağustos 2021

Bu tezde optik metayüzeyleri kullanarak ışığı odaklayıcı minyatür mercekler, metalensler geliştirilmiş ve bu metalenslerin fotonik devrelerle bütünleşme olasılığı incelenmiştir.

Son yıllarda özellikle görünür bölgede metalensler üzerine çok sayıda çalışma yapılmıştır. Bununla birlikte, orta kızılötesi (mid-IR) ve morötesi (UV) spektrumlarında çalışan metalenslerin geliştirilmesi kısıtlı kalmıştır. Ölçülen odak noktasının odaklamanın niteliğini etkileyebilecek biçimde benzeştirilen değerden sapması metalenslerin gerçekleştirilmesinde önemli bir sorundur. Bu sapma küçüldükçe, daha homojen Airy disk odaklama modeli elde edilebilir. Fresnel sayısının olası odak kayması için tek ilgili etken olduğunu öne süren önceki çalışmalardan farklı olarak, orta IR metalensler için metalenslerin sayısal açıklığının (NA) odak noktası sapmasını öngörmek için önemli bir değişken olduğunu sayısal olarak gösterdik. Ayrıca, tasarlanan odak noktasının ölçülenden sapmasının sıfıra yaklaştığı ayırgan bir NA (0,55-0,65 arasında) önerildi.

Bu tezde ele alınan metalenslerin diğer yönü, kutup süzme uygulamaları için kullanışlı odak noktası sayısının çoğaltılabilmesidir. Tek malzemeden oluşturulan metalensler UV sıklıkta sayısal olarak araştırılmıştır. Al_2O_3 alttaş ve nanobloklardan oluşan çok-odaklı metalens elde etmek için evre, kutuplama ve odak noktaları üzerinde tam uzamsal yönetime sahip bir tasarım yöntemi geliştirildi. Tek malzemeden oluşan metalenslerin en önemli özelliği kırılma katsayısı farklılığı bile olmadan ilginç optik özelliklerin kısa bir üretim süreciyle elde edilebilmesidir.

Son olarak, odak kayması tahmini ve çok odaklı tasarım ilkesinden yararlanarak, metalens ile entegre bir fotonik devre oluşturuldu. Cihazı oluşturan alttaşın bir tarafında metalens yapısı, diğer tarafında bir plazmonik anten dizisi modellendi. Bu yeni sıkı tasarımın plazmonik yapılar için olgun bir lenssiz odaklama mekanizması sunabileceğini gösterdik. Gelen ışığı plazmonik yapıya odaklamak mümkün

olduğundan, bu aygıtta yakın alan şiddetin önemli ölçüde attığı gözlenmiştir. Ayrıca çok odaklı metalens kullanmak, yüzeydeki çoklu yongaları farklı kutuplama kipleri ile aydınlatmamıza da olanak tanır. Biyoalgılama amaçlı plazmonik yapı uygulamalarında yakın alan şiddetinin önemi düşünüldüğünde, karmaşık ölçüm tekniklerinden kaçınırken bu entegre aygıtlarda biyoalgılamanın duyarlılığını ve seçiciliğini artırabiliriz.

ACKNOWLEDGMENTS

First of all, I want to express my great appreciation to my advisor, Prof. Serap Aksu Ramazanoğlu, for all her supports and helps during my master's period. Not only has she been an excellent thesis advisor to me, but also I learned many things from her about morality and academic behaviors. Although this pandemic made everything unexpected and postponed, her encouragement and patience created a situation for me to have maximum focus on my research. She is very sympathetic, and I really appreciate her guidance and trust during these two years. I feel lucky that I had this chance to pursue my master's under her supervision, which was an excellent opportunity for me to find my way and learn new things with her kind assistance. I am grateful for all the support I received and the knowledge she kindly shared with me, which makes this thesis possible.

After that, I should deeply acknowledge my labmate, Farhan Ali (Ph.D. student at Imec), for his help and support during these two years. I learned many things from him, and I sincerely appreciate his help and knowledge-sharing, which significantly paved the way to write this thesis. Also, I should appreciate Dr. Semih Korkmaz (Assist. Prof. at Bandırma Onyedi Eylül Üniversitesi) for his honest assistance and advice in this thesis.

I would like to thank some of my friends that supported me incredibly during these years. They have had a significant role in my life, especially in this pandemic situation, which they helped me to keep the focus on the research. So I want to express my deep gratitude to Mr. Farzin Negahbani, Mr. Javad Bathaei, Mr. Yousef Sadeghie, Mr. Amirhossein Sayar, Mr. Sina Zare Pakzad, and Mr. Morteza Hosseini for all their supports in these two years. This thesis was hard to reach without them at this time. More importantly, I should appreciate my uncles, Dr. Mehdi Yazdaanpanah and Dr. Mehdi Hosseini that were like brothers to me, and I

always use their advice in my life and research.

In the end, I should thank the most precious ones in my life, my family, for all their supports. Words are not enough to express my acknowledgment to them, but I want to emphasize their vital role in everything I have.

Also, I should appreciate The Scientific and Technological Research Council of Turkey (TÜBİTAK) that provided financial supports for me.

TABLE OF CONTENTS

LIST OF TABLES

LIST OF FIGURES

ABBREVIATIONS

CMOS	Complementary Metal–Oxide–Semiconductor
DOF	Depth of Focus
EM	Electromagnetic
FDTD	Finite Difference Time Domain
FE	Focusing Efficiency
FWHM	Full Width Half-Maximum
LCP	Left Circular Polarized
LP	Linear Polarized
NA	Numerical Aperture
OMs	Optical Metasurfaces
PCE	Polarization Conversion Efficiency
RCP	Right Circular Polarized

Chapter 1

INTRODUCTION

1.1 Overview

Recent developments in photonics and optics have arisen due to advances in micro-nano fabrication methods in the last decade. These methods, as well as advanced monitoring and understanding of wave-matter interaction, pave the way for manipulation and controlling the flow of light in paths that were not possible before [5, 6]. This miniaturization increasingly grows the utilization of nanophotonic devices instead of former bulky-conventional versions [7].In this regard, not only the efficiency of optical devices increased, but also a plethora of new practical applications emerged in the field of nanophotonics [8].

Optical metasurfaces (OMs) are nanophotonic structures that have sub-wavelength thickness and can strongly interact with light. OMs are artificial nanostructure that manipulate the light properties such as its polarization, wavefront, distribution or spectrum over a sub-wavelength dimensions [9, 10, 11] Nowadays, these OMs have very widespread applications in lenses [12, 13], polarization controller [14], beam forming devices [15], reflection/refraction controller [16], holography [17], and perfect absorbers [18], to name a few.

Metalenses are one of the most applicable dielectric metasurfaces. Over the past few years, many studies have been done in this field, especially in the visible region. However, the existing mid-IR technologies ranging from thermal imaging, vibrational spectroscopy to optical cloaking [19, 20] and also the applications in the UV range, including lithography, imaging, spectroscopy, and quantum information processing [21], are prone to substantial advancements by utilizing of planar dielectric metalenses in these ranges. This thesis aims to investigate mid-IR and UV metalenses

and the applicability of integration of metalenses with other photonic structures. Hence, first, the focal shift effect in the metalenses operating in the mid-IR range is investigated. The focal shift refers to the deviation of simulated and designed focal length, which happens in the metalenses. Here, we will show the importance of NA to predict the value of focal shift. In the following, a single material metalens with a particular phase controlling technique is proposed that presents a multifocal focusing pattern in the UV range. These multifocal metalenses can offer an excellent opportunity to operate as polarization filters. It is worth mentioning that the fabrication process of these single materials metalenses is more straightforward than those that have different materials for nanoblocks and substrates.

We continue our discussion by introducing an integrated device constituent of plasmonic structures and metalenses in one chip and numerically investigating the effectiveness of this integrated device. Here, the importance of multifocal pattern and focal shift effect will clearly emerge. This metalens-plasmonic structures integration system presents a lens-free illumination strategy with higher near field enhancement. Also, utilizing multifocal metalens in this system allows us to illuminate multi chips on a surface with different polarization modes.

1.2 Metamaterials

The interaction between electromagnetic waves and materials is almost the basis of all electromagnetic phenomena. Therefore, to have a better realization of possible ways to manipulate the wave-matter interactions, it is crucial to deliberate the nature of the electromagnetic properties of the material. In other words, the functionality and variety of many electromagnetic devices are limited to the materials utilized to build them. However, due to some material constraints, sometimes it is very challenging to achieve the desired properties. For example, one of the obvious constraints that we are always dealing with is the light propagation speed. The optical pulses cannot travel faster than free space in any medium [22].

There are several approaches to overcome the constraints arisen from materials. The conventional method was to synthesis new materials at the molecular level with

unique properties. For example, Teflon (polytetrafluoroethylene) is one of those materials with a very low refractive index, and it has numerous optical applications. However, there is also another approach that is very widespread nowadays. In this novel method, the artificially structured composite materials are designed, which are constituted of well-arranged functional inclusions with subwavelength dimensions. These kinds of materials are called **metamaterials**. The word "meta" is taken from Greek, which means "beyond" [22, 23], and it defines the materials that their properties are beyond conventional materials. The electromagnetic properties of the metamaterials can be tuned in different ways with precise control of impinging electromagnetic waves [24, 25]. Plasmonic perfect absorbers, Energy harvesting and Imaging technologies., are among some of the applications of these metamaterials in which the interaction between material and Electromagnetic waves are manipulated accurately. There are different kinds of metamaterials. Some metamaterials show a negative refractive index which can be used for novel applications such as flat lenses. On the other hand, some metamaterials are designed to have a high surface impedance which can be achieved by precise geometry control. For example, perfect absorption can occur when effective surface impedance ($Z_{eff}=\sqrt{\frac{\mu_{eff}}{\varepsilon_{eff}}}$ gets a similar value to the free space impedance ($Z_{eff}= 1$) at some certain frequency [26]. The concept of metamaterials emerged two decades ago, and nowadays, it is utilized for various applications ranging from electromagnetic and optical to mechanical and transport properties [27]. Here our focus is on optical metamaterials.

1.3 Optical Metasurfaces

Optical metasurfaces (OMs) are considered as 2D metamaterials, which are consisted of subwavelength thickness elements on planar surfaces. OMs exploit nanostructures scattering phenomena to control and manipulate the light in the desired way, and they can adjust different properties of light such as polarization, wavefront, intensity distribution, or spectrum [28, 29]. In contrast with conventional optics that relies on propagation and refraction of light, in the OMs, the meta-atoms resonantly capture and reradiate the incident light [8]. Metasurfaces can be classified in several manners.

They can be categorized based on their materials operation's mode (transmission Vs. reflection), the way that they obtain their functionality (e.g., geometric Vs. resonance phase response), and the materials used as meta-atom on the surface (metallic/plasmonic Vs. dielectric)[12, 30].

The meta-atoms in plasmonic metasurfaces are from metallic particles with special geometries, and they take advantage of the plasma oscillation of metallic particles on their surface. These OMs consist of periodic or distributed resonant metallic arrays of nanoantenna on the surface, and they can confine the light into the sub-wavelength structures [31, 5]. Plasmonic metasurfaces' light scattering properties are mostly related to the shape and dimension of metallic meta-atoms on the surface. Plasmonic metasurfaces are very applicable for perfect absorbers [24], biosensing purposes [32] and optical vortex [33].

Although the plasmonic OMs produce great light confinement, due to the lossy nature of plasmonic metasurfaces, the high refractive index plasmonic OMs are introduced to increase the efficiency. Also, the plasmonic OMs usually use noble metals such as gold or silver as metallic particles on the surface, which imposes higher costs and more complexity in the fabrication process [34]. Therefore, the dielectric OMs, which utilize the materials such as titanium dioxide, germanium, silicon, and tellurium, can modify the light properties in a more efficient method [8, 28, 30]. Over the past few years, dielectric OMs have become very popular for photonics applications, especially in transmission mode. The applications of dielectric OMs in metalenses, holograms, polarization optics, and beam shaping devices can be promising evidence for their possible vast future applicabilities [8].

The OMs opened a new path to light modification in comparison with conventional optics, and they made the inspiration to introduce the field of flat optics [35]. The OMs provide a range of advantages in comparison with bulky optics. Employing the OMs, one can engineer to shape the light wavefront at a distance much less than the wavelength from the interface. Hence when light is transmitted or reflected from the OMs, more extensive and more controllable modification can be applied on the incident beam through the meta-atom scatterer [19]. On the other hand, the OMs offer an opportunity to go beyond wavelength resolution and allow us to control the

phase, amplitude, and polarization of light in the order of subwavelength resolutions. The subwavelength resolution makes it possible to focus all the illumination's optical power into a single useful beam. More importantly, in flat optics, the interaction of meta-atoms can be engineered with both electric and magnetic field components of the light. Hence, the optical impedance of the surface can be adjusted, and by matching this value with the impedance of free space, a highly efficient transmitting array can be achieved with a minimum reflection value [19, 36].

1.4 Metalenses

Although conventional lenses are beneficial in our daily life, they are usually bulky, heavy, expensive and their fabrication process is almost old. Thanks to miniaturization development in recent years, the OMs base lenses, called metalenses, are introduced, and they offer an advantageous range of features for manipulating the incoming light [37]. The metalenses are flat optical components that can apply an abrupt change in the incident beam's phase, amplitude, and polarization. Same as other OMs, the metalenses are composed of many nanoblocks that are designed precisely on the substrate. As the distance between nanoblocks and their dimensions are much smaller than the incoming light's wavelength, they can form the optical wavefront to the desired shape with the subwavelength resolutions. This ability is feasible when the response of each nanoblock on the surface is different from the others to achieve the required phase mapping on the surface.

The required phase profile of a conventional to focus a collimated beam with the wavelength of λ is given by:

$$\varphi(R) = \pm k_0(f - \sqrt{R^2 + f^2}) \tag{1.1}$$

Here the k_0 is the wave vector of free space, and it is equal to $k_0 = 2\pi/\lambda$, and R is the distance from the center of the lens to each random point on the surface [38]. The required phase profile in the conventional lenses is achieved by gradual thickness variation in its structure. Fig.1.1(a) shows the schematic of a traditional lens with a positive focusing profile. As It can be seen, the thickness of the lens is not constant,

and it is changing to attain the required phase for the focusing. However, for the metalenses, the story is different [39, 37].

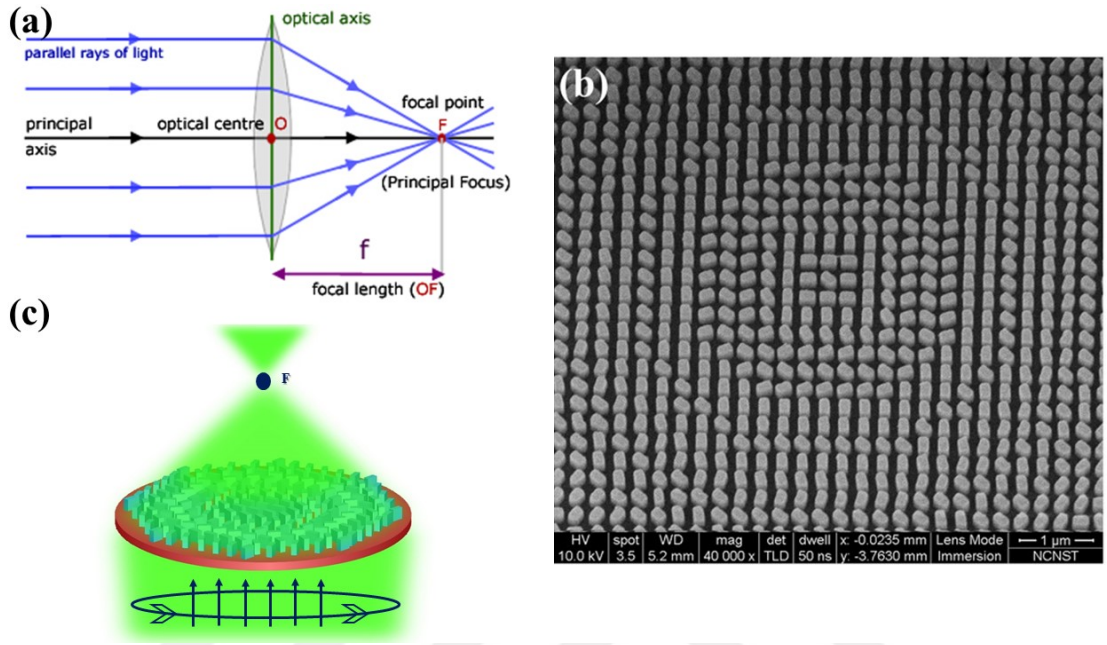

Figure 1.1: **a** The schematic of a conventional lens with positive focusing profile. **b** An SEM image of a metalens designed based on geometric phase method.**c** The schematic of focusing profile of a metlanes. **b** is taken from the [1] with permission.

The nanoblocks on the substrate are responsible for applying the required phase profile at each position on the surface. Hence the phase profile along the surface is imparted discretely. It means that we can rewrite the Eq.1.1 in the following way:

$$\varphi(x, y) = \pm k_0(f - \sqrt{x^2 + y^2 + f^2}) \tag{1.2}$$

Here the x and y are the position of each nanoblock on the surface. The Eq.1.2 confirms the fact that the response of each nanoblock on the surface should be different from the others. Fig.1.1 (b) shows a SEM image of a metalens. This lens is designed based on a geometric phase controlling system [28], which will be elaborated in the next chapter. Here the dimension of each nanoblock is the same as each other, and their orientations vary to impart the required phase. Changing the orientation of nanoblocks should cover the full phase range between 0-2π to satisfy the required phase profile at each position. On the other hand, the idea of creating the spatial

phase by utilizing the elements with different shapes and dimensions has been used since 1993. This idea becomes an origin for another phase engineering method called the propagation phase for designing the metalenses [28]. Here, the required phase to focus the light with metalenses is imparted by changing the dimensions of each nanoblock at each position [37]. Fig.1.1 (c) shows the schematic of metalens focusing system. While passing from the metalens structure, the incident light wavefront goes through the desired direction to be focused in the designed focal spot.

The new development in the metalens design and fabrication technology makes them one of the most useful metasurfaces over the past few years. The first types of metalenses were designed to operate at specific wavelengths. However, by advancement in design methods, nowadays, the operation bandwidth of metalenses has become wider, and they can focus a range of wavelengths without any chromatic aberration [40, 41, 42]. In addition to the thickness and weight decrements and chromatic correction, metalenses also can correct the spherical, coma, and astigmatism aberration in compression with conventional lenses [43]. Besides all these advantages, metalenses activate the option of focal spot manipulation. The position of focal points in x,y, and z directions can be set precisely designed with polarization selectivity. Also, by adjusting the phase profile on the metalens surface, the multifocal metalenses can be achieved [44, 45]. The more compatibility with CMOS fabrication line, focal lens tunnability and the capability of providing high numerical aperture focusing with high efficiency are the other advantages of metalenses [44].

1.5 Plasmonic Background

Plasmonics is a field of research that can be considered at the interface of photonics, electronics, and nanotechnology. By taking advantage of the collective oscillation of conduction electrons at the metals' surface (plasmons), the plasmonic structures provide an opportunity for light-matter interaction at sub-wavelength scales. Coupling of light with metallic structures at nanoscales dimensions, electromagnetic field enhancement, scattering, and absorption of light at the resonance frequency of the structure, are some of the advantages that plasmonics can offer. Due to

these remarkable properties, plasmonic antennas can be utilized as biosensors, photodetectors, absorbers, photocatalysts, and many more applications with excellent functionality [24, 46, 47]. In this thesis, we will integrate the metalenses with plasmonic structures as one of the essential photonic circuits. Hence, here a brief theory about plasmonic is presented.

As a result of irradiation of EM waves on noble metals, the conduction electrons cloud oscillates at the metal-dielectric interface, and the surface plasmons are excited. As a consequence of these oscillations, the charge distribution on the surface is changed continuously; therefore, a restoring force is induced on the surface. This force results in periodic collective oscillation of conduction electrons which is called surface plasmon resonance (SPR). SPR can be classified into two main groups: Surface Plasmon Polariton (SPP) and Localized Surface Plasmon Resonance (LSPR) [48, 49, 50]

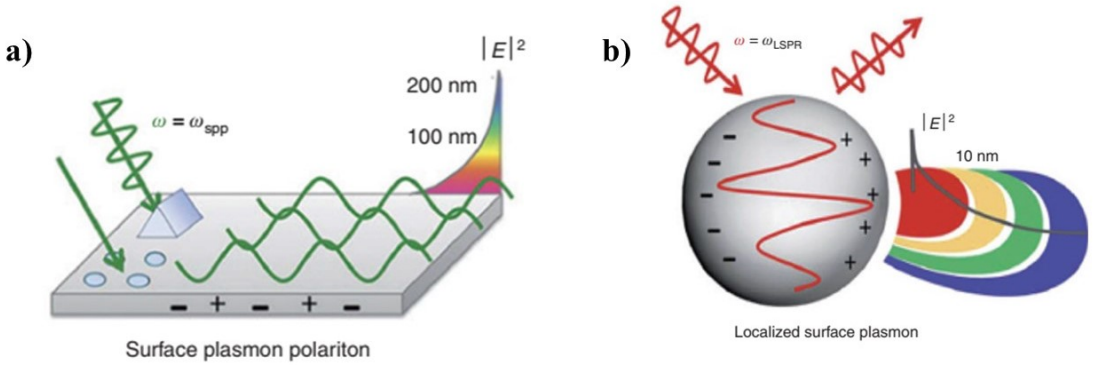

Figure 1.2: The schematic of Surface Plasmon Polariton (**a**) and Localized Surface Plasmon resonance(**b**). Taken with permission from [2].

The SPPs are non-stationary excitation modes, and they are EM waves that are propagating along with metal-dielectric interface (Fig. 1.2 (a)). Unlike the LSPs(Fig. 1.2 (b)) that are a kind of static excitation mode, SPPs cannot be excited directly by incident light due to the high momentum requirement. Hence, the prism coupling (Kretschmann configuration) and grating coupling (Periodic structures) techniques are used to overcome the momentum problem and help to excite the SPPs. On the other hand, LSPs can be directly excited by incident EM radiation

on metal nanoparticles. This direct excitation is due to the absorption and scattering phenomena that happen through the surface of the sub-wavelength sized conductive nanoparticles shown in figure1.2 (b). This type of resonance is highly dependent on the material, geometry, and the surrounding environment of the antenna [24, 51, 52].

Chapter 2

DESIGN AND PRINCIPLES OF SIMULATIONS

In this section, we introduce the principle associated with electromagnetic simulations. These principles are the basis for our following investigations in this thesis.

2.1 Finite difference time domain Solver

Finite-difference time-domain (FDTD) is a state-of-the-art analyzing method to model computational electrodynamics and solve Maxwell's equations numerically in complex geometries [53, 3]. FDTD, by taking advantage of Fourier transform, can offer to calculate a full range of valuable quantities from transmission and reflection of light to the complex Poynting vector. Unlike the Finite element method (FEM), in which analyses are based on frequency-domain, FDTD exploits of time-domain technique to solve electromagnetics (EM) equations. Therefore, for analyzing the properties of systems in a wide range of wavelengths, the FDTD is a more memory-efficient technique, and as a result, it is a well-appropriate method to investigate the interaction of EM waves with complex structures at a subwavelength scale.

FDTD solver, by considering the interaction between EM radiation and non magnetic materials, can solve the Maxwell's curl equations and constitutive equation in the system which are given by:

$$\frac{\partial \vec{D}}{\partial \vec{t}} = \nabla \times \vec{H} \tag{2.1}$$

$$\frac{\partial \vec{H}}{\partial \vec{t}} = -\frac{1}{\mu_0} \nabla \times \vec{E} \tag{2.2}$$

$$\vec{D}(\omega) = \epsilon_0 \epsilon_r(\omega) \vec{E} \tag{2.3}$$

Where $\vec{H}$, $\vec{E}$ and $\vec{D}$ are magnetic field, electric field, and electric displacement, respectively. Also, ϵ_0 is the permittivity of free space, and the ϵ_r (ω) is the complex

relative dielectric permittivity of the material. The value of ϵ_r (ω) is related to the refractive index of the material (n) and it is given as ϵ_r (ω)=n^2.

In three dimensions, both $\vec{E}$ and $\vec{H}$ have three components in the three axes. These vector components can be calculated by two sets of independent Maxwell equations, termed as transverse magnetic (TM) and transverse electric (TE). **TM** equations are composed of the $\vec{H}_x$,$\vec{H}_y$ and $\vec{E}_z$, and **TE** equations are composed of $\vec{E}_x$,$\vec{E}_y$ and $\vec{H}_z$. Then, If we consider that fields are independent of z, by assuming that the structure is infinite in the z direction, we can solve both TM and TE equations only in the x-y plane. Therefore, we can rewrite the equations with this assumption according to Eq.2.4 and Eq.2.5.

$$\frac{\partial \vec{E}}{\partial z} = \frac{\partial \vec{H}}{\partial z} = 0 \tag{2.4}$$

$$\epsilon_r(x, y, z, \omega) = \epsilon_r(x, y, \omega) \tag{2.5}$$

All of these equation can be solved in FDTD solver on a discrete spatial and temporal grid. Each of electric and magnetic field components mentioned above, can be solved within a grid cell in different locations. This grid cell is called Yee's cell (the scientist who first introduced the FDTD method), shown in Fig.2.1. After data collection, all the data calculated at different points within a Yee cell are interpolated at the origin of each grid point by default [54, 53, 3].

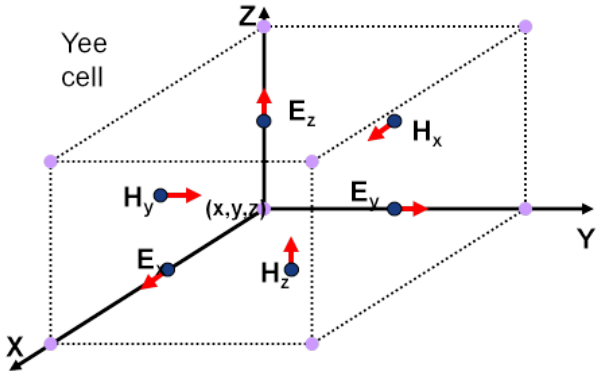

Figure 2.1: A Yee cell, showing how field components are solved at various points inside a grid cell [3]

2.2 Simulation Domain and Objects

To do our simulation, we are mainly using the Lumerical FDTD software. It is essential to design the simulation's parameters correctly to achieve the best accurate results from simulations. In this section, we overview the simulation's object we are dealing with in the FDTD environment. As we can deliberate to set the parameters more precisely, our simulations' results have higher Compatibility in comparison with what happens in reality.

2.2.1 General and geometry settings

First of all, in the simulation space, we should define an FDTD region. This FDTD region can be 2D or 3D, and its dimensions can be set in the geometry tab. In addition to the geometry, we can set the simulation time, temperature, and refractive index of the background. Despite the parameters related to the mesh setting, which will be explained following this section, there is another parameter called **auto-shut off** that can be set for the FDTD region. This feature monitors the energy remaining in the simulation region as a fraction of the power shot into the simulation region. When this fraction of residual power in the system falls below a specified threshold value (It is the auto shut-off level), this prompts the simulation to end.

2.2.2 Geometric and material parameters

After defining a simulation region, we can insert our desired structure in the simulation zone using the structure tab available in the top main layout window. After that, we can set the dimensions for each structure and choose the structure's material. Materials are selected based on their refractive index. There are two ways to select a material; the first is selecting the material from the library provided by the software and the second one is user defined by inserting the material's refractive index.

2.2.3 Sources

These are several sources that can be used in the FDTD solver to be injected into the simulation region. These sources include point dipole source, Gaussian source, plane waves, total field scattered field (TFSF) source, mode source, and customized import source that each can be utilized based on application. We usually use the plan wave for our simulations in this work. We can set different parameters in the source setting menu, such as wavelength range, polarization, angle of incidence, and the amplitude of illumination.

2.2.4 Monitors

Monitors are needed to record data of simulation. There are different versions of monitors such as Index monitor, Frequency-domain field profile monitor, Frequency-domain power monitor, Movie monitor, and Mode expansion monitor. Each of these monitor record a bunch of data. It is essential to select just the required data to be recorded in the monitor's setting to decrease the simulation's time and file size. These monitors can be 2D in different planes, or 3D with specific dimensions can be set in the geometry tab of the monitor's setting. It is crucial to put the monitor in the proper position to achieve accurate data.

2.2.5 Mesh setting

Maxwell's equations are solved in FDTD solver by using a Cartesian mesh, and all the fundamental simulation quantities such as electromagnetic field, material, and geometrical properties are calculated at each mesh spot. There is one mesh intrinsic setting embedded in the FDTD region design's menu. In this setting's bar, there are three types of meshes; auto non-uniform, custom non-uniform, and uniform. Auto non-uniform is the default one in which there is a Mesh accuracy parameter with a slid bar ranging from 1-8. This parameter controls the precision of the FDTD solver in each mesh point. As the mesh accuracy becomes greater, simulations become more accurate, and the time of simulations increases. For sub-cell scale accuracy, the Mesh refinement parameter is used. The selection of mesh

refinement is dependent on the materials we are using in the system. Other settings include the DT-stability factor, which defines the time step for each mesh spot used for the simulation and minimum mesh step, giving the absolute minimum value for each interval for the whole region to be solved. Mesh override is another option that can be applied to the structures. This option exerts another mesh for higher accuracy in the particular zone inside the FDTD solver region. We can stabilize the time and the accuracy of the simulation by appropriate usage of both mesh options.

2.2.6 Boundary Conditions

Deliberating to select the boundary conditions correctly is one of the most important parameters to simulate our desired structure. There are six types of boundary conditions featured in this FDTD solver. If we have a 3D FDTD region, we should set the boundary conditions for each boundary plane of this region. It means we should set the boundary conditions for these six planes; **x min**, **x max**, **z min**, **z max**, **y min** and **y max**. Appropriate selection of boundary conditions (BC) is required to get the expected results. Below, these different types of BC's are discussed in detail.

Perfectly matched layer (PML):

The perfectly matched layer is a reflectionless boundary condition that can absorb the incident electromagnetic illumination. If we set this BC for any plane, the electromagnetic waves will be absorbed in the selected surface. Actually, PML came from a basic concept of electromagnetism that no reflection of waves takes place from the matched region in contrast to the unmatched part which reflects the waves. For this boundary condition, usually default parameters are used except tuning the number of layers (typically 278 to 12) to prevent the incoming light from reflecting back from the simulation domain. As the number of layers is increasing, the time of simulation and the accuracy increase.

Periodic boundary condition (PBC):

The periodic boundary condition is used when both the structure and electromagnetic fields are periodic. This boundary condition can be set for each direction, and for example, when you put the PBC for the x min plane, the system automatically selects the periodic boundary condition for the x max plane too. It means that periodic BC connects two ends of the simulation domain and is applied to both negative and positive sides of any axis. We usually set periodic boundary conditions for the plasmonics structures in the x and y direction and put PML in the z-axis.

Symmetric/Anti-Symmetric boundary condition:

This boundary condition is used when symmetry planes existed in the simulation, with both source and structure symmetric. Symmetric boundaries behave like a mirror for the electric field and an anti-mirror for the magnetic field. However, the reverse is true in the case of anti-symmetric boundaries i.e., mirror for the magnetic field and anti-mirror for the electric field. We can use this boundary condition in some particular cases instead of periodic to reduce simulation time with the same accuracy.

Metal or perfect electric conductor (PEC):

This boundary is applied to the surfaces which behave as a perfect electric conductor. In this case, the electric field components parallel to the metal boundaries, and the magnetic field components perpendicular to the metal boundaries are zero. Therefore this BC makes it a perfectly reflecting boundary conditions and does not allow any power to escape the simulation region along that specific boundary.

Perfect magnetic conductor (PMC):

PMC is the magnetic equivalent of the metal PEC boundary condition. Here, the electric field components perpendicular to the PMC boundaries and the magnetic field components parallel to the PMC boundaries are zero. Hence, it yields the

condition for perfect reflection. But, it is worth mentioning that although the PMC boundary condition is not experimentally realizable, PEC is applicable.

Bloch boundary condition (BBC):

This boundary condition is an extension of the periodic boundary condition. We can use the BBC when both the structure and electromagnetic fields are periodic; however, there is a phase shift that existed between each period. This condition is usually imposed when the periodic system is excited diagonally.

2.3 Simulating a metalens based on PB phase

Metasurfaces constituted of meta-atoms should design precisely to focus a collimated beam of incident light at the designed focal point; therefore, they can act as metalens. It is crucial to design the position and arrangement of meta-atoms correctly so the whole structure can provide the required phase like a conventional spherical lens. There are two major methods to achieve the target-phase profile: (i) Pancharatnam-Berry (PB) phase [55, 39] and (ii) Propagation phase [40, 56, 57]. The latter method involves the distribution of individual meta-atoms with different geometry/sizes to manipulate the phase. Meanwhile, the former way realizes the phase distribution by controlling the orientation angle θ of the meta-atoms with identical structural parameters. In this thesis, we use the PB phase method to design our metalenses. In both cases, to have the same function with spherical lenses, focusing a wavefront to a focal point, the phase profile of each meta-atom should satisfy the fundamental equation for the lenses (Eq.2.6) [58, 4]:

$$\varphi(x, y) = \pm k_0(f - \sqrt{x^2 + y^2 + f^2}) \tag{2.6}$$

Where $k_0 = 2\pi/\lambda$ and it is free space wave-vector of illumination with the wavelength of λ, f is the designed focal length, and x,y are the relevant coordinates of each meta-atom. Now, we should implement the PB phase according to this equation to our structures.

For the metalenses working based on PB phase method, we are utilizing of meta-atoms which have a twofold rational symmetry [59]. Therefore, the effective refrac-

tive indices along short and long axis will be different. On the other word, we use the elements that are structurally birefringent (Length > Width). Hence, the rectangular nanoblocks are the best option for this purpose. As a result of this birefringence properties, these nanoblocks can act as phase retarders and rotation of these nanoblocks based on PB phase theory can provide the required phase profile at each position. Therefore, it is a wave-plate and the retardation Jones matrix for this rotated nanoblock is given by:

$$T = R(-\theta)J_0R(\theta) \tag{2.7}$$

$$R(\theta) = \begin{pmatrix} cos(\theta) & sin(\theta) \\ sin(-\theta) & cos(\theta) \end{pmatrix} \tag{2.8}$$

$$J_0 = \begin{pmatrix} e^{i\phi_x} & 0 \\ 0 & e^{i\phi_y} \end{pmatrix} \tag{2.9}$$

Where, R(θ) is the rotation matrix and the J_0 is the phase retardation's Jones matrix of nanoblock before rotation. Here ϕ_x and ϕ_y shows the propagation phase difference of electric field along x and y axes [60, 61, 62]. Now if we consider the short axis is along with x direction we can conventionally write:

$$J_0 = \begin{pmatrix} 1 & 0 \\ 0 & e^{i\phi} \end{pmatrix} \tag{2.10}$$

where ϕ is the relative phase retardation along y-axis [20]. In this case, if the nanoblock can act as a half-wave plate, it results to ϕ=π and therefore, it makes the polarization conversion efficiency maximum [20, 4]. More importantly, acting as a half-wave plate provide a full phase coverage for the nanoblocks while rotation.

With all this taken to account, we investigate the Eq.2.7 again. If the nanoblock considered as a half-wave plate, we can write:

$$T = \begin{pmatrix} cos2\theta & sin2\theta \\ -sin2\theta & cos2\theta \end{pmatrix} \tag{2.11}$$

In this case, for the collimated circularly polarized light, $j_{\pm}=\begin{pmatrix}1\\ \pm i\end{pmatrix}$ and Jones vector for the exiting light can be written as:

$$j_{\pm}^{'} = TJ_{\pm} = \begin{pmatrix}1\\ \mp i\end{pmatrix} e^{\pm i2\theta} \tag{2.12}$$

where the + and - sign are stand for right and left circular polarized light, respectively [20, 63]. Here, the required PB phase for each nanoblock based on Eq.2.6 is ϕ=2θ. It means that based on Eq.2.6, if we choose a unit nanoblock which can act as a half-wave plate in the desired wavelength, we can easily achieve the required phase for the metalens by rotating each nanoblock while the value of rotation for each nanoblock in each position is θ=ϕ/2 (Eq.2.6). More importantly, comparing the $j_{\pm}$ and $j_{\pm}^{'}$ elucidates that the handedness of incident and transmitted light of metalens are opposite each other in this case [20, 59].

2.3.1 Polarization conversion efficiency

As mentioned above, to achieve the best focusing functions, each nanoblock should act as a half-wave plate, which birefringence characteristics of a single meta-atom can induce. This property allows the incident beam to reverse its polarization state after passing through the nanoblock. The ratio of the transmitted light with opposite helicity to the incident light is termed polarization conversion efficiency (PCE).

To calculate the PCE, we can use the swap method to find the highly efficient metalenses. First, we construct a unit cell of the nanoblock with the random structural parameters of the building block, i.e., length L, width W, height H of the nanoblock, and period P of the substrate. We choose the random number in the initial step in the range of previous works' choices for the working wavelength zone. After that, periodic boundary conditions are utilized along with the x and y directions, and a perfectly matched layer (PML) boundary condition is utilized in the z-direction. All simulations are set apart by a grid mesh with a step size of 0.25 nm to obtain highly accurate and necessary data of the structures. Then, we illuminate the right/left circularly polarized light (RCP/LCP) to the structure and calculate

the transmission of light with opposite handedness on the other side of the structure to find the ratio of PCE. We repeat this calculation multiple times by swapping one of the parameters each time while all other parameters are constant. Hence we can achieve a pattern like what we get in Figure4.3 (a,b,c). We did not swap the periodicity in these patterns, and we only change the nanoblocks' parameter each time. The vertical axis of each figure shows the range of parameter's dimension, and the horizontal axis shows the wavelength range. The heat map shows the PCE percentage at each point. We can choose the best dimensions for our nanoblock for the working wavelength zone by considering all the figures. The best-optimized dimensions for the structure in Fig.4.3 (a,b,c) is shown by the dashed lines in each figure based on our purposes in the operating wavelength range. Choosing these values for the dimensions of nanoblocks results to the high PCE and half-wave plate properties.

2.3.2 Full phase coverage

Based on the PB phase method, rotation of each nanoblock with θ degree will result in 2θ phase shift in the transmitted light. As we consider the nanoblock as a half-wave plate, we can have a complete phase coverage from 0 to 2π by rotating the nanoblocks. Hence, based on the Eq.2.6 we can easily achieve the required phase in each position of nanoblocks. To verify the principle of the PB phase, after finding the best structure with high PCE, we do another simulation to investigate if it has a full phase coverage. Therefore, we illuminate the unit cell of nanoblock, containing a nanorectangle on a substrate, with RCP/LCP light and calculate the phase of exiting light with the FDTD simulation method and set it as an origin. Then we rotate the nanoblock with a step of 10° until 180° and calculate the phase of transmitted light in each step. In the end, we plot the transmitted phase vs. angle of rotation for the structure. The ideal case based on the PB method is $\phi=2\theta$ as it is illustrated with a solid black line in figure 4.3 (e). As our data have a lower deviation from the ideal case, our structure is a better fit for a metalens design based on PB phase, and phase realization is better fulfilled in each coordinate.

2.3.3 Designing the lens (Scripting algorithm)

After finding the best nanoblock at the working wavelength, we can design the whole lens by taking advantage of Eq.2.6. First, we should decide about the radius (R) of metalens. Then, for the x and y values lower than R, we put the nanoblocks on the surface while the central coordinates of each nanoblock are the multiplication of periodicity number (P) in integers. Hence, if we assume the periodicity in the x and y direction is identical, we can estimate the number of nanoblocks at each design by dividing the area of metalens (πR^2) by the area of each unit cell (P^2). After that, we decide about the required phase of each nanoblock at each position with Eq.2.6 and then, based on PB phase theory, we apply θ=2ϕ to each nanoblock as a rotation angle. All of these processes are doing with a script in the FDTD solver software. It should be mentioned that designing the metalenses based on this method is polarization sensitive. In Eq.2.6, if we select the positive value, the metalens will work for RCP illumination and focus the RCP illumination in a focal point while it is LCP. On the contrary, if we choose the negative value in Eq.2.6, the metalens work under LCP illumination. Figure2.2 shows the full process of designing simple metalens. The unit cell, dimensions, and the required rotation are presented in Fig.2.2 (b-e), respectively. The process of focusing is shown in Fig.2.2 (a), and the whole designed metalens is demonstrated in Fig.2.2 (f) [4].

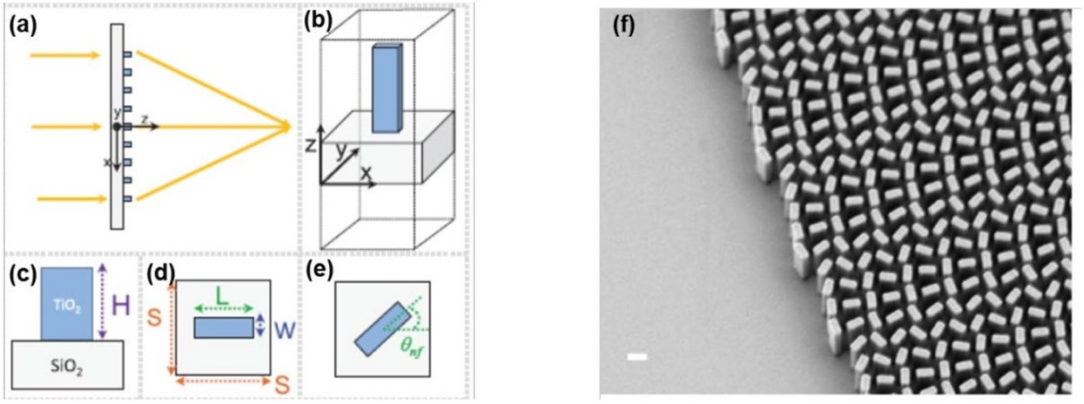

Figure 2.2: **(a–e)** Schematic and **(f)** scanning electron micrograph of nanoblocks used to form a metalens. L,W, and H are representative of length, width, and height of nanoblock, respectively, and S is the periodicity of the unit cell [4].

2.3.4 Hybrid Cells

To overcome the polarization dependency problem, we can use hybrid metalenses. The process which is presented in the previous sections is for designing a simple lens working for circularly polarized light. However, we can design metalenses working at both LCP and RCP simultaneously by using the hybrid method [64, 65]. In this design strategy, after finding the proper unit cell properties, nanoblocks are concurrently rotated by θ_R=+ϕ(x,y)/2 (for RCP) and θ_R=-ϕ(x,y)/2 (for LCP) via alternative distribution of the unit cells in both x and y directions. Therefore, using this method, the designed metalens can effectively work to focus both LCP and RCP light in a focal lens with a converted polarization.

2.4 Important parameters

2.4.1 Diffraction limit and Numerical aperture

Different parameters can determine the resolution of the optical system. Among all of these factors, although the factors such as lens imperfection or misalignments can affect the resolution, the physics of diffraction is one of the most crucial parameters that directly specifies the optical system's resolution. Diffraction is the group of phenomena, happens when a wave sees an obstacle or an opening along the way of its propagation. It has been found that the minimum resolvable distance (d) that light with the wavelength of λ can travel in a medium with a refractive index of n, while converging to a spot with a half-angle θ, can be calculated based on Eq.2.13 [60, 66]:

$$d = \frac{\lambda}{2nsin(\theta)} \tag{2.13}$$

This theoretical distance is called the diffraction limit of light, and When an optical system has a resolution at the instrument's limit, it is called diffraction-limited. To verify whether a device is diffraction-limited or not, we can calculate the full width half maximum (FWHM) of the lens. If we plot the intensity profile of light at the focal plane (x-y plane at z=focal length (f)) along with x-direction while y=0, the width of Gaussian shape distribution at half maximum intensity is

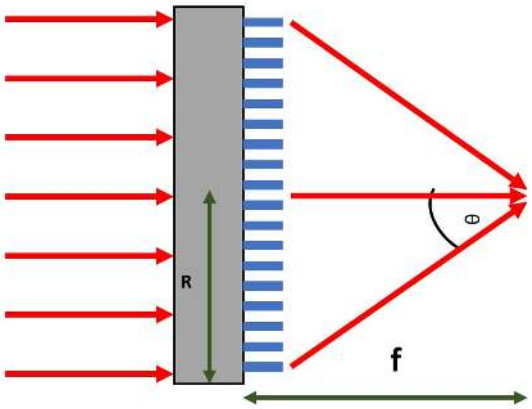

Figure 2.3: The schematic of metalens while light passes the lens and focuses into the focal spot.

called FWHM. If the value of FWHM is equal to or higher than the value of d, it is called diffraction-limited.

In this equation (Eq.2.13), the value of $nsin(\theta)$ in the denominator is called the numerical aperture. This parameter is a dimensionless factor determining the range of angle values of light accepted or emitted by the optical system. Most of the time, since the light propagates through the air after passing the lens, n can be considered 1. Figure2.3 shows the position of θ. Also, the radius (R) and focal length (f) of the lens are determined in this figure.

2.4.2 Focusing efficiency

The focusing efficiency (FE) is an important parameter that can determine the effectiveness of metalens. FE can be defined as the power within the focal region at the focal plane to the total power incident upon the lens. In some studies, they measure the FE by calculating the fraction of power passing through the radius of three times of FWHM at the focal region in the focal plane to the total incident power [57, 67]. However, to avoid the unwanted diffraction and make higher precision, we calculate the FE as a ratio of power passes within the focal region with a radius of two FWHM in the focal plane to the incident [64, 68, 69].

2.4.3 Depth of focus

The depth of focus (DOF) is the distance between two planes on the optical propagation axis in which the image has an acceptable sharpness. In other words, when we focus an illumination into a focal point, there is a distance field around the focal spot that still suitable focusing characteristics can be observed. The formula to calculate the DOF is given by [70]:

$$\Delta f = 4\lambda \frac{f^2}{D^2} \tag{2.14}$$

Where Δf is DOF, λ is the operating wavelength, f is the practical focal length, and D is the diameter of the lens.

Chapter 3

OPTIMIZATION OF FOCAL SHIFT EFFECT AND FOCUSING EFFICIENCY FOR METALENSES

Enhancing the resolution and image quality at the focal zone for the metalenses has been the most crucial and valuable feature, should be considered in their applicability [39, 71, 72, 19]. Early classical investigations express that the principal maximum intensity of the diffracted wave is located at the geometric focus, and the field exhibits definite symmetry about the geometrical focal plane. However, after practical observation, it has been shown that this principle maximum intensity of the incident wave may not occur at the geometrical focus under certain circumstances and may experience a bit deviation from the theoretical expected position. This phenomenon is referred to as the 'focal shift' and attributed to the Fresnel number of the focusing system [73, 74, 75]. One significant disadvantageous result of the focal shift phenomenon is the appearance of asymmetric intensity distribution in the focal region [76, 73, 74, 77, 75, 78, 79, 80]. Thus, reducing the focal shift for better-performing metalens is critical as it leads to a symmetric airy disc-like field distribution on the focal spot. Recent studies on planar metalenses mostly describe the focal shift phenomena by only considering the Fresnel number as an effective parameter, and some further claim that the relative focal shift from the geometric focus is totally dependent on the Fresnel number [73, 77, 74, 78, 79, 80]. An interesting observation is that for planar metalenses, the focal shift usually occurs toward the lens, defined as the negative focal shift [81, 82, 73]. The actual focal lengths of the reported high contrast grating lens, planar plasmonic slit lenses, and traditional dielectric lenses are smaller than the designed ones [74]. However, a positive focal shift is observed mostly in spherical or truncated lensing systems.

3.1 Overview

This section presents a systematic theoretical analysis to minimize the focal shift phenomenon on planar dielectric metalenses. We offer metalens designs constituted of Si and Ge nanoblocks that operate in the mid-IR frequency range and theoretically study their lensing performance using the finite-difference time-domain method. The metalenses work at 3 and 4μm wavelengths with a polarization conversion efficiency (PCE) near unity. We show that in addition to the Fresnel number, the focal shift appearance on dielectric metalenses is strongly related to the numerical aperture (NA), and increasing the Fresnel number is not always the approach to minimize the focal shift. Unlike previous studies, we define a critical NA where the focal length aberration for the metalens reaches a minimum, and a symmetric focal intensity distribution is obtained, leading to better-performing metalens. The focusing efficiency of the metalens is calculated as high as 70%, one of the best values reported for the mid- IR range so far. More importantly, in contrast with the existing studies, we show that for NA higher than the determined critical value, a positive focal shift happens on planar metalenses instead of conventional negative focal deviation. We show that as the designed focal length decreases from higher values, while the lens size has kept constant, the negative focal shift weakens and becomes zero at a particular NA. After this point, if the focal point decreases, reaching higher numerical apertures, the focal shift becomes positive. Also, the effect of diameter, material, and focusing efficiency is investigated in this section.

3.2 Mid-IR metalenses designs

To achieve highly efficient metalenses in the mid-IR frequency range both silicon (Si) and germanium (Ge) nanoblocks are precisely arranged on calcium fluoride (CaF_2) substrate (Fig.3.1). It is expected that a sharp refractive index contrast between the background and nanoblocks exists for effective handling of the phase, which results in efficient metalenses [64]. Thus, Si and Ge are chosen due to their high refractive indices (n_{Ge}=4.04 and n_{Si}=3.43) at the designed operating wavelengths of 3 and 4 μm and their wide usage in a cleanroom. A commercial electromagnetic

solver software based on the finite-difference time-domain method (Lumerical Inc., Vancouver, Canada) is employed to perform all simulations. The optical constants of Si and Ge are taken from Palik et al., which are available in the software library. The refractive index of CaF_2 is set to $n = 1.41$. A unit cell, as shown in Fig.3.1 (b), is formed for simulations. The incident light source is set as a right/left circularly polarized (RCP/LCP) plane wave and sent as illustrated in Fig.3.1 (a). Also, the top view of the full lens is presented in Fig.3.1 (d).

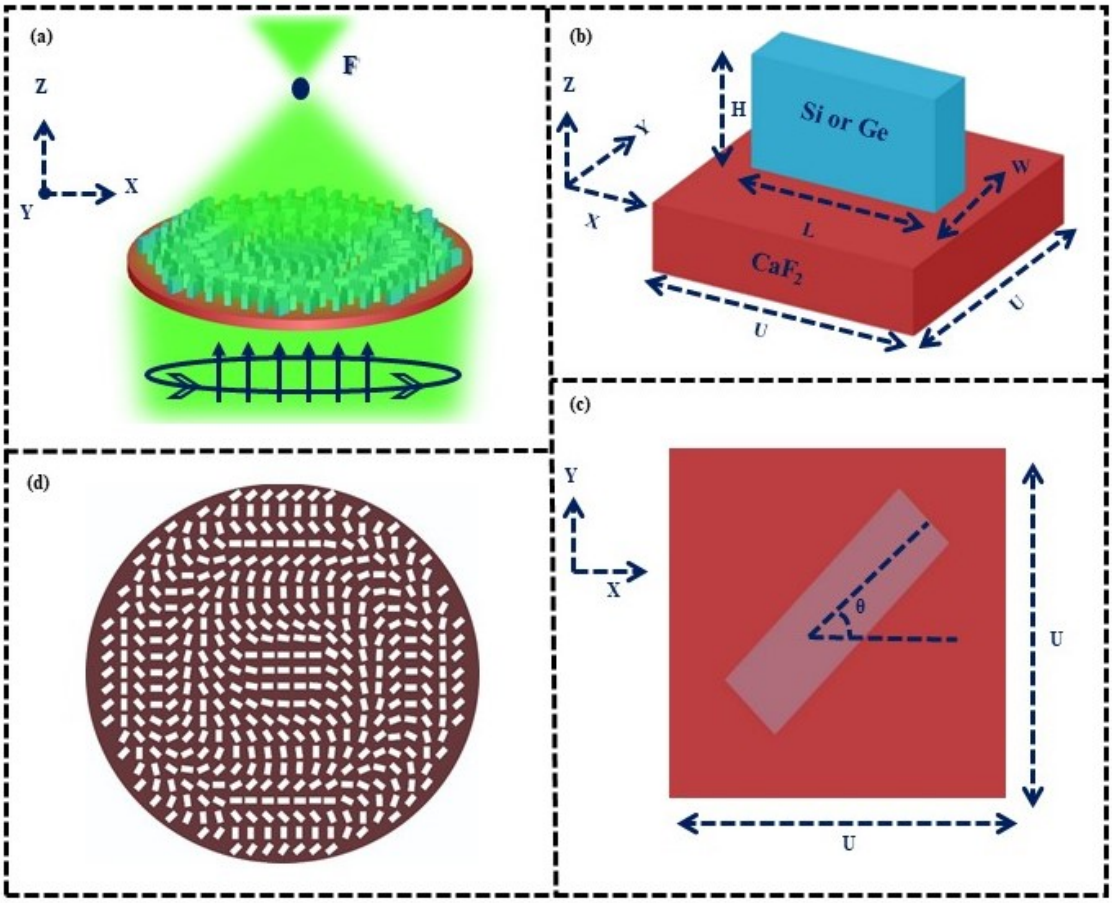

Figure 3.1: (a) A schematic of the designed metalenses based on geometric PB phase elements to focus the incident light at focal point F. (b) A single nanoblock of Ge/Si on the CaF_2 substrate, with corresponding length L, width W, and height H. The unit cell repeat itself in both x, and y direction with periodicity U to compose the metasurface. (c) Each nanoblock within the metasurface will experience a rotation of an angle θ according to PB phase.(d) The top view of nanoblocks arrangement.

To focus a circular polarized incident beam, the metalens is constructed in such

a way that it fulfils the Pancharatnam-Berry (PB) phase condition: the individual nanoblocks are rotated with an angle θ to achieve full 2π phase coverage. The θ in Figure 3.1 (c) is determined by equation 3.1 in which (x, y) are the coordinates for each nanoblock [20, 83, 84]:

$$\theta(x, y) = \frac{\pi}{\lambda_d}(f_d - \sqrt{f_d^2 + x^2 + y^2}) \tag{3.1}$$

Where λ_d and f_d are designed wavelength and focal length. Therefore, the phase profile required for each nanoblock to focus the incident circular polarized light at the focal spot is ϕ_{PB}=2θ. As a result, the right-circularly polarized (RCP) incident light will experience a 2π phase shift and convert to the left-circularly polarized (LCP) light [4, 37, 85]. Hence, the maximum polarization conversion efficiency (PCE), which is defined as the power ratio of transmitted circular light with opposite helicity to the incident light, is achieved when each nanoblock functions as a half wave-plate [86]. The half wave-plate feature arises from the asymmetric cross-section of the nanoblock [87]. Hence, by properly optimizing the geometrical parameters (length L, width W, height H) and period U of the unit cell (Fig.3.1 (b)), nanoblock will act as a half waveplate. Asymmetricity is brought into the system by playing with the width for a fixed length, height, and periodicity values to introduce the half waveplate feature in each nanoblock. Therefore we apply this asymmetry by changing width W against the constant L, H, and U at the operating wavelength. As a result, the effective refractive indices along the long axis (n_e) and short-axis (n_o) change, resulting in a phase retardation Γ to achieve half waveplate characteristics of the nanoblock at a certain width. The phase retardation [88] generated by a single nanoblock is given as:

$$\Gamma = \frac{2\pi H(n_e - n_o)}{\lambda_d} \tag{3.2}$$

where H is the height (also known as propagation length) [89, 60], λ_d is the designed operating wavelength, n_e and n_o are the effective refractive indices along the long axis and short axis, respectively.

To confirm the half waveplate characteristic of each nanoblock MODE simulator within Lumerical software is utilized to calculate the effective refractive indices along

both the long axis and short axis of nanoblocks. A single Si and Ge nanoblock suspended in the air is considered for MODE simulations. Similar to the FDTD simulations, periodic boundary conditions are applied in both x and y directions, and a perfectly matched layer (PML) boundary condition is imposed for the z axis for MODE simulations. Figure3.2 b(i) shows the simulated n_e, n_o, and Γ (using Eq. 3.2) as a function of width W of the Si nanoblock at the designed wavelength of 3μm. Other geometrical parameters are kept constant as $L = 0.89\mu$m, $H = 1.5\mu$m, and $U = 1.3\mu$m. Figure3.2 b shows that control over the width of nanoblock enables precise tuning of n_e and n_o, resulting in a phase retardation along both axes. Modification of the width from $W = L$ to a certain value of W leads to phase retardation from 0 to π. As a result, for the specified L, H, and U, the nanoblock acts as a half waveplate at the optimized value of $W = 0.43\mu$m. Similar analysis are made for the Si nanoblock operating at 4μm (Fig.3.2 b(ii)), Ge nanoblock operating at 3μm (Fig.3.2 b(iii)), and Ge nanoblock operating at 4μm (Fig.3.2 b(iv)). The optimized geometrical parameters for each type of nanoblocks are obtained as shown in the Table 3.1. The aspect ratio of the optimized nanoblock ($H/W < 4$) is acceptable, and the structures could be routinely fabricated in a cleanroom environment.

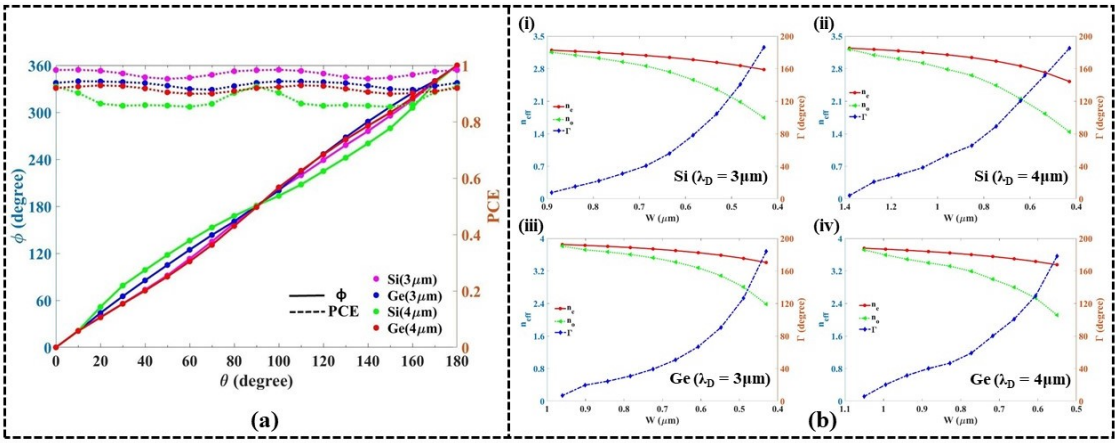

Figure 3.2: (a) Phase (ϕ) and Polarization conversion efficiency (PCE) of the optimized unit cell for each case as a function of rotation angle θ.(b) Phase retardation Γ, and the effective refractive indices along the long-axis (n_e), and short axis (n_o), as a function of width W of the Si, Ge metalens's building blocks designed at 3μm (i, iii) and 4μm (ii, iv), respectively.

λ_d (μm)	Material	W(μm)	L(μm)	H(μm)	U(μm)
3	Ge	0.43	0.96	1.5	1.3
	Si	0.43	0.89	1.5	1.3
4	Ge	0. 55	1.05	1.6	1.5
	Si	0.43	1.38	1.9	1.5

Table 3.1: Optimized geometrical parameters length (L), width (W), height (H), and period (U) of the unit cell composed of rectangular nanoblocks for the Si, Ge metalenses designed at $3\mu m$ and $4\mu m$.

We further simulate the single unit cell with optimized geometric parameters shown in Table 1 using FDTD and calculate the PCE and phase of the optimized metalenses as a function of rotation angle θ. Figure 3.2 (a) shows that the rotation angle does not significantly affect the PCE, and the average calculated PCE for each case is above 80%, ensuring the highly focusing characteristics of the designed metalens. Also, it is shown in Figure 3.2 (a) that each θ applied to each nanoblock can produce a phase $\phi = 2\theta$, satisfying the PB phase condition, both for the Si, Ge nanoblocks operating at 3μm and 4μm wavelengths. Thus, rotating the nanoblocks by an angle θ = 0-180^0 one can achieve the full 360^0 phase coverage required to focus the incident circular polarized light beam at a designed focal point, and therefore we can utilize these unit cells to prepare our metalenses.

After confirming the high PCE of each unit cell, we construct the circular metalens array constituted of unit cells using FDTD. We utilize a script code to precisely place the nanoblocks at each position (x, y) within the designed diameter D of the metalens with rotation angle θ (Eq. 3.1) satisfying the PB phase condition. Here, PML(Perfectly meshed layer) boundary condition is employed in all three x, y, and z directions, and a right/left circularly polarized light beam is incident from the substrate side. After transmitting through the metalens surface, the incident light is expected to focus at the designed focal spot F as shown in Figure 3.1 (a) at a focal length f_d, which is used in Equation 3.1. In practice, due to the focal shift effect, the simulated focal point is located on the z-axis but with a deviation from

its designed value. The distance of this actual focal point to the lens is defined as f_s. Overall, the focal shift in this work is calculated using the absolute value of a ratio, in which the aberration from the designed focal length is divided by the designed focal length value. ($\% \ \Delta f = \mid \frac{f_d - f_s}{f_d} \mid \times 100$).

3.3 Fresnel number and focal shift theory

Fresnel number, N, is defined as a parameter that helps determine the diffraction of light that passes through an aperture and hits the screen. For an aperture of radius a and the focal length of f (the distance from screen), the Fresnel number is given by Eq.3.3: [90, 91, 92]

$$N = (\frac{a^2}{\lambda f}) \tag{3.3}$$

Where λ is the operating wavelength. Here, a (aperture radius) for the lens is its radius (R). When the focal shift occurs, a high phase difference exists between the central part of the lens and its edges[75]. The smaller Fresnel number means a higher diffraction effect and, as a result, a great phase difference between the middle parts and margins of the lens. Some mathematical expressions have proposed to approximate the focal shift based on Fresnel number [73]. However, among all of them, the formula derived by Y. J. Li [80] is the most common one in which only the Fresnel number is its variable. Based on the definition we presented for the focal shift in our work, we can write Li's approximation (Eq.3.4) accordingly:

$$\frac{\Delta f}{f} = \left(1 + N \times \sqrt[c]{1 + (\frac{\pi^2 N}{12})^c}\right)^{-1}, (c = 1.51) \tag{3.4}$$

Here, N is the Fresnel number, and c is a constant that its proper selection will increase the accuracy of this formula [80]. The desired value for c is usually considered 1.51 as Li calculated. Figure 3.3 shows the relative focal shift Vs. Fresnel number based on 3.4.

Now, if we consider the half-angle of cone of light at focal spot equal to θ, as we define before, the NA= $sin\theta$ and $tan\theta = \frac{R}{f}$. Therefore, by taking advantage of these two relations, we can rewrite the NA as a function of Fresnel number and vice versa

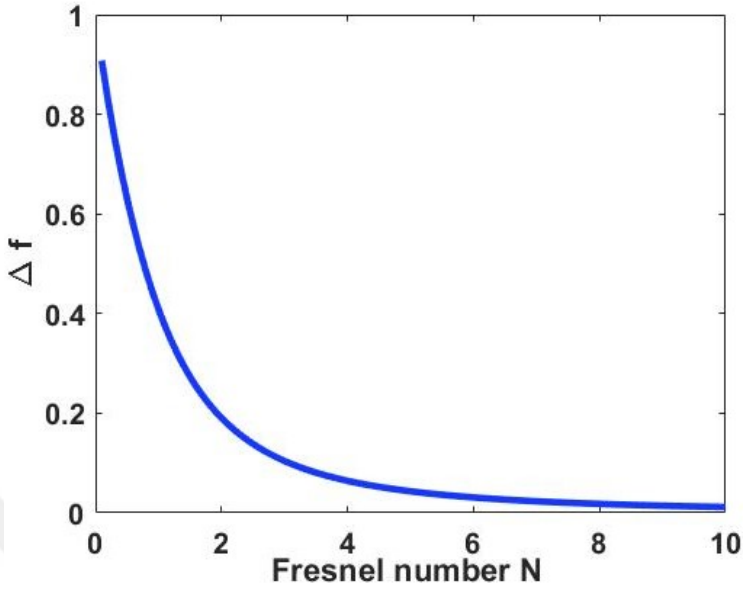

Figure 3.3: Relative focal shift Vs. Fresnel number according to Eq.3.4

(Eq.3.5).

$$N = (\frac{a^2}{\lambda f}) = (\frac{R \times R}{\lambda f}) = (\frac{R}{\lambda}) \times tan\theta \longrightarrow \theta = tan^{-1}(\frac{\lambda N}{R}) \longrightarrow tan(sin^{-1}(NA)) \times \frac{R}{\lambda} = N \tag{3.5}$$

Therefore, based on Eq.3.5, we can conclude that for a metalens working in a specific λ and with a constant R, increasing of NA will result in higher Fresnel number values. Comparing this conclusion with Eq.3.3, one can expect that increment of NA, as it raises the N value, may eventuate to lower focal shift numbers. However, based on our results, a positive focal shift occurs in higher numerical aperture ranges in metalenses. In the latter sections, we show that although the fresnel number is an effective parameter for predicting the focal deviation, NA also plays an essential role in this aberration.

3.4 Result and discussion

To analyze the performance of the proposed metalenses, we illuminate the metalenses designated at $\lambda_d = 3$ μm, $\lambda_d = 4$ μm (for both Ge, Si case) by an incident monochromatic light source (RCP polarized) of a similar wavelength ($\lambda_{incident} = \lambda_d$). The

dimensions of constituent nanoblocks for each metalens are presented in Table.3.1. Metalenses are irradiated with the light source from the substrate side as shown in Figure.3.1 (a) to focus at a focal point f along with propagation direction (z-axis). The metalenses are designed in three diameters (D= 30, 60, and 100μm) for both Si-based and Ge-based lenses. Fig.3.4 and Fig.3.5 show the focusing characteristics of the metalenses composed of Si and Ge rectangular nanoblocsks at two different designed wavelengths (3μm and 4μm) in the Mid-IR region of the electromagnetic spectrum respectively. As illustrated in Fig.3.4 and Fig.3.5, for each diameter of metalens, three focal lengths are presented for both materials. The focal lengths are set for each structure in a way that all of them experience working in three specific NA (0.3, 0.65, and 0.95). The data information for their focal lengths and their Fresnel number value are presented in Table.3.2. In these figures, the diameter of each lens is specified on the left vertical axis in μm (30, 60, and 100 μm from top to bottom respectively), the NAs are determined on the top horizontal axis (from left to right, 0.3, 065 and 0.95 respectively) and the materials are defined on the bottom horizontal axis (from left to right, Si and Ge respectively). The normalized electric field intensity distribution profiles in the x-z plane at y=0 are shown in Fig.3.4 (a-f; *i*, *ii* and *iii* labeled sub-figures) and Fig.3.5 (a-f; *i*, *ii* and *iii* labeled sub-figures). Also, Fig.3.4 (a-f; *iv*, *v* and *vi* labeled sub-figures) and Fig.3.5 (a-f; *iv*, *v* and *vi* labeled sub-figures) depict the focusing profiles in the x-y plane at focal point z=f for each metalens. As it can be observed, in both figures (Fig.3.4 and Fig.3.5) and in each case (a-f), the focal pattern for NA=0.65 is more symmetric and tightly confined around the focal point in comparison with others in the same section. In both Fig.3.4and 3.5, the Normalized intensity profiles of each focal spot presented at *iv*, *v*, and *vi* labeled sub-figures, along with y=0, are presented in *vii*, *viii*, and *ix* labeled sub-figures correspondingly. The full-width half-maximum (FWHM) for each case is calculated in these *vii*, *viii*, and *ix* sub-figures. Taking both materials into consideration, the values of FWHM are changing from 1.6μm to 5μm for the metalenses working in 3μm (Fig.3.4 and they vary from 2.15μm to 6.34μm for the metalenses working at 4μm (Fig.3.5). As we did in the first chapter, it worth mentioning that increasing NA will decrease the FWHM.

Design information			
D(μm)	NA	f_d (μm)	Fresnel number(N)
30	0.3	47.69	1.57 (at $\lambda = 3\mu m$) and 1.17 (at $\lambda = 4\mu m$)
	0.65	17.53	4.27 (at $\lambda = 3\mu m$) and 3.2 (at $\lambda = 4\mu m$)
	0.95	4.93	15.21 (at $\lambda = 3\mu m$) and 11.4 (at $\lambda = 4\mu m$)
60	0.3	95.38	3.14 (at $\lambda = 3\mu m$) and 2.35 (at $\lambda = 4\mu m$)
	0.65	35.06	8.55 (at $\lambda = 3\mu m$) and 6.41 (at $\lambda = 4\mu m$)
	0.95	9.86	30.42 (at $\lambda = 3\mu m$) and 22.81 (at $\lambda = 4\mu m$)
100	0.3	158.98	5.24 (at $\lambda = 3\mu m$) and 3.39 (at $\lambda = 4\mu m$)
	0.65	58.45	14.25 (at $\lambda = 3\mu m$) and 10.7 (at $\lambda = 4\mu m$)
	0.95	16.43	50.72 (at $\lambda = 3\mu m$) and 38.04 (at $\lambda = 4\mu m$)

Table 3.2: The information about diameter (D), numerical aperture (NA), designed focal length(f_d) and Fresnel number (N) for the designed metalenses presented in Fig.3.4 and Fig.3.5.

If we want to investigate the focal shift phenomena in these metalenses based on the previous theory, one can expect that there would not be any focal shift when the Fresnel number is more than 8 [73, 77]. However, based on our analysis, another focal shift occurs at higher Fresnel number values. Hence, for a metalens with a constant diameter, at high NA values, a positive focal shift happens contrary to negative ones in the lower Fresnel number region (For a fixed diameter, lower N values occur at lower NA zone). Therefore, NA is another parameter that affects focal shift phenomena. On the other hand, as the diameter increases, the Fresnel number moves toward much larger values and makes an effect on the focal shift pattern.

In the following subsections, we elucidate the effect of these parameters on focal shift. In addition, we investigate the behavior of focusing efficiency and materials selection's role on optimizing the design's factors accordingly. We will also introduce the concept of Critical NA (NA_c) as a crucial operative that should be considered in the metalens design.

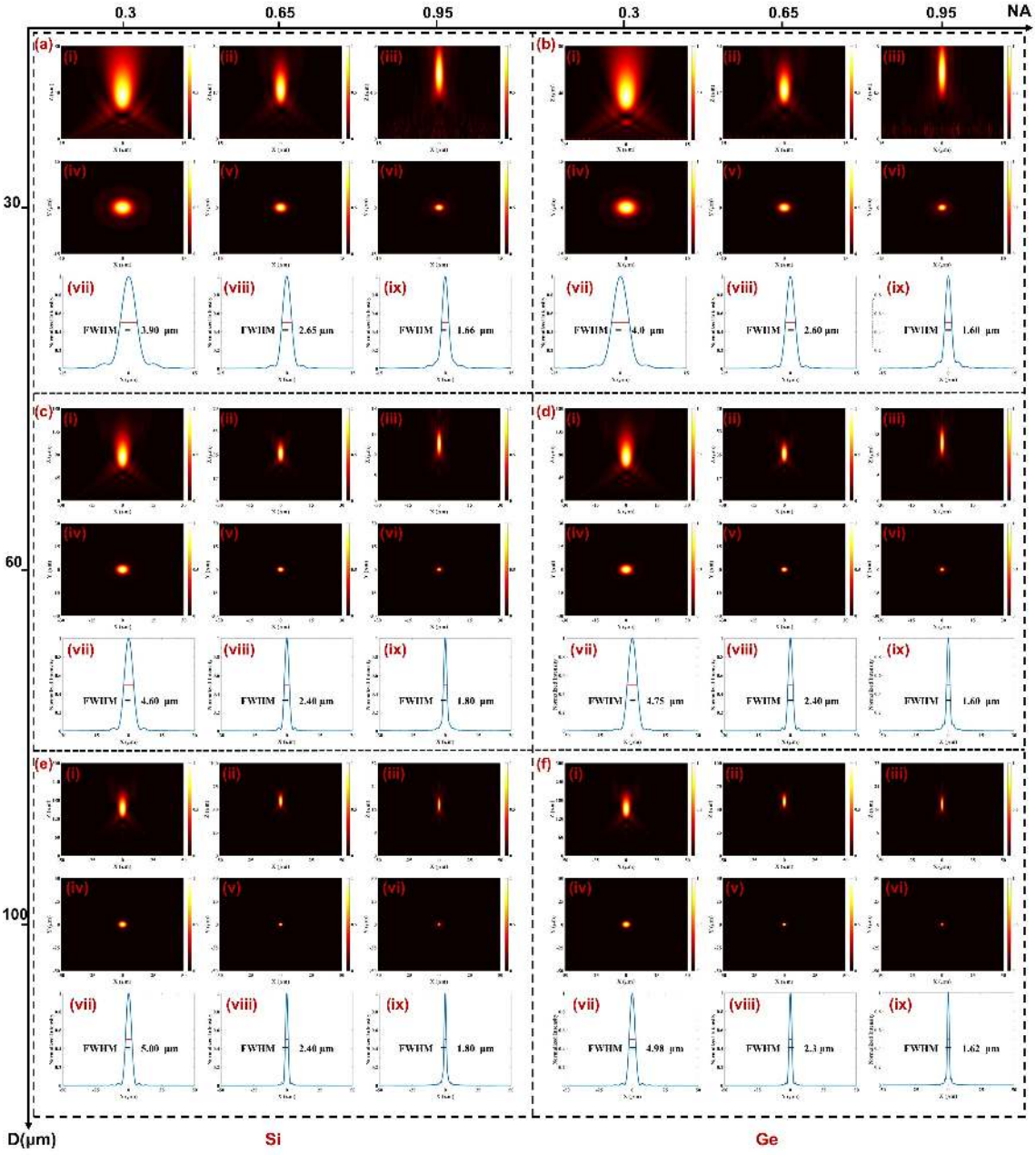

Figure 3.4: Simulated normalized electric field intensity profiles of the metalens designated at $\lambda_d = 3$ μm, for both Si and Ge cases, when illuminated with an RCP polarized light source of incident wavelength $\lambda_{incident} = \lambda_d$. The diameters in μm are mentioned in the left vertical axis, the NAs are mentioned in the top horizontal axis, and the materials are mention in the bottom horizontal axis. $(a-f)i$, ii, **and** iii show the focusing profiles in the x-z plane at y=0. $(a-f)iv$, v, **and** vi illustrate the focusing profiles in the x-y plane at z=F. $(a-d)vii$, $viii$, **and** ix exhibit the corresponding intensity distribution along with the horizontal cut at y=0 in $(a-f)iv$, v, **and** vi, giving the FWHM values of the diffraction-limited focal spots.

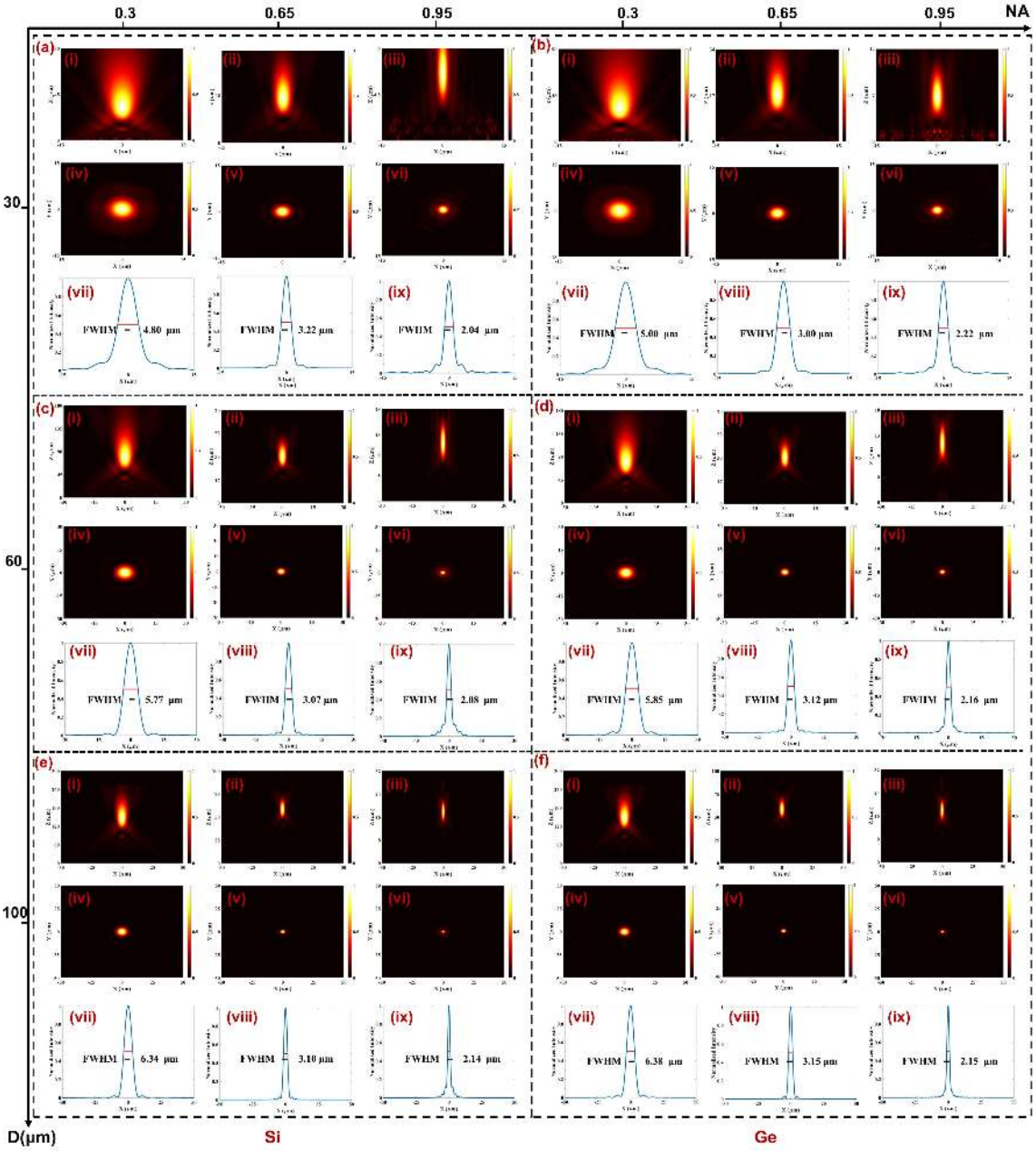

Figure 3.5: Simulated normalized electric field intensity profiles of the metalens designated at $\lambda_d = 4$ μm, for both Si and Ge cases, when illuminated with an RCP polarized light source of incident wavelength $\lambda_{incident} = \lambda_d$. The diameters in μm are mentioned in the left vertical axis, the NAs are mentioned in the top horizontal axis, and the materials are mention in the bottom horizontal axis. $(a-f)i$, ii, **and** iii show the focusing profiles in the x-z plane at y=0. $(a-f)iv$, v, **and** vi illustrate the focusing profiles in the x-y plane at z=F. $(a-d)vii$, $viii$, **and** ix exhibit the corresponding intensity distribution along with the horizontal cut at y=0 in $(a-f)iv$, v, **and** vi, giving the FWHM values of the diffraction-limited focal spots.

3.4.1 Effect of numerical aperture

In this subsection, we investigate the effect of designed numerical aperture on the focusing characteristics of the proposed metalenses. Initially, we designed a number of Si and Ge metalenses with different numerical apertures within a range of 0.3-0.95, designed at 3μm and 4μm. All the metalenses have the same diameter D=30μm, and are illuminated with an RCP polarized monochromatic incident light source of the corresponding frequency. Figure.3.6 shows a comparison of designed and simulated focal lengths as a function of designed numerical aperture. As it can be observed, on the extreme values of NA (at lower and higher values of designed NA, NA_d), the simulated focal length (f_s) is significantly deviating (≈35%) from the designed focal length (f_d). However, within the zone where NA_d has the values between 0.65-0.75, this deviation reduces to just <3%. We define this region as the critical region (NA_C), where this deviation takes a minimum value. More importantly, the type of focal shift differs between the NA points before and after this critical zone. Before NA_C the negative focal shift ($f_d > f_s$) and after NA_C the positive focal shift($f_d < f_s$) is observed. This positive focal shift was not reported clearly in previous studies [73, 74, 77]. Although in the Table.4 of reference [73], similar phenomena can be reflected, it was not elaborated at all.

To further confirm this behavior of the metalenses under study, we design the metalenses with different numerical aperture values between 0.3-0.95, in three diameters (30,60 and 100μm) working at 3 and 4 μm. It is evident from Figure.3.7 (a,b) that all the rest types of metalenses show the same trend. In this figure (Fig.3.7 (a,b)), the total focal shift ($\% \Delta f = \mid \frac{f_d - f_s}{f_d} \mid \times 100$) is plotted versus the designed NA for the metalenses working at 3 and 4 μm. As it can be observed, there is a certain region of NA_d in both of these sub-figures that can result in a minor difference between f_d and f_s. Hence, it confirms that the designed numerical aperture can play a vital role in focusing the incident light beam at the focal point along the propagation direction. To make more confirmation of our proposal about the presence of critical NA (NA_C), we did the same analysis for a metalens working in the visible region. For this purpose, we took advantage of the metalens' unit cell designed by H.Dong

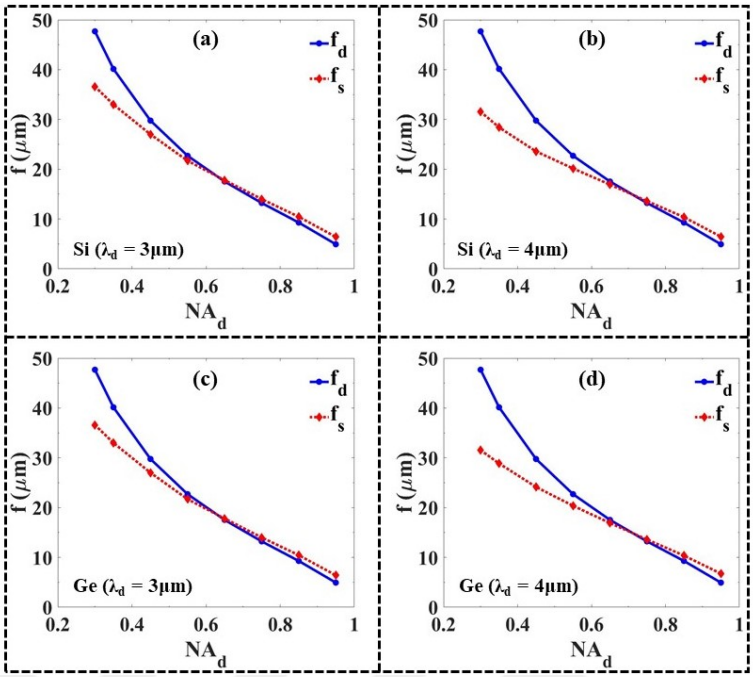

Figure 3.6: A comparison of designed (f_d) and simulated (f_s) focal lengths as a function of designed numerical aperture NA_d for the Si, Ge metalenses working at 3μm (**a, c**), 4μm (**b, d**) respectively. In each case, there is a critical NA region, resulting in a minimum deviation of f_s from f_d. All the metalenses have D=30μm, and illuminated with RCP monochromatic light source of incident wavelength $\lambda_{incident}$ = λ_d.

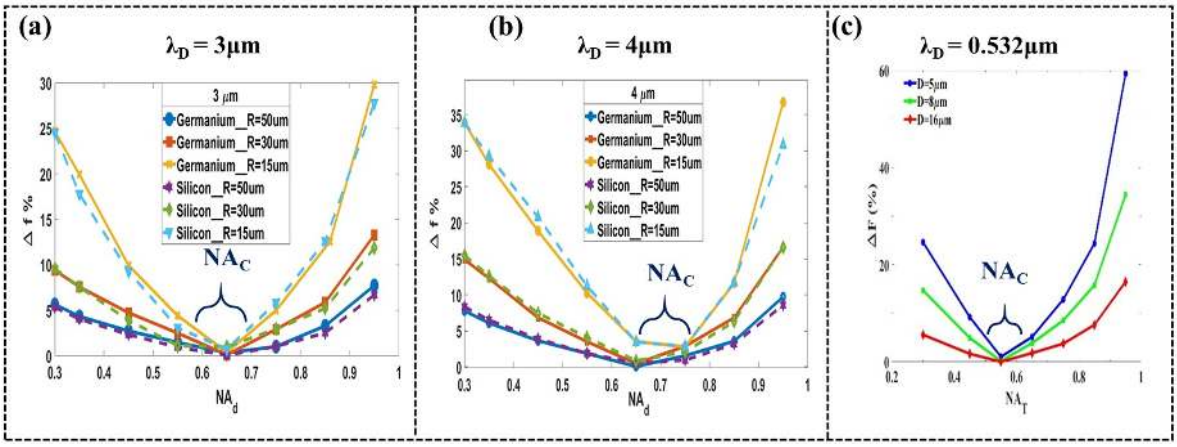

Figure 3.7: Percentage deviation(Δf %) of simulated focal length from the designed focal length as a function of NA_d for the Si, Ge metalenses having the diameters D=30, 60, and 100μm operating at 3μm **(a)**, 4μm **(b)**. **(c)** Δf (%) as a function of NA_d for the ZnS metalenses having the diameters D=5, 8, and 16μm operating at 532 nm in the visible region. In each case, percentage deviation in the focal lengths can be intentionally reduced especially at the extreme NA points by an increment in the diameter.

[93] for working at = $0.532\mu m$. Unit cells constitute of ZnS nanofins on glass in which $L = 70nm$, $H = 550nm$,$W = 290nm$ and $P = 320nm$. Again we constructed metalenses with these characteristics in 3 diameters (5, 8, and 16 μm). Then, with the same procedure, we designed them in different NA values between 0.3 to 0.95 to see the focal shift's behavior with respect to NA, in the metalenses working in the visible region (Because of simulation's power limitation, we could not go beyond 16nm for diameter in the visible region). As it can be observed in Figure.3.7 (c), the trend of focal shift percentage is the same as the previous observation at 3 and 4 μm. Interestingly, the presence of NA_C is understood here again. However, the value of NA_C for this metalenses is around 0.5 to 0.55. Therefore, based on the comparison between the sub-figure presented in Fig.3.7, we can correlate the value of NA_C to the working wavelength.

These observations are different from previous theories in which they expected to make the focal shift zero at higher Fresnel numbers. As shown in Fig.3.3, it is predicted that the value of focal shift reaches zero for the N values higher than 8. However, by taking the Table.3.2 into consideration, we can see that even at very high values of Fresnel number, we have some positive focal shift. Hence, we can conclude that the Fresnel number is not the only parameter to predict the focal deviation. Actually, before the (NA_C) value, as we are in the smaller Fresnel number region, the diffraction effect is the more dominant, and the Eq.3.4 has more accuracy [73, 75]. As the NA starts increasing, the Fresnel number reaches larger values. The increment of the Fresnel number in this region results in a decrease in the focal shift based on the Eq3.3. The decrements of focal deviation continue to near zero as we reach the NA_C point. Therefore, the positive focal shift, which is shown in our results, is not considered in Eq.3.4. Hence, the second parameter starts playing the role to make this focal shift behavior. We believe that this parameter is NA. Actually, the focusing characteristics of metalenses are dependent on the discontinuous phase profile. Although decreasing the period for each unit cell may minimize this phase discontinuity effect, this phase discontinuity nature becomes more stranger at higher numerical aperture values. As the result of this feature in metalenses, a slight focal shift may arise at high numerical aperture values, which is different in nature from

what happens before NA_C [94, 95, 82, 81]. Hence, although it was mentioned that at higher Fresnel number values, the geometric optics is adequate to predict the focal length, the positive focal shift happens in higher numerical aperture region after NA_C due to this phase discontinuity feature. So, choosing the NA_d within a critical regime which has the lowest value of focal deviation in this study can significantly overlap the designed and simulated focal lengths in this class of metalenses. More importantly, taking the focusing characteristics of the lenses working in the NA_C zone into consideration (Fig.3.4and Fig.3.5), we can easily understand that the focal point is very symmetric and confined in compression with others with the same diameter.

3.4.2 Effect of diameter

The diameter of the designed metalens is another parameter to investigate that can significantly impact the focusing performance. The effect of diameter(D) is first of all on the Fresnel number. The Fresnel number has a square relation with the radius (R) of metalens(R=D/2); secondly, as we increase the diameter, since the number of nanoblocks increase for one metalens, the phase discontinuity effect decrease in higher NAs. It can be seen in Figure3.7 that increasing the diameter will decrease the focal shift in all the NA values. Therefore as figure3.7 shows, the Δf is firmly dependent on the diameter outside a critical NA region (NA_C).It is worth noting that inside NA_C region Δf is almost independent of the diameter for all the cases.

3.4.3 Focusing efficiency behavior and material's effect

Focusing efficiency is another crucial parameter to define the metalens performance. It is defined as a ratio of optical power in the focal region (a circular region with a diameter of $\sim$ 2×FWHM) to the total incident power. To realize the dependence of FE on the designed numerical aperture and the diameter of the corresponding metalens, we calculated the FE values for each designed metalens as mentioned in previous sections. Figure 3.8 (a) shows as we increase the NA_d from 0.3 up to a specific value around $\sim$0.65-0.75 (which is NA_C region for our structures), FE is

almost unaffected by this change for the Si, Ge metalenses operating at 3μm. (The FE is higher at lower NA since they have much larger FWHM)

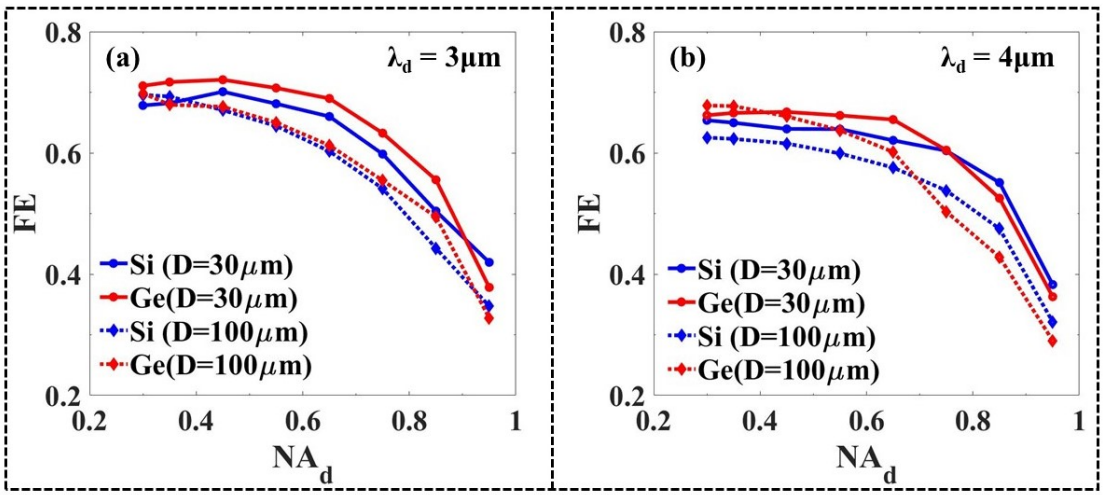

Figure 3.8: Focusing efficiency (FE) as a function of designed numerical aperture for the Si, Ge metalenses with diameter D=30, 100μm operating at 3μm **(a)**, and 4μm **(b)**. In both the cases (a, b), an increase in the numerical aperture up to 0.65 does not significantly change the FE.

Meanwhile, a further increase in numerical aperture causes a drastic drop in the FE values. On the other hand, increasing diameter slightly decreases the FE but follows the same trend as a function of numerical aperture. Figure.3.8 (b) depicts the FE values for the Si, Ge metalenses with two different diameters designed at 4μm as a function of numerical aperture. It can be seen that all the metalenses are operating at 4μm show similar response to NA$_d$ and diameter change, as in the case for 3μm metalenses.

From the materials perspective, as shown in Fig.3.8, the *Ge* metalenses show a better focusing efficiency behavior in comparison with Si ones in most NA values.

3.5 Conclusion

To conclude our discussion we can mention that to have the best performance of our metalenses we should consider these points:

(i) select a designed numerical aperture within a critical NA region, such that

simulated focal length has the minimum deviations from the designed focal length without any size dependence. More importantly, the FE values in this range of NA are almost equal to the maximum value of NA at lower NA numbers.

(ii) choose a size of the metalens in the mid-range to minimize the %Δf, independent of NA_d selection within a critical region NA_C. Although decreasing the %Δf, increasing the diameter will decline the FE value.

(iii) Focal shift is almost independent of material. However, material selection is essential to achieve the highest possible number for FE.

Hence to summarize our discussion, we can say that unless we require high NA metalenses for some specific applications, we can always choose a NA up to a critical region with mid-range diameters to achieve highly efficient metalenses with the minimum focal shift.

Chapter 4

MULTIFOCAL METALENSES AT ULTRAVIOLET REGION

4.1 Motivation

The applications of optical devices working in the ultraviolet region, ranging from lithography and imaging to quantum information and spectroscopy, have created a high demand for efficient-powerful devices in this range [96, 97, 21].Metalenses can offer highly efficient and manipulatable lensing properties within small structures. Therefore designing metalenses with tunable focusing characteristics is a necessity within the UV region. However, UV-based devices are less reported as compared to their counterparts due to substantial absorption loss for many dielectric materials inside the UV regime (200-400 nm) [98, 99]. Also, metalenses with the metals nanoblocks cannot be used in this frequency range for the same reason.

Choosing the materials for the metalenses has always been challenging, and it thoroughly depends on the materials with high refractive indices. Most studies express that an efficient metalens usually needs a sharp refractive index gradient between background and nonofins [64]. However, there is still no solid rule of thumb to understand the refractive index characteristics needed for efficient metalenses. Based on the previous studies, low refractive index materials, as they are more transparent with large bandgaps, are better candidates to utilize for the metalenses with higher efficiency [64, 100]. However, in the UV region, the transparent materials have a limited range of dielectric constant [64]. On the other hand, in most of the previous works within the UV region, the materials of the nanofins and the substrate were different; MgO and Si_3N_4 on the glass [64, 101] or AlN on the Sapphire [102].

Besides the materials perspective, the functionality of metalenses is another crucial parameter. There are many types of metalenses have been designed includ-

ing polarization-insensitive [103, 104],chromatic and achromatic [105, 106], hybrid [64, 107], single [101] and multi-focal [108, 73] metalenses. Multifocal metalenses are designed to boost the functionality of metalenses, and they focus single incident light beam at different desired focal points for many applications such as optical communication, imagining and holography, laser lithography, and spectroscopy [109, 110, 111, 112, 113]. Most of the previous works in the UV region were single focal. However, based on the wide applications of multifocal metalenses in this range, introducing a multifocal metalenses with design-tunability properties is essential.

4.2 Overview

In this work, we introduce the first ultraviolet multifocal metalens entirely composed of aluminum oxide (Al_2O_3). In these metalenses, the material of both nanoblocks and substrate is (Al_2O_3). Although based on previous studies, almost high refractive index difference between substrate and nonoblocks was a standard consideration to design metalenses, here all the system is composed of a single material, making the fabrication process easier. Geometrical parameters such as length (L), width(W), height (H), and period (P) of nanoblock of metalens are obtained via the fine-tuning mechanism. The unit cell of metalens could convert a beam of a circularly polarized incident beam into inverse circularly polarized light with more than 73% polarization conversion efficiency (PCE) through UV regime (200-400nm). The maximum PCE value is obtained as 93% at 263 nm. Based on the PCE profile, the design parameters can be utilized for constructing metalens for other wavelengths inside the UV region (200nm-400nm) without any significant functionality difference. Compared with the other reported studies, our uni-focal metalens provides narrower FWHM values such as 143, 181, 207, and 241 nm at the designated four different wavelengths 210, 263, 305, and 358 nm, respectively.

More importantly, in this work, we introduce the multifocal UV metalenses that can easily be tuned and focus the target wavelength with a linearly polarized incident beam into multifocal spots along with both longitudinal and transverse directions P-B phase modulation method. These metalenses can be designed to focus a linear

polarized incident into one or two pairs of right circular polarized (RCP) and left circular polarized (LCP) focal points. Here, by taking advantage of new phase engineering method in addition to regional designing technique, we can extend the number of focal spots.

4.3 Design principle

In order to study a multi-focal metalens based on non-contrast metasurface, we choose Al_2O_3 because of its high transmission, ultra-wide bandgap (7 - 7.6 eV), and refractive index ranging 1.9–1.79 in the designed frequency region. Figure4.1.a shows the unit cell of our designed metalens consisted of Al_2O_3 nanoblock on the Al_2O_3 substrate. Here again, to achieve the best focusing functions, each meta-atom should act as a half-wave plate which can be induced by birefringence characteristics of a single meta-atom. The optimized structural parameters of the designed metalens's unit-cell are P=180nm, L=160nm, W=80nm, and H=875nm. Figure4.1.b also shows the method that we used to achieve full phase coverage. Based on the Pancharatnam-Berry (PB) phase method, by rotating the nanoblock placed on the substrate, we can acquire a full phase coverage for our design. Therefore, by implementing this PB phase method to compose the metalens, a smooth shift in the local phase from 0 to 2π via a linear phase-angle relationship $\varphi = 2\theta$ happens, which satisfy the fundamental phase equation (Eq.4.1 [58]:

$$\varphi(x, y) = \pm k_0(f - \sqrt{x^2 + y^2 + f^2}) \tag{4.1}$$

As introduced before, $k_0 = 2\pi/\lambda$ is free space wave-vector, f is the designed focal length, and x,y are the relevant coordinates of each meta-atom, and $\pm$ sign represents the helicity of the input light beam, Right-handed circular polarization (RCP or $|R\rangle$) and Left-handed circular polarization (LCP or $|L\rangle$) respectively. As discussed before, metalenses based on the PB phase method are mostly polarization-dependent and work for circularly polarized light either an $|R\rangle$ or $|L\rangle$ state of the incident light beam. However, by a precise modification and manipulation in the phase-equation (Eq.4.1) we can construct a metasurface to focus a linearly polarized ($|LP\rangle$) light beam into multiple focal points with different polarization states. Here,

We discuss two types of metalenses: (i) Uni-focal operating for circularly polarized light, (ii) Multi-focal operating for linearly polarized incident light beam.

Figure4.2 presents schematic views of all the focusing systems have studied in this work. As shown in Fig.4.2 (a) a uni-focal metalens is depicted, which focus a right circular polarized ($|R\rangle$) light beam into a focal spot with opposite helicity ($|L\rangle$) at the designed focal length **f**, along with the longitudinal direction (z-axis). This metalens is a single-material lens which has constituted of rectangular Al_2O_3 nanoblocks with the structural parameters mentioned above, on Al_2O_3 substrate in which these nanoblocks are distributed on the surface based on the Eq.4.1. Therefore, each meta-atom is rotated by an angle θ (Fig.4.1) to compensate the surface phase distribution according to $\varphi = 2\theta$ relationship, given as:

$$\theta(x,y) = \frac{1}{2}\varphi(x,y) = \pm\frac{k_0}{2}(f - \sqrt{x^2+y^2+f^2}) \tag{4.2}$$

A schematic diagram for a dual-focal metalens is also shown in Figure4.2 (b). When metalens is excited with a linearly polarized ($|LP\rangle$) light beam, it focuses incident light into two symmetric focal points with opposite helicity ($|L\rangle$) and ($|R\rangle$) at the designed focal point **f** along the z-axis. As the linear polarized light is composed of left and right circular polarized source ($\mathrm{E}_{x-LP} = \frac{\sqrt{2}}{2}\left[\begin{pmatrix}1\\ i\end{pmatrix} + \begin{pmatrix}1\\ -i\end{pmatrix}\right]$), to focus the ($|LP\rangle$) into ($|L\rangle$) and ($|R\rangle$) at different positions, we can simply achieve the required phase by superposition of their corresponding phase-terms. Hence, the total phase can be modified as [45]

$$\varphi_{df}(x,y) = arg[e^{i\varphi_i} + e^{i\varphi_j}] \tag{4.3}$$

where $\varphi_i = k_0(f_i - \sqrt{(x-x_i)^2+(y-y_i)^2+(f-f_i)^2})$ and $\varphi_j = -k_0(f_j - \sqrt{(x-x_j)^2+(y-y_j)^2+(f-f_j)^2})$ are the phase terms to focus ($|R\rangle$) at (x_i,y_i,f_i), and ($|L\rangle$) at (x_j,y_j,f_j), respectively. Just like uni-focal metalens, dual-focal metalens is composed of identical nanoblocks, rotated by a modified angle satisfying the condition $\theta = \varphi_{df}/2$.

In the end, Figure4.2.c shows a quad focal metalens which focuses the $|LP\rangle$ light beam into two $|R\rangle$ and two$|L\rangle$ polarized focal spots. Here, we take advantage of

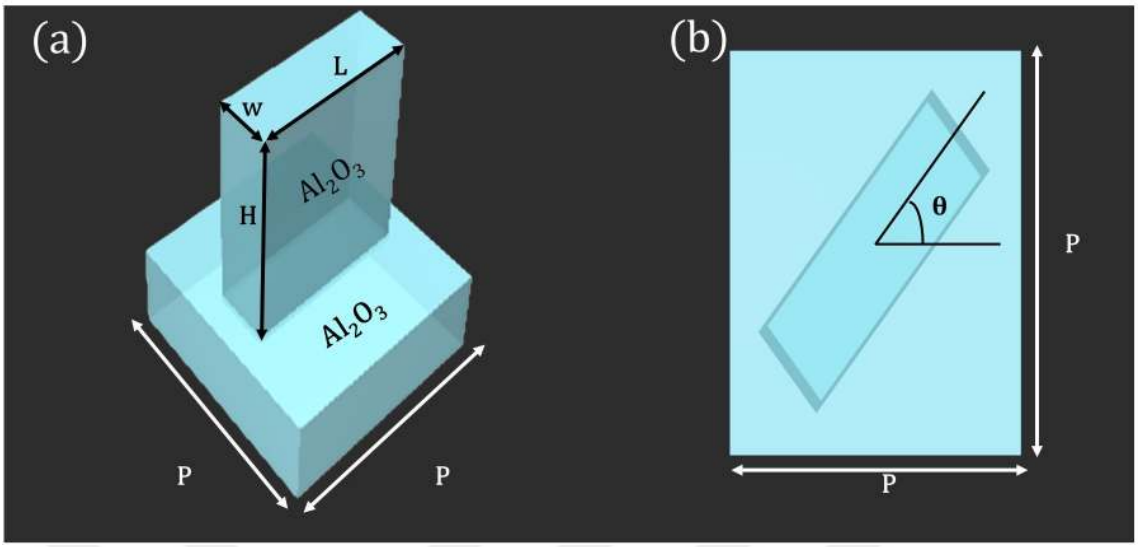

Figure 4.1: **(a)**The unit cell of dimensions P×P for uni-focal,dual-focal and quad-focal metalens, where an Al_2O_3 nanoblock with height of H, length L, and width W placed on Al_2O_3 substrate. **(b)** The individual nanoblock is rotated by an angle θ to introduce required phase according to geometric PB phase method.

Eq.4.3 phase engineering and regional designing technique, which will be elaborated in the quad focal section.

PCE analysis

Again, we start our simulations related to one building block of the metasurface in the first step. To numerically analyze the electromagnetic properties of the designed structures, we employed a commercial software program (FDTD Solutions, Lumerical Inc.). We used Palik [114] model for the optical constant of Al_2O_3, which is defined in the program library. For the calculations related to a single unit cell, the incident light source is set as RCP or LCP. All the boundary conditions and grid mesh size are based on what was proposed in the second chapter (The periodic boundary conditions are utilized along with the x and y directions, and a perfectly matched layer (PML) boundary condition is being used on the z-direction. Grid mesh with a step size of 0.25 nm). After that, we used the parameter sweeps are performed to reach the optimal unit cell yielding a maximum PCE. Each time we change one parameter in this method while other parameters are constant at their

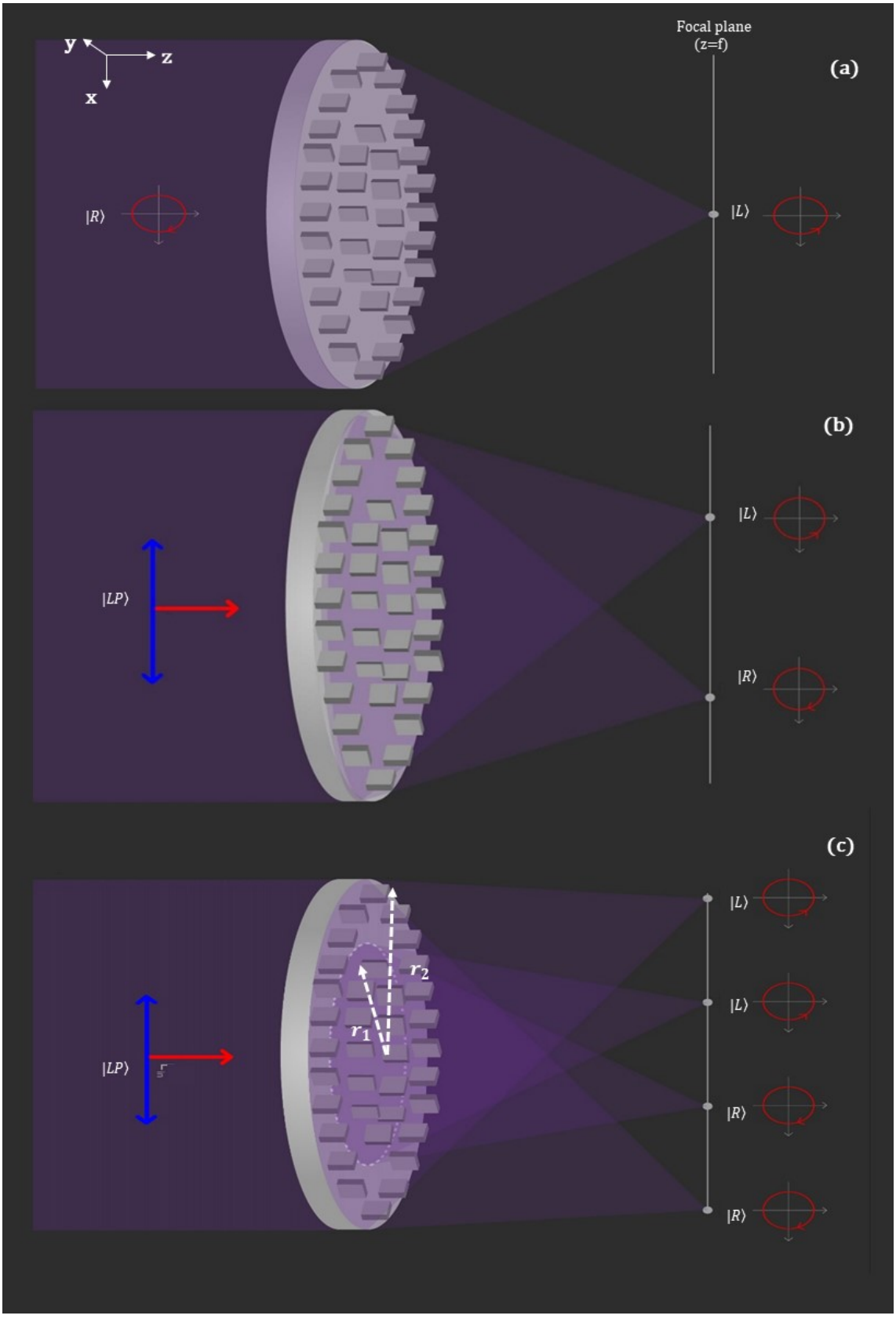

Figure 4.2: **(a,b and c)** A schematic view of the designed uni-focal, dual-focal and quad-focal metalens composed of uniformly spaced Al_2O_3 nanoblocks with different orientation on Al_2O_3 substrate operating in the UV region.

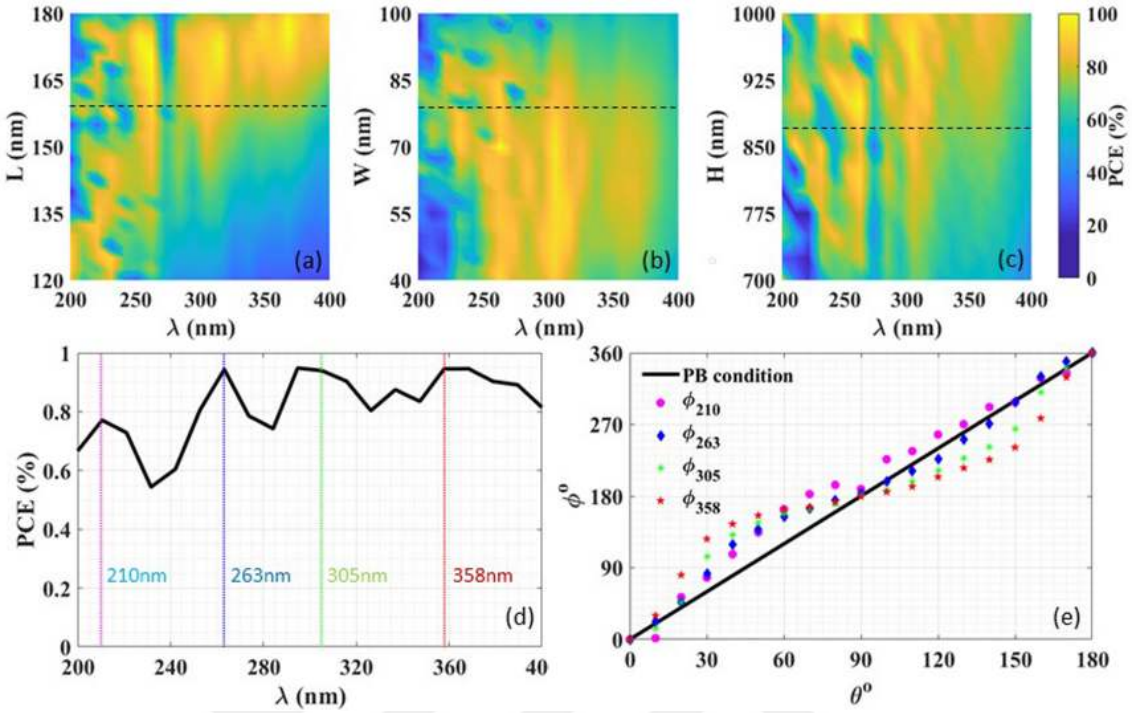

Figure 4.3: **PCE** as a function of incident light wavelength λ and length L **(a)**, width W **(b)**, height H **(c)** of the nanoblock. The optimized values for L, W, and H are specified by Horizontal dashed line in **a-c**. By using these parameters, the maximum PCE in the system will be acheived. **(d)** The simulated PCE of Al_2O_3 nanoblock with optimized structural parameters on Al_2O_3 substrate as a function of wavelength. Vertical dashed lines show the designated four different wavelengths (210, 263, 305, and 358 nm) that are chosen to determine the focusing characteristics of the proposed metalens for each of them. Here, the minimum PCE is 73%. **(e)** Required phase profile and calculated phase profiles of nanoblock as a function of rotation angle θ within range of 0^0-180^0, at the corresponding wavelengths. The optimized structural parameters of nanoblock are $L = 160$ nm, $W = 80$ nm, $W = 875$ nm, and unit cell with period $P = 180$ nm.

optimum values. Then for each step, we calculate the value of PCE at each λ in our desired wavelength range. As illustrated in Figure4.3, the PCE as a function of L (Fig.4.3 (a)), W (Fig.4.3 (b)), and H (Fig.4.3 (c)) of the nanoblock in the designed frequency regime (200-400nm) is measured. The horizontal dashed lines highlighting in each of these plots show the best average PCE in the whole region. Figure4.3 (d) presents the calculated PCE of an optimal nanoblock across the desired wavelengths inside the UV region. The PCE plot depicted in Fig.4.3 (d), offers the possibility to use this structure in multiple wavelengths. Therefore, to demonstrate the focusing

characteristics of our non-contrast metasurfaces, we choose four wavelengths 210, 263, 305, and 358 nm, shown by vertical dotted lines with a maximum PCE of 93% of Fig.4.3 (d). Finally, Fig.4.3 (d) exhibits phase shift of the unit cell as a function of rotation angle, calculated at all four chosen wavelengths. The solid black line shows the ideal phase profile, and the dashed lines are the phase profiles for the proposed metalens at each specified wavelength. It can be seen that the designed unit-cell composed of Al_2O_3 nanoblock completely covers the whole phase range from 0 to 2π, and more importantly, satisfying the linear phase-angle relationship $\varphi = 2\theta$ governed by the PB phase method. However, a small aberration from the linear phase-angle relationship can be realized because nanoblocks do not behave as a perfect half-wave plate.

4.4 Single focal

We construct four different metalenses at the designed wavelengths of 210, 263, 305, and 358 nm for the study of uni-focal metalens. All the metalenses have the same diameter of **D=10** μ**m**, and composed of Al_2O_3 nanoblocks with identical structural parameters rotated by an appropriate angle θ given by Eq.4.2. These metalenses are designed to focus the $|R\rangle$ light into the focal spot with opposite helicity. The right circular polarized light illuminated from the Al_2O_3 substrate and focus on a diffraction-limited focal spot with left circular polarization.

Figure4.4 shows the diffraction-limited focusing characteristics of the uni-focal metalenses at the designated wavelengths in the UV range. The normalized electric field intensity distributions in the x-z plane (at y=0) are shown in Fig.4.4 (a-d) at each wavelength. The designed focal length for each of these structures is $4\mu m$, and the simulated values are calculated as 4.76, 4.65, 4.56, and 4.53 μm for = 210, 263, 305 and 358 respectively. As discussed in the previous chapter, here, the designed NA is 0.7. Based on the observation we had in chapter 3, the critical value of NA is dependent on the working wavelength, and it was lower for the visible range than the mid-IR range (0.55 for visible and 0.65 for the mid-IR). Therefore, we can expect that the critical NA for the UV region is less than 0.55. Hence, as the designed

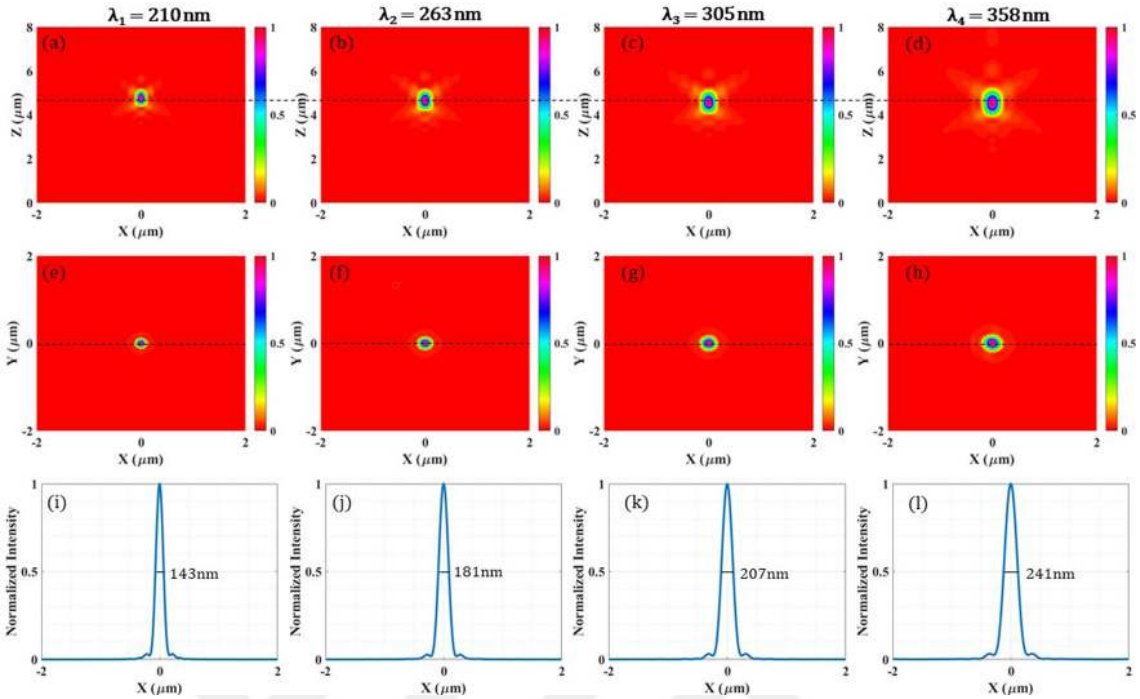

Figure 4.4: **(a–d)** Simulated normalized intensity profiles of focal spot at y=0 (in x–z plane) for uni-focal metalens at the designated 210, 263, 305, and 358 nm, respectively. **(e–h)** Simulated normalized focal spot intensity profiles at z=f (x–y plane) for the corresponding wavelength. **(i–l)** Normalized intensity distribution of focal spots along x-axis at y=0 (horizontal dashed lines in e-h) for the corresponding wavelength. The profiles present diffraction limited full width at half maximum (FWHM) of 143, 181, 207, and 241 nm, respectively. Each metalens has the diameter of 10 μm and is illuminated by monochromatic RCP incident light. The designed focal length is also $5\mu m$ for all the structures.

NA here is more than the critical NA in the UV regime, the existence of a positive focal shift is predictable. Figure4.4 (e-h) depicts the simulated normalized intensity profiles in the x-y plane (at z=f) for each metalens. The intensity distributions of the focal spots are clearly seen as bright, symmetric, and strongly confined at the center of the focal region of the metalenses. Here, the designed focal spot is set to be at x=0 and y=o. These focal spots are distributed symmetrically as Gaussian-shaped, with corresponding full width at half maximum (FWHM) of 143, 181, 207, and 241 nm shown in Fig.4.43 (i–l). Here, we obtain narrower FWHM values as compared with previously reported work on metalenses at UV range [98, 115, 104, 64]. The simulated focusing efficiencies of the four designed uni-focal metalenses are found as

40, 37, 30, and 25%, respectively, which is an acceptable value for single-material metalens. The focusing efficiency is calculated by taking the ratio of optical power in the focal region with an area (A=2×FWHM) to the total incident power. As it can be seen, the proposed metalens structure works excellent in all the designed wavelengths.

4.4.1 Angle dependence

In this subsection, we investigate the effect of incident angle on the focusing performance of our uni-focal structures. Here again, the diameter of the metalenses is 10 μm, and the designed focal length is 4 μm.

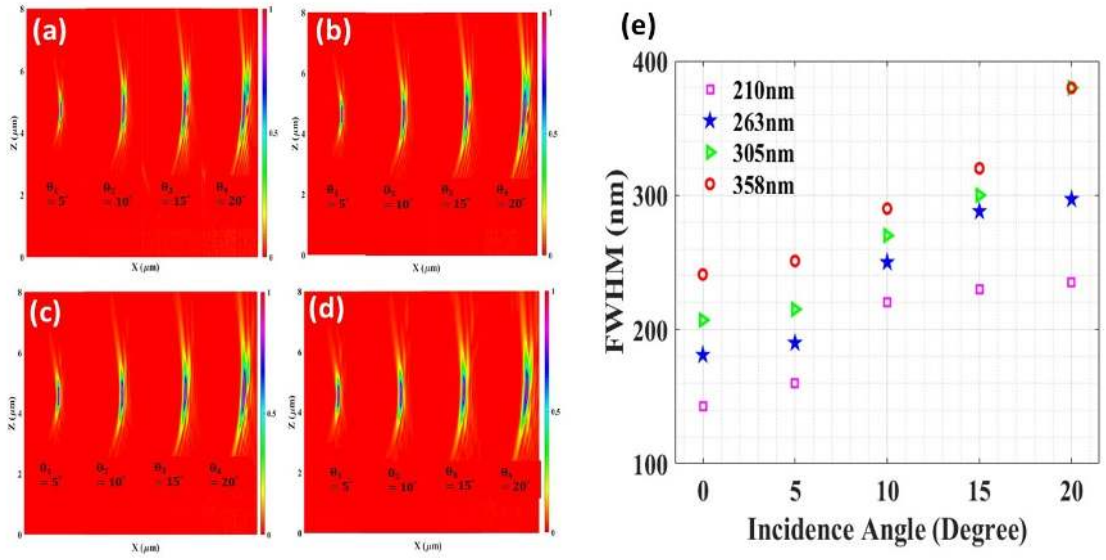

Figure 4.5: The simulated electric field intensity in x-z plane at y=0 for a designed metalens working at **a** 358nm,**b** 305nm, **c** 263 nm and **d** 210 nm. In each figure the four focusing profiles are depicted in four beam incident angle (5°,10°,15° and 20°). As beam incident angle is increasing, the focal points move toward more positive values in the x-direction. Changing of FWHM while increasing of angle also is shown for each metalens in **e**

.

Figure 4.5 (a-d) shows the normalized simulated electric field intensity distributions in the x-z plane (at y=0) for each metalens working at 358nm,305nm,263nm, and 210nm, respectively. In each of these subfigures, the changing of the focal spot is

shown based on the applied incident angle. As it can be seen, as the angle is increasing, the focal spot becomes more distorted and more elongated in the z-direction. It is related to the increment of FWHM as a result of the increasing of incident beam angle, which is shown in Fig.4.5 (e). In this figure, the FWHM for each metalens is specified for any applying incident angle. As it can be observed, FWHM goes toward the higher values as the incident angle increase in all the cases.

Angle Dependence information				
λ(nm)	Angle°	f_s (μm)	FWHM (nm)	x_s(μm)
358	5	4.51	251	0.46
	10	4.53	290	0.92
	15	4.69	320	1.34
	20	4.71	380	1.77
305	5	4.56	215	0.46
	10	4.61	270	0.91
	15	4.73	300	1.32
	20	4.87	380	1.73
263	5	4.64	190	0.46
	10	4.7	250	0.9
	15	4.81	288	1.31
	20	4.53	297	1.59
210	5	4.75	160	0.46
	10	4.87	220	0.77
	15	4.87	230	1.22
	20	4.69	235	1.6

Table 4.1: The information about the dependence of metalens behavior on the incident angle. Four angles are tested (5,10,15 and 20) and the simulated focal length, FWHM and deviation is x direction are presented in the table for each metalens. All the metalenses have the diameter of 10 μm and the designed focal length is 4 μm. The right circular polarized light is used to illuminate all of them.

More importantly, as the beam incident angle is going to the higher values, the fo-

cal spot has more positive deviation in the x-direction for all the cases. As mentioned in the uni-focal section, all the metalenses were designed based on Eq.4.2. According to this equation, metalenses will focus an incident circular polarized light into a spot with opposite helicity while the coordinates of the focal spot are x =0,y =0 and z =f, which f is the focal length. When the incident angle is zero, these conditions fulfilled correctly, as can be seen in the uni-focal section. However, as presented in Fig.4.5 and Table.4.1, with the same design configuration used for uni-focal metalenses, we can shift the focal spots in x-direction just by applying the angle. The x_s and f_s in the Table.4.1 are representative for the position of the focal point in the x-direction and the simulated focal point, respectively. The f_s again has a positive shift in compression with the designed value regarding the designed NA number and shows an additional positive deviation by increasing angle. This investigation shows that applying an angle is a method to move the focal spot in the x-direction for the metalenses designed based on Eq.4.2, although the focusing performance may be damaged with deformation of the focal site. More importantly, predicting the focal spot position in the x-direction is not that much correct, and it is time-consuming even with a distorted focal point. In further sections, we show another method to control the focal point position in the x and y direction in a more accurate way.

4.5 Dual focal

In this section, we design four metasurfaces by manipulating the focal points at different positions in both the transverse and longitudinal planes to realize dual-focal metalenses with robust focusing characteristics. The diameter of all the metalenses is **D=10 μm**, and the operating wavelength is 358 nm. The metalenses are illuminated with $|LP\rangle$ incident light beam. The designed metalenses are constituted of Al_2O_3 nanoblocks uniformly distributed on an Al_2O_3 substrate, with different in-plane orientations. These nanoblocks obey the phase equation presented in Eq.4.3to fulfill the required phase conditions for dual-focusing properties. Therefore each nanoblock will experience $\theta = \varphi_{df}/2$ (Eq.4.3) rotation to comply the phase requirements in each position. As the $|LP\rangle$ incident light beam could be considered as a superposition of

$|R\rangle$ and $|L\rangle$, it can be focused into two circular polarized focal spots with opposite helicity after interacting with the designed metasurface (Fig.4.2.b).

Figure4.6 displays the focusing properties of dual-focal metalenses with flexible focal spots at the designed wavelength of 358 nm. As it can be seen, the focusing profiles based on this design system are completely tunable and manipulatable. For the first type of dual-focal metalens, we set the designed focusing parameters as: (x_i=-x_j= -2 μm, y_i=y_j= 0 μm, f_i=f_j= 4.5 μm) to generate symmetric focal spots along propagation direction. Simulated normalized intensity distributions in the x-z plane (at y=0) and x-y plane at (z=f) are shown in Fig.4.6 (a-b). It is worth mentioning that two focal spots with opposite polarization states ($|L\rangle$ at x_i= -2μm and $|R\rangle$ at x_j= 2μm) are observed at the focal length of 4.98 μm. A small deviation from the designed focal length is observed due to imperfect phase realizations. Both the focal spots are symmetrically distributed in the x-y plane with identical diffraction-limited FWHM of 300 nm Fig.4.6 (c). To examine the capability of the proposed metalens to focus the incident beam into asymmetric focal spots pattern along longitudinal and transverse directions simultaneously, we set the focusing parameters as: (x_i=-x_j= -2 μm, y_i=y_j= 0 μm, f_i= 4.5 μm, f_j= 6.5 μm) and (x_i= 2 μm, x_j= 0 μm, y_i=y_j= 0 μm, f_i= 4.5 μm, f_j= 6.5 μm) for the second and third kind of dual-focal metalens, respectively. Figure4.6 (d and g) shows the normalized intensity distributions of the corresponding metalens in the x-z plane (at y=0). The simulated focal length for the second one are found as 4.98 μm ($|L\rangle$ at x_i= -2 μm) and 6.89 μm ($|R\rangle$ at x_j= 2 μm). Also, for the third one the focal lengths are 4.9 μm ($|L\rangle$ at x_i= 2 μm) and 7 μm ($|R\rangle$ at x_j= 0 μm). The normalized intensity profiles in the corresponding z=f plane for these metalenses are shown in Fig.4.6 (e and h), respectively (One time we set the monitor at z=4.98 and 4.9μm, and one time we put it on z=7 and 6.89μm. The simulated intensity profiles in the x-y plane presented at Fig.4.6 (e and h) are a combination of each two corresponding monitors for each metalens). All the focal spots are of high quality and uniformly distributed in a Gaussian-shaped profile in the transverse plane. The corresponding FWHM values are found as 310 and 300 nm for $|L\rangle$, and 350 and 330 nm $|R\rangle$, respectively, as depicted in Fig.4.6 (f and i). Comparison of these metalenses

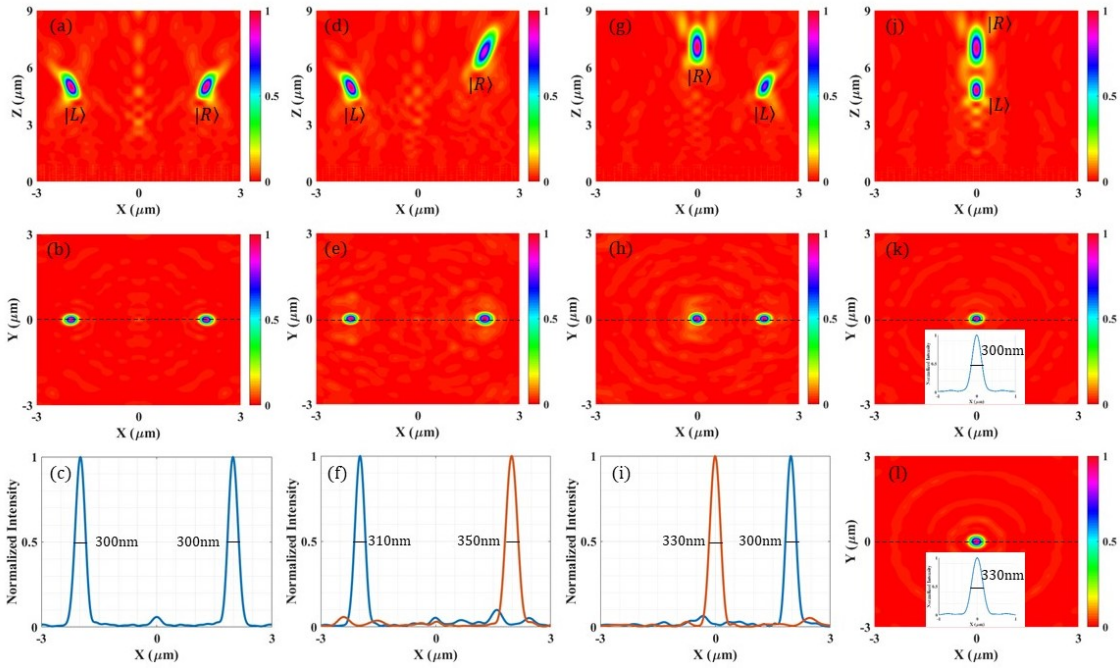

Figure 4.6: Normalized simulated intensity profiles for dual-focal metalens operating at the designated wavelength of 358 nm with adjustable focal pattern in the x-z plane. **(a,d,g,j)** Normalized intensity profiles of the focal spots of the tunable dual-focal metalenses in x-z plane (at y = 0) yielding focal spots at different designated positions along x-z plane. **(b,e,h,k,l)** show Normalized intensity profiles of the focal spots for the dual-focal metalenses in x-y plane at relevant z = f value.(**b** for the structure **a**,**e** for the structure **d**, **h** for the structure **g**) **(c,f,i)** Normalized intensity distribution of focal spots along x-axis at y=0 (horizontal dashed lines in e-g) with diffraction limited FWHM values for corresponding structures. **(k, l)** Normalized intensity profiles of (j) in x-y plane at relevant z=f value with subsets giving the intensity distribution along the horizontal dashed lines with corresponding FWHM values. All the designed metalenses have the same diameter of 10 μm, and are illuminated with linearly polarized light source.

shows the design tunability that can be served to construct these metalenses. The design system is completely manipulatable, and the position of each spot with each $|L\rangle$ or $|R\rangle$ polarization can be easily modified based on our purpose. At the end, for the fourth kind of dual-focal metalens, we set the focusing parameters as: (x_i=x_j= 0 μm, y_i=y_j= 0 μm, f_i= 4.5 μm, f_j= 6.5 μm) to achieve both the focal spots in the longitudinal direction, on central vertical axis along with z-direction. Figure 4.6 (j) presents the normalized intensity distributions in the x-z plane (at y=0). The simulated focal spots are found at z=4.8 μm ($|L\rangle$) and z=7.02 μm ($|R\rangle$). Both focal spots are tightly confined in a circular shape, as shown by corresponding normalized

intensity profiles in the x-y plane at z=f in Fig. 4.6 (k-l), respectively. The subsets in Fig.4.6 (k-l) depict the relevant intensity distributions of the focal spots along the x-direction at y=0 (horizontal dashed lines), with diffraction-limited FWHM of 300 and 330 nm. The simulated focusing efficiency of all the four metalenses is found between 30-40%.

Summarizing the dual-focal focusing properties of the proposed metalens, we can conclude that the studied metalenses not only can focus the incident beam into dual-focal channels with opposite spin, but also tend to manipulate the focal position along any direction without losing the focused beam quality.

More importantly, these smooth-tunable properties can facilitate the applicability of these lenses to perform as a polarization filter for linear polarized illumination. This capability will allow us to filtrate the light based on their handedness in any desired position at the far-field. On the other hand, focusing the light with opposite spins in two independent channels will provide the opportunity to entrap and rotate the particles in the two distinct directions [116]. This particle rotation resulting from the torque implemented by light angular momentum could be anticlockwise or clockwise. ($|L\rangle$ or $|R\rangle$)

4.6 Quad focal

In this section, we demonstrate the quad-focal points metalenses designed based on regional phase engineering to provide a more comprehensive realization of the tunability property of these lenses. As illustrated in Fig.4.2 (c), in order to achieve a quad focal pattern, we divide the metalens area into two regions: one circular region in the center as an inner section with a radius of r_1 and one ring around it as an outer section defined as $r_1 < r \leq r_2$. Both regions are composed of Al_2O_3 nanoblocks, which are placed on the Al_2O_3 substrate. Therefore by taking advantage of Eq.4.3, we can modify the nanoblocks arrangement for each region separately in order to have four focal points. Figure 4.7 shows the top view of different nanoblocks' arrangement in each region. Thus, the phase distribution for each section will be different. Hence Eq.4.3 can be rewritten for inner and outer zones accordingly:

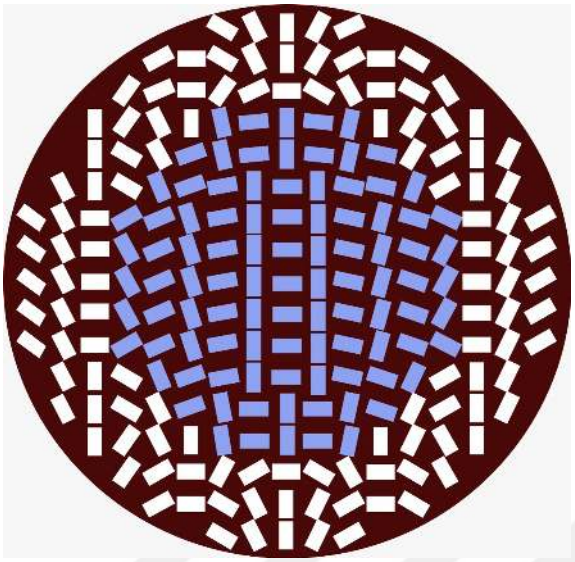

Figure 4.7: The top view of Quad-focal metalenses. All nanoblocks are identical and they are composed of Al_2O_3. The different color of nanoblocks shows the arrangement difference in each region based on regional designing method.

$$\varphi_{df1}(x,y) = arg[e^{i\varphi_{i1}} + e^{i\varphi_{j1}}] \ (0 \leq r \leq r_1) \tag{4.4}$$

$$\varphi_{df2}(x,y) = arg[e^{i\varphi_{i2}} + e^{i\varphi_{j2}}] \ (r_1 < r \leq r_2) \tag{4.5}$$

Where $\varphi_{df1}(x,y)$ and $\varphi_{df2}(x,y)$ will be used to phase engineering of inner and outer regions respectively. Thus by changing the parameters of φ_{i1}, φ_{i2}, φ_{j1} and φ_{j2}, we can modify the position of focal spots in X,Y and Z directions. Based on what we mentioned in previous section, we can consider $\varphi_{df1}(x,y)$ and $\varphi_{df2}(x,y)$ independently to manipulate the orientation of nanoblocks in inner and outer zones, in order to focus the $|LP\rangle$ illumination into the four focal points: two with $|R\rangle$ helicity and two with $|L\rangle$. Therefore, the rotation angle for each nanoblock (θ) at each specified (x,y) position can be written in the form of θ_1=$\varphi_{df1}(x,y)/2$ for internal section and θ_2=$\varphi_{df2}(x,y)/2$ for external section.

On the other hand, the area of each section plays a crucial role in the focal points specifications. The relation between r_1 and r_2 in some of previous works done with this regional designing strategy was considered $r_2 = \sqrt{2} \times r_1$ [109, 111]. As a result, the area of each section is the same to ensure that each part will receive the uniform energy flux. Consequently, the energy of each focal spot, which is dependent on

the area of the sections, will be analogous. However, in this study after a precise optimization process, we modify the ratio between r_1 and r_2 to $r_2 = \sqrt{2.25} \times r_1$. Here, we change the proportion of areas to minimize light interference, which is due to the phase variation between the regions. As the position of designed focal spots and also the zone they stem from can affect their interference, for other focusing patterns, the optimum ratio between r_1 and r_2 could be different. However, for the patterns we are presenting, this ratio ($r_2 = \sqrt{2.25} \times r_1$) is the best one in which all the spots have their maximum possible intensity.

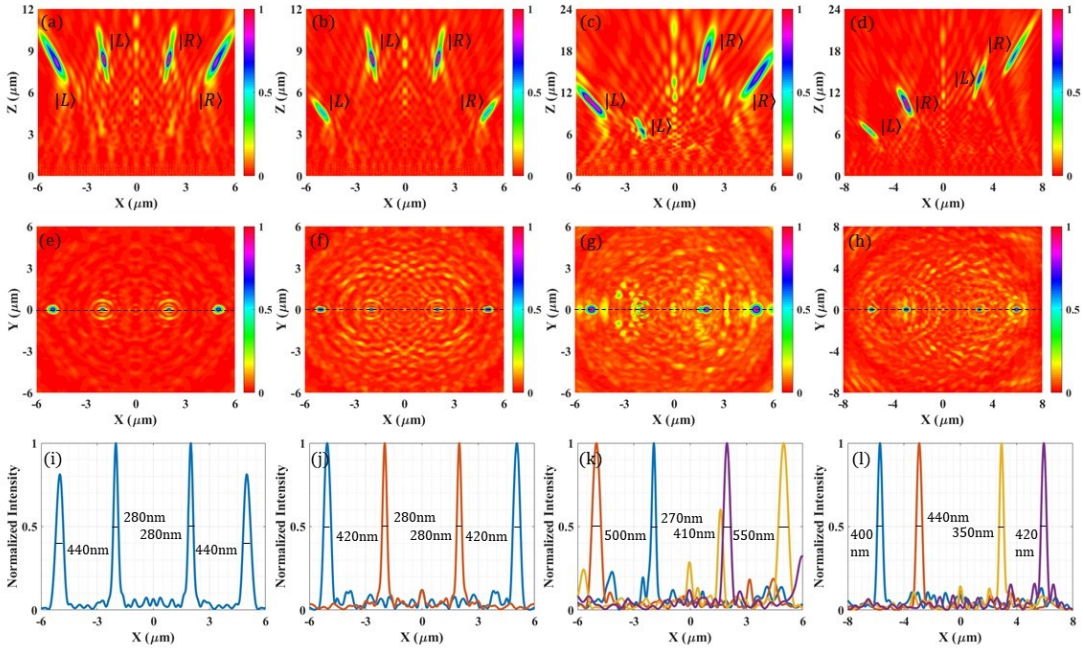

Figure 4.8: Simulated intensity profiles for the quad-focal metalens working at the designated wavelength of 358 nm with tunable focal spots pattern. **(a–d)** Normalized intensity profiles of the focal spot of the tunable quad-focal metalens in x–z plane (at y = 0) yielding focal spots at different designated positions along x–z plane. **(e–h)** Normalized intensity profiles of the focal spots in x–y plane at the relevant z = f value. **(i–l)** Normalized intensity distribution of focal spots along x-axis at y=0 (horizontal dashed lines in e-h) with corresponding diffraction limited FWHM values. The diameter of designed metalenses for (a-c) is 15 μm and for (d) is 16.5 μm. All of the metalenses are illuminated with linearly polarized light source.

Figure4.8 demonstrates the focusing patterns of the metalenses designed based on this engineering strategy at λ=358 nm. For all of the lenses in this figure, we

use $\varphi_{df1}(x, y)$ to phase engineering of the Central region, and $\varphi_{df2}(x, y)$ is used for the outer ring. The first type of these quad-focal metalenses (Figure4.8 (a,e)) has a symmetric schema in which all the focal points are located on a horizontal line. The diameter of this lens is 15 μm and all focal length values (f_{i1},f_{i2},f_{j1} and f_{j2}) is set 8 μm. Also, we consider y_{i1}=y_{i2}=y_{j1}=y_{j2}=0 while x_{i1}=-x_{j1}=5 and x_{i2}=-x_{j2}=2. The simulated normalized intensity distributions in the x-z plane (at y=0) and x-y plane at (z=f) are shown in Figure4.8 (a,e) for this lens respectively. Here the polarization state of the the spots at x_{i1} and x_{i2} is $|R\rangle$, and at x_{j1} and x_{j2} is $|L\rangle$. The simulated focal length for two internal spots is 8.358 μm and for two outer points is 8.13 μm which shows a low deviation from the designed focal length. The different focal deviations between these points are due to the zone from which they originate. Also, the corresponding FWHM for this metalens is calculated and depicted in Figure4.8 (i), in which the FWHM of two outer spots (440 nm) is different from two inner spots (280 nm) because of the same reason mentioned above. For the second design, a trapezoidal focal pattern is presented. In this design, all the parameters are similar to the previous one except f_{i1} and f_{j1} that are set 4 μm. Fig4.8 (b,f) illustrate the simulated normalized intensity distributions in the x-z plane (at y=0) and x-y plane at (z=f) for this lens separately. The simulated focal length for two inner spots is the same as the previous case (8.35 μm) and for two spots at corners is 4.45 μm which shows a low focal aberration again. Also, the results for FWHM calculation Fig4.8 (j) depict 280 and 420 nm for two internal and two outer focal points, respectively. In the third case, an asymmetric focal pattern is shown in which each spot has a unique focal length. Here we set f_{i1}=14 μm, f_{j1}=10 μm, f_{i2}=18 μm and f_{j2}=6 μm. All the other parameters have been set to be the same as the previous models. The status of focal points are demonstrated in Figure4.8 (c) (simulated normalized intensity distributions in the x-z plane at y=0) and Figure4.8 (g)(simulated normalized intensity distributions in the x-y plane at z=f). The simulated focal length for each f_{i1},f_{j1},f_{i2} and f_{j2} is also calculated which are respectively 14.2, 10.9, 17.6 and 6.4 μm. Actually, this asymmetric focal spots' arrangement intensifies the phase realization imperfection, making the aberration from the designed focal length a bit more for some spots. The polarization status

for each point is similar to the previous cases, and their FWHMs form left to right, as measured in Figure4.8 (k) are 500, 270, 410, and 550 nm. It is also worth mentioning that the deviation of focal spots in x direction from the designed values for all of these three metalenses is almost negligible (at most $\pm 0.2\mu$m).

Finally for the last design, we increase the diameter of the lens to the 16.5 μm and also x_{i1}, x_{i2}, x_{j1} and x_{j2} has been changed to -3, 6, -6 and 3μm respectively. Moreover, the focal lengths are designed to be f_{i1}=10μm, f_{j1}=6μm, f_{i2}=18μm and f_{j2}=14μm. Other specifications are set the same as former cases. As it can be seen in Figure4.8 (d), which shows simulated normalized intensity distributions in the x-z plane at y=0, the dispersion of focal spots based on their polarization is different from others. Here, same as the prior metalenses, the linear polarized UV is illuminated to the lens. However, the polarization state of focal spots are different with the previous lenses, and there is one pair of $|R\rangle$-$|L\rangle$ polarized points in right half-spaces (at x_{i2} and x_{j2}) and one pair in the left half (at x_{i1} and x_{j2}). This arrangement varies with the previous ones in which $|R\rangle$ polarized points were located at the right half part, and $|L\rangle$ were placed at the left half. Also, Figure4.8 (d) illustrates that diameter's increment and increasing the distance between two inner spots, in addition to this polarization arrangement of the focal spots, decrease unwanted intensity concentration in the x-z plane except at focal points. This decrements is visible when we compare Fig4.8 (d) with the other ones (Fig4.8 (a,b,c)). The normalized intensity profile in the corresponding z=f plane for this lens is shown in Figure4.8 (h), and FWHM for each point is calculated in Figure4.8 (l). The deviation of focal spots in x direction is less than 0.1 μm for all the points except the focal site designed for x_{i2}, which has 0.4 μm shift to the left (simulated x_{i2} is 5.6 μm). Also, the simulated focal length are calculated which are f_{i1}=10.37μm (FWHM=440nm), f_{j1}=6.38μm (FWHM=400nm), f_{i2}=17μm(FWHM=420nm) and f_{j2}=14.05μm(FWHM=350nm).

In the end, to abridge these quad focal metalenses, we can mention that this phase engineering method provides a capability to focus the linear polarized UV light into four channels, in which each two have the same angular momentum. Therefore, continuing the discussion presented at the end of the previous section, we can double

the channels to filtrate the UV light based on their helicity, giving higher freedom for this separation. More importantly, extending this design technique, one can have more focal points in which half of them are $|R\rangle$ and half of them are $|L\rangle$ polarized for further applications.

Chapter 5

LENS FREE SPECTROSCOPIC SYSTEM: PLASMONIC WITH METALENSES

Plasmonic arrays and metalenses are vastly studied in these years. However, the idea of integration of these two metasurfaces has not been investigated yet. This section proposes integrated metalens-plasmonic devices to exploit the advantages of both structures in one system. After numerical analysis, we found the high potential applicability of these devices in various applications such as molecular sensing, polarization visualizer, selective excitation, photodetectors, hot electron generation.

5.1 Overview

The illumination of plasmonic nanostructures usually is done by using an external lens. Therefore, it is very important to optimize the lens-chip distance to bring the plasmonic array to the focal region. On the other hand, based on the functionality of these external conventional lenses, selective chip and single cell illumination is a challenging procedure. More importantly, the localized field enhancement happens in the plasmonic structures is an crucial parameter defines the precision and sensitivity of these systems in different applications. On the other side of the coin, Metalenses based on PB phase are another type of metasurfaces which focus the incident circular polarized light into a focal point with opposite polarization. But there is no system has been introduced yet to visualize this polarization conversion induced by PB-based metalenses and their operational efficiency. So far, we studied the focal shift effect and multifocal metalenses in previous chapters. However, we did not show an intangible aspect of the applications regarding these investigations.

In this chapter we present an integrated metalens-plasmonic chip which can pave

the way for lens-free illumination of plasmonic structure. Here a metalens is embedded on the backside of a chip and the plasmonic pattern is designed on another side of that chip. Hence, we can radiate our plasmonic nanoantennas without any external lens. Also, by taking advantage of this system we can selectively illuminate a couple of single antennas on the chip based on the designed metalens. On the other hand, utilizing a multifocal metalens allow us to excite several chips on the surface with different polarization simultaneously. In this regard, we can use this system to filtrate and visualize the incident light polarization. More importantly, using this compact device system, greatly increase the field enhancement in plasmonic structures and boost the sensitivity of these nanostructures for biosensing applications. As the metalenses focus the light in a specific region, the power accumulation accomplished by the metalens locally increase the field enhancement. Based on our design purpose, we can play with nominal the NA to manipulate the area of field enhancement; lower the NA, higher the region, and vice versa. On the other hand, regarding what we discussed in chapter 3, playing with NA means changing the corresponding focal shift value while anticipating the focal shift is very crucial here to get the maximum efficiency. The thickness of the substrate should be determined by considering the focal shift effect. Finally, taking all these features into account, we can utilize these compact devices as suitable choices for chiral biomolecules sensing with higher precision.

In the following sections, we review the chiral plasmonic structures and then, we numerically investigate our proposed integrated device for different applications.

5.2 Chiral plasmonic structures

The asymmetricity in which the object and its mirror can not be superimposed is named chirality, and that object is called chiral. Our hands are the obvious example of chiral objects in which the left hand and right hand can not be superimposed. Chirality plays a crucial role in our daily life, and the activity of many chemical and pharmacological molecules is dependent on this property [117, 118].The chiral molecules and their opposite mirror image, which are known as enantiomers, have

the same stoichiometric molecular formula; however, they have different handedness (left(L) and right (R)). The distinction of enantiomers is significant in biology and pharmaceutics since the handedness of enantiomers may differentiate the metabolic profile and functionality of drugs and biomolecules [119, 120, 121].

As the chiral molecules have the same chemical composition and scalar physical properties, the discrimination of their handedness is possible by investigating their interaction with other chiral objects. Circularly polarized light (CPL), divided into left and right-handed polarization, is one of the most common ways to distinguish and separate chiral objects [122, 123]. However, because of the mismatch between the size of molecules and the wavelength of CPL, the realized chiral dichroism (CD) by chiral molecules is relatively low (around tens of millidegrees in UV region), and this is a significant limitation to use this method for small molecules or low-volume samples [123]. In this regard, taking advantage of plasmonic nanostructures which can confine the light in sub-wavelength dimensions is a promising method to enhance the chiroptical signal [124, 125, 126]. As a result of light-matter coupling in chiral plasmonic structures, the chiral near-field is enhanced, and hence, the interaction of chiral molecules with this boosted electromagnetic field eventuate in a higher CD signal [127].

To realize the effect of field enhancement in CD increment, we start by formulating the electric ($\tilde{p}$) and magnetic ($\tilde{m}$) dipole moment of a chiral molecule under monochromatic, time-harmonic, and low-intensity electromagnetic field. We can write[118]:

$$\tilde{p} = \tilde{\alpha}\tilde{E} - i\tilde{G}\tilde{B} \tag{5.1}$$

$$\tilde{m} = \tilde{\chi}\tilde{B} + i\tilde{G}\tilde{E} \tag{5.2}$$

Here, $\tilde{\alpha}$, $\tilde{G}$, and $\tilde{\chi}$ are the complex electric polarizability, mixed electric-magnetic dipole polarizability, and magnetic susceptibility, respectively. Also, $\tilde{E}$ and $\tilde{B}$ are the local electric and magnetic fields at the target chiral molecule. Now, if we want to calculate the absorption of light accomplished by the molecule, it can be written

as:

$$A^{\mp} =< B \cdot m + E \cdot p >= \frac{\omega}{2}\left(\tilde{\alpha}''\left|\tilde{E}\right|^2 + \tilde{\chi}''\left|\tilde{B}\right|^2\right) \pm \frac{2}{\varepsilon_0}\tilde{G}''C \tag{5.3}$$

In 5.3 the (+) and (-) sign refer to the right and left handeded polarized light, respectively and the $\tilde{\alpha}''$, $\tilde{\chi}''$ and $\tilde{G}''$ are representative for the imaginary part of $\tilde{\alpha}$, $\tilde{\chi}$ and $\tilde{G}$, in a same order. The chiral density is also shown by C and it is given by [128, 118]:

$$C = \frac{\varepsilon_0}{2}E \cdot (\nabla \times E) + \frac{1}{2\mu_0}B(\nabla \times B) = -\frac{\omega\varepsilon_0}{2}Im(\tilde{E}^* \cdot \tilde{B}) \tag{5.4}$$

Where the μ_0 and ε_0 are permeability of free space and permittivity. Now we can find the CD that is the difference of molecule's absorption while RCP and LCP illumination. it means that [129]:

$$CD = A^+ - A^- = \frac{4}{\varepsilon_0}G''C \tag{5.5}$$

On the other hand, based on 5.4, the maximum value of C can reaches to the $C^{\pm}_{CPL}$=$\pm\frac{\omega\varepsilon_o}{2}|E|^2$ [130]. Here, $|E|$ is the amplitude of incident CPL.Therefore, with all these taken to account, we can realize that exploiting engineered plasmonic nanostructures, which can manipulate the light-matter interaction in a way to make localized-enhanced electromagnetic fields, can boost the C value, and based on 5.5, the increment of C will result in a higher CD signal. In this regard, as the chiral molecules themselves usually show a very low CD against CPL incident, the chiral plasmonic structures are suitable choices to ease the selective light absorption by the molecule [131].

There are different plasmonic chiral nanostructures are proposed and successfully tested for biosensing applications [122, 118, 119, 132, 129].However, these chiral nanostructures can be utilized for asymmetric hot electrons (HEs) generations in addition to sensing applications [133, 134, 135]. These generated hot electrons can prompt surface reactions, and they have applicability in polarization-sensitive photochemistry and chiral photocatalysis application [133].

5.3 Principles

In this section, we numerical investigate our proposed compact device. This compact device comprises one metalens structure on the backside and a chiral plasmonic structure on the other side. As illustrated in fig.5.1 (a), the light is passing through the metalens and is focused on the plasmonic structure. Both structures are patterned on the CaF_2 substrate.

5.3.1 Design details

As shown in fig.5.1 (b), we are using a periodic left-handed (LH) spiral pattern, which is etched into an Au layer as the chiral plasmonic structure in this compact device. The periodicity of these spirals is $2.4\mu m$, and the spiral's start and end radius is 100nm and 900nm, respectively. Also, the number of spiral turns is set to be 1.6. These spirals are patterned into a 100nm thick gold layer which is placed on the top-center of the substrate (CaF_2). We use a 5×5 periodic spiral pattern as our plasmonic structure in the simulation process due to the memory limitation.

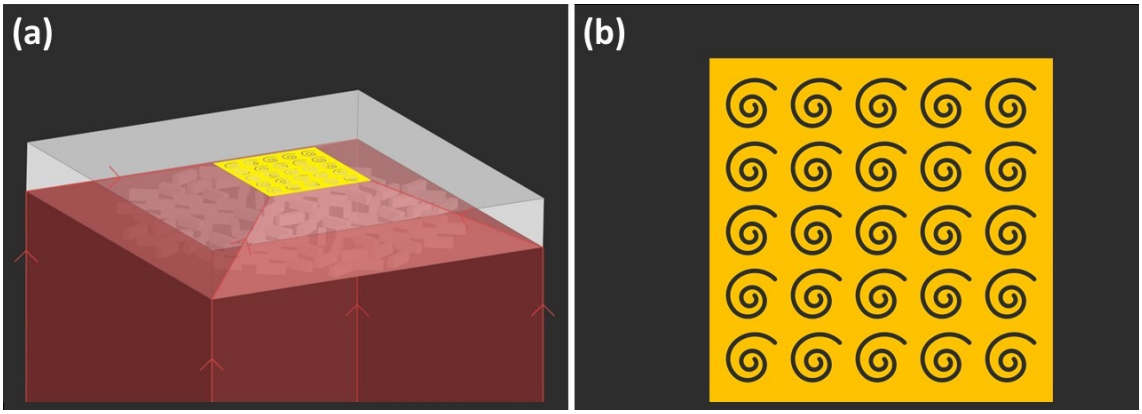

Figure 5.1: **a** The schematic of the working principle of the proposed integrated device for biosensing. The metalens nanoblock in the backside and plasmonic nanostructuture on the top can be observed in the figure.**b** The spiral shape periodic aperture on a gold layer which used as plasmonic nanostructure

As illustrated in figure5.2 (a), these LH-spirals have a resonance in their absorption spectrum near $6\mu m$ for both LCP and RCP source illumination. Because of the chiral shape of these LH-spirals, they show a strong CD signal as presented in

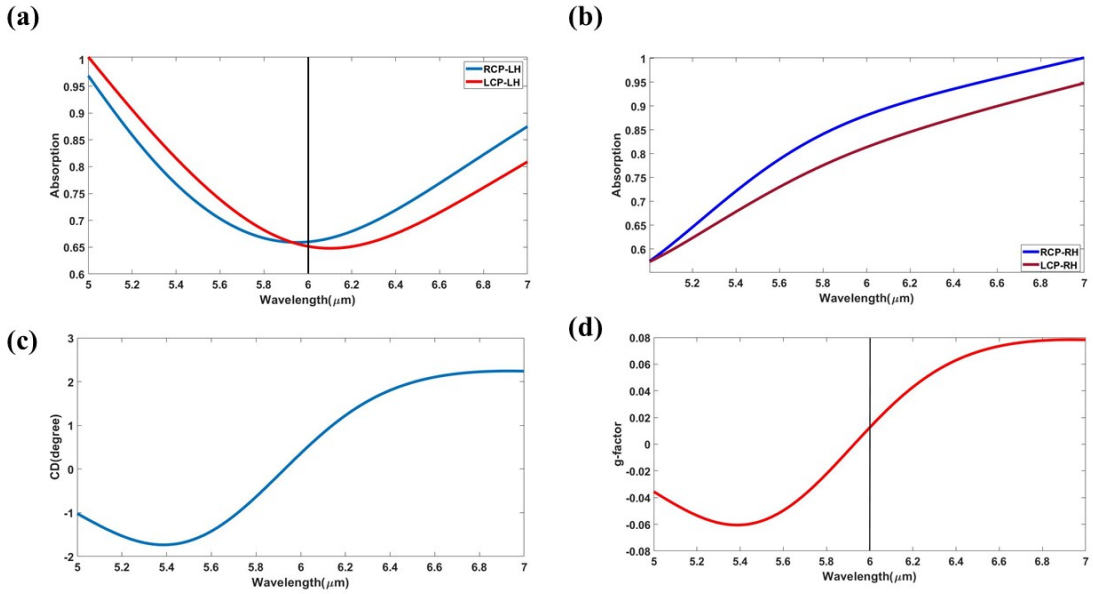

Figure 5.2: **a , b** Absorption spectrum for the LH and RH spiral under RCP and LCP illumination, recpectively. **c** The calculated CD signal and **d** and g-factor for the LH spirals.

Fig.5.2 (c). This CD signal is around 1 degree, and it is much higher than the CD signal of chiral molecules, which is about tens of millidegrees [118, 129]. To calculate the CD signal for these LH spirals, we can use the eq.5.6 [136, 123]:

$$CD = tan^{-1}\left(\frac{A_{LCP} - A_{RCP}}{A_{LCP} + A_{RCP}}\right) \tag{5.6}$$

In this equation, the A_{LCP} and A_{RCP} are the absorption of LH-spiral under LCP and RCP illumination, respectively. We also calculated the absorption of right-handed (RH) spirals under RCP and LCP radiation which is presented in figure.5.2 (b). It can be seen that there is no resonance peak can be observed for these RH spirals. It is worth mentioning that to calculate the absorption of these spirals, we do our simulations in the FDTD region for one unit cell. The unit cell contains one LH (RH) spiral etched into a gold layer with 100 nm thickness while the dimension of the unit cell is equal to is $2.4\mu m$ in both x and y-direction. The periodic boundary condition is applied in both x and y directions, and the PML boundary condition is set for z-direction. Then we illuminate the structure from the back, one time with LCP source and one time with RCP source. Light passes from the CaF_2substrate and

interacts with the spiral aperture on the top. After calculation the transmission and reflection in each step, we can measure the corresponded absorption for each structure under LCP/RCP illumination (Absorption (A)=1-Transmission (T)-Reflection (R)).

From the absorption data, we can also calculate the $g-factor$, which is a parameter to characterize the chiral structures, and it is given by [119, 133]:

$$g-factor = 2 \times \frac{A_{LCP} - A_{RCP}}{A_{LCP} + A_{RCP}} \tag{5.7}$$

The $g-factor$ is calculated for the LH-spiral based on the previous equation. Figure5.2 (d) shows a value in the order of 10^{-2} for the $g-factor$ of these LH-spiral, which is around 10^5 times higher than the typical calculated value for the asymmetry of chiral molecules in solution, when measured by bare circularly polarized light [119, 137].

5.3.2 Lens structure design

The designed LH-spiral has a resonance frequency at $6\mu m$. Therefore, to amplify the expected near field provided with this structure, we use a metalens at the backside of the substrate, which focuses the light at $6\mu m$. More importantly, since we aim to take advantage of our proposed compact device at both RCP and LCP illuminations, we should design a hybrid metalens in the backside. Hence we design a hybrid metalens based on PB phase with rectangular nanoblcoks working at $6\mu m$. The material of nanoblocks is Ge, and the dimension of each nanoblock is $1.87\mu m$ for height, $3.5\mu m$ for length, and $0.74\mu m$ for the width, and the periodicity is $3.8\mu m$. The procedure for designing metalens is similar to what we did in previous chapters. The calculated PCE is around 1 at $6\mu m$, and the full phase coverage is satisfied. Figure5.3 shows the electric field squared ($|E|^2$) distribution of designed metalens in x-z direction at y=0 plane under LCP (Fig.5.3 (a)) and RCP (Fig.5.3 (b)) illumination. The diameter of designed metalens is set to be $50\mu m$, and the designed NA is 0.64. The focal length here is the thickness of the substrate, and it is equal to $30\mu m$. It means that the irradiated light is focused on the LH-spiral structure on the top of the substrate surface. It worth mentioning, since the propagation of light after pass-

ing from the lens is accomplished in the CaF_2 medium, we divided the fundamental equation for design PB phase metalens (2.6) by the value of CaF_2 refractive index (n=1.42). Figure5.3 (c,d) also depicts the FWHM of the designed lens under LCP

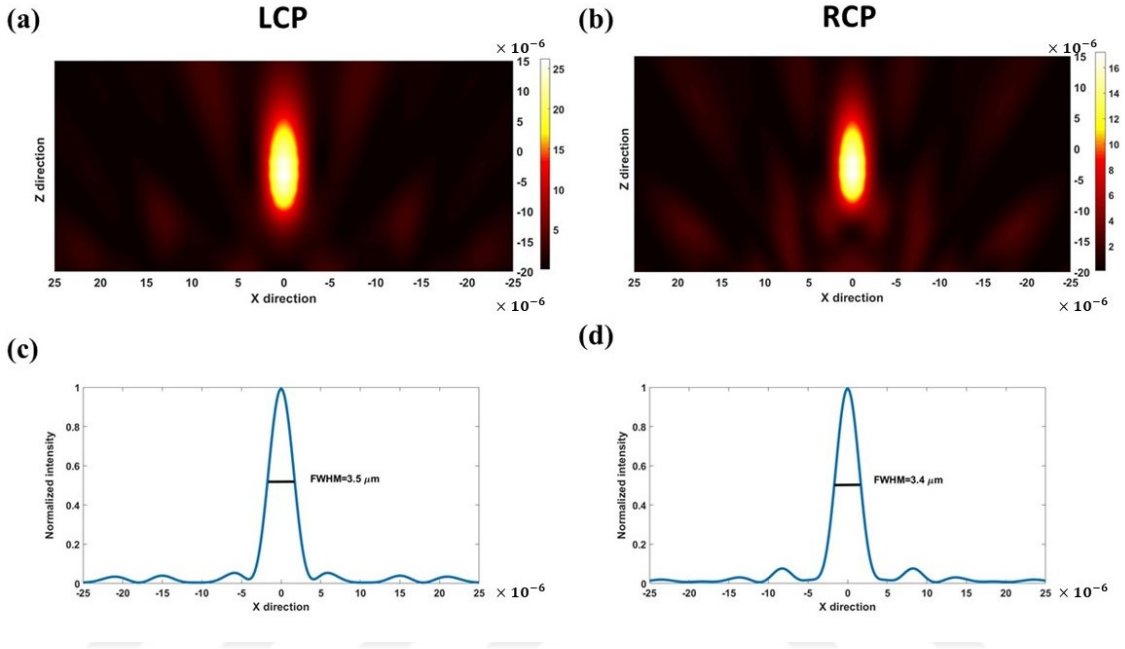

Figure 5.3: **a and b** The electric field squared ($|E|^2$) distribution of the designed hybrid metalens operating at $6\mu m$ in x-z direction at y=0 plane, illuminated by LCP and RCP, respectively.**c and d** The normalized intensity distribution for each lens in x-y plane at z=f along x-direction while y=0, illuminated by LCP and RCP, respectively. The FWHM is depicted for each lens.

and RCP illumination. Here, the FWHM is very important. The FWHM of lens for LCP and RCP illumination is $3.5\mu m$ and $3.4\mu m$, respectively. Based on the focusing efficiency formula, the focusing forehead on the substrate surface, which plasmonic nanostrucure is designed there, can cover a region with a radius of 3 times FWHM with gradient intensities. Although the maximum intensity happens in the center of the focal spot, we still have power accumulation up to the 3×FWHM far from the focal point center. Considering the figure5.3 (a,b), we can find out that the focused power is around $\frac{1}{5}$ of maximum intensity, in the distances equal to 3×FWHM from the Central focal spot.

5.3.3 Results and discussion

This section compares the results of the LH-spiral plasmonic nanostructures in the integrated device and ones without integration with metalenses. Figure5.4, Figure5.5 and Figure5.6 depict the normalized near electric field square ($\left|\frac{E}{E_0}\right|^2$), normalized electric field ($\left|\frac{E}{E_0}\right|$) and normalized magnetic field ($\left|\frac{H}{H_0}\right|$) distribution of the chiral plasmonic structure under LCP and RCP illumination, respectively; one time with lens (in the compact device) and one time without lens. As it can be seen in fig.5.4 (a,b), the near field distribution of plasmonic spiral pattern under LCP and RCP radiation is different from each other, and they are distinctive. Figure5.5 (a,b) that shows the electric field distribution of spiral structure under LCP and RCP illumination can give rise to a better understanding of this difference. The electric field is enhanced in the outer branch, while the LCP light radiance and it is enhanced in the inner branch when the RCP light is illuminated. The concentration of magnetic field also is at the end of outer branch for LCP light (fig.5.6 (a)) and at the end of inner branch for RCP light (fig.5.6(b)). The distribution of field is completely uniform, and field enhancement happens strongly based on the source polarization. Note that to have a better comparison with the compact device, we illuminate the bare plasmonic (without lens) structure from the backside, and light passes through the CaF_2 substrate toward the spiral structure. However, when we are using the proposed compact device to illuminate the plasmonic structure with a lens, the fields distribution change.

The (c) and (d) label subfigures in Fig.5.4, Fig.5.5 and Fig.5.6 represent the near field, electric field, and magnetic field distributions of the chiral plasmonic structure in the compact device while LCP and RCP light are illuminated through the metalens, respectively.

It can be seen clearly that the field confinements are enhanced sharply compared to ones illuminated without the lens. But, more importantly, as the incident circular light experience a polarization conversion while passing through the metalens, the distinctive field distribution pattern that happens within the plasmonic nanostructure irradiated without lens is entirely different from those are lightened with

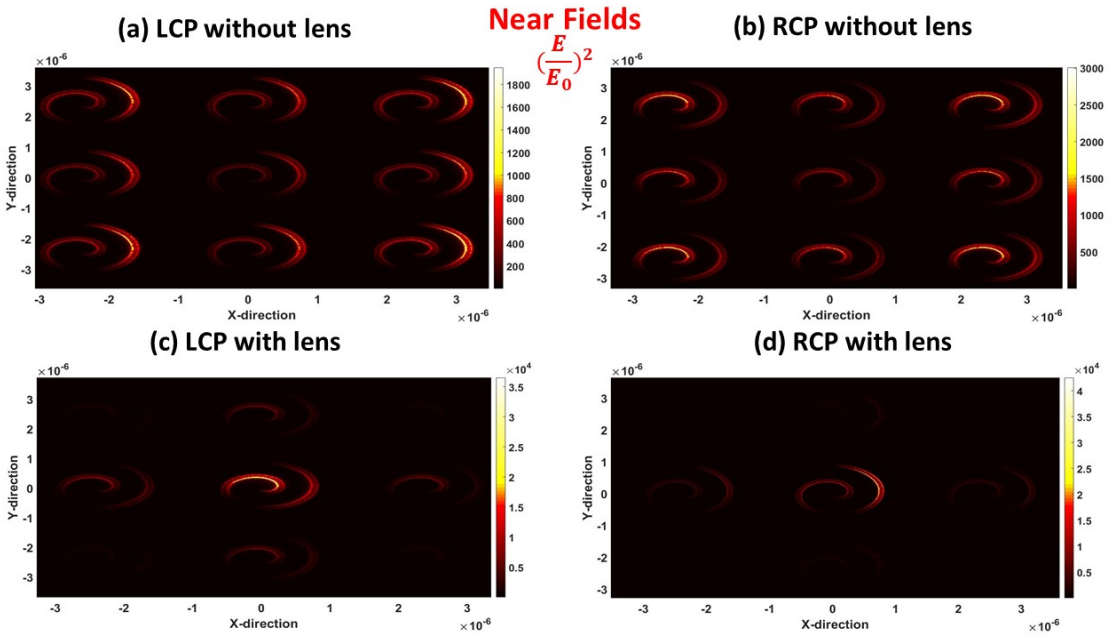

Figure 5.4: The normalized near electric field ($\left|\frac{E}{E_0}\right|^2$) distribution of chiral plasmonic structure under LCP(**a**) and RCP(**a**) illumination without lens.**c** (for LCP sourc) and **d** (for RCP source) shows the near field distribution of the plasmonic structure in the compact device while lens used to illuminate the light. The results were taken at the height of 100nm from substrate.

metalens. Here, the field distribution is the opposite with ones illuminated without lens; maximum in the inner layer for LCP and utmost when shone with RCP. This is the clear visualization of polarization conversion that happens through the metalens. It is worth mentioning that the order of maximum field enhancement in these compact device systems can be calculated as a product of the field enhancement of the bar plasmonic structure to the focal power of metalens. However, the simulation results are slightly lower than the calculated values due to the scattering phenomena in the interface.

Considering the (c) and (d) label subfigures in fig.5.5, fig.5.4 and fig.5.6, we can explicitly see nonuniform field distribution happens in the structures illuminated through the metalens in compact device platform. As the metalens is designed to focus the light to the central position (x=0,x=0), the near field is at the highest level for the spiral placed in the center. However, as mentioned in the previous subsection

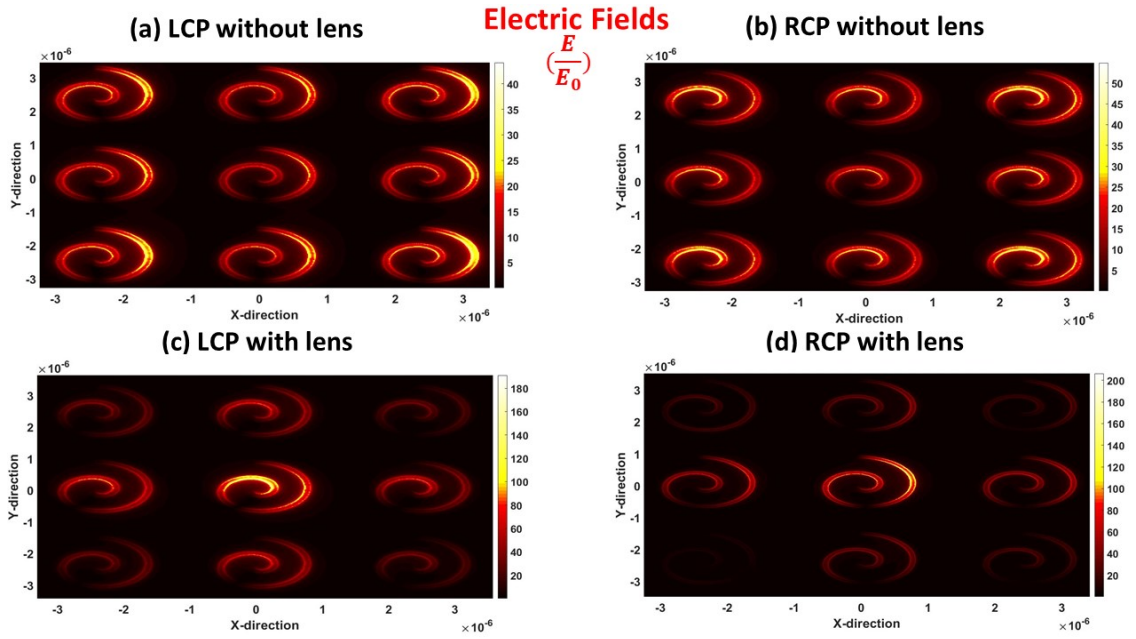

Figure 5.5: The normalized electric field ($\left|\frac{E}{E_0}\right|$) distribution of chiral plasmonic structure under LCP (**a**) and RCP(**a**) illumination without lens.**c** (for LCP sourc) and **d** (for RCP source) shows the electric field distribution of the plasmonic structure in the compact device while lens used to illuminate the light. The results were taken at the height of 100nm from substrate.

(lens design), the focal forehead covers a region up to 3× FWHM. It means that, although the field distribution is nonuniform, the field enhancement for the other spirals in the vicinity of the central spiral can still be higher than those illuminated without metalens. For biosensing applications, a strong coupling between chiral molecules and these chiral-shaped spiral happens, and therefore, calculating the difference between the resonance shift occurs under RCP and LCP illumination results in molecular detection [119, 129]. However, as the CD signal in the chiral biomolecules is low, the high CD signal created by these chiral structures sometimes may make some limitations for detection. In other words, the CD signal of the molecule may be waived in comparison to the intrinsic-strong CD signal of these chiral plasmonic structures. In this regard, the nonuniform field distribution in these compact devices can be considered advantageous for chiral molecule detection. In the next section, we introduce a method to excite different chips with opposite polarization selectively.

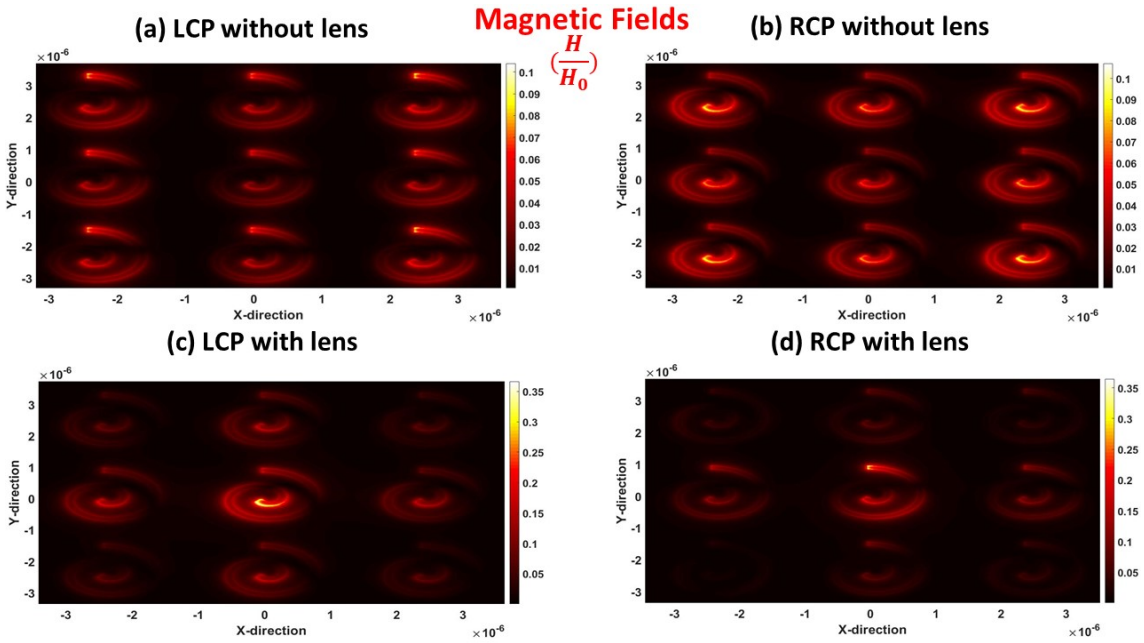

Figure 5.6: The normalized magnetic field ($\left|\frac{H}{H_0}\right|$) distribution of chiral plasmonic structure under LCP(**a**) and RCP(**a**) illumination without lens.**c** (for LCP source) and **d** (for RCP source) shows the magnetic field distribution of the plasmonic structure in the compact device while lens used to illuminate the light. The results were taken at the height of 100nm from substrate.

5.4 Multifocal lens in compact device

Based on what we discussed in the previous chapter, here again we can utilize of multifocal metalenses to in configuration of our proposed compact device. By taking advantage of these kind of metalenses, we can illuminate several plasmonic structures with different polarization modes on the same chip surface, simultaneously. Therefore, not only can we use this for biosensing applications, we can use this device as a polarization visualizer system. Also, we can use this method to generate HEs with different handedness for selectively controlling biological surface reaction.

Figure 5.7 shows an example of the near field pattern of the previous spiral system excited with dual focal metalens. The design principle of metalens is similar to what we did in the previous chapter under the dual focal section. Here the design parameters for the compact device are the same as the single focal one presented before. However, in this system, there are two separated chips designed on the

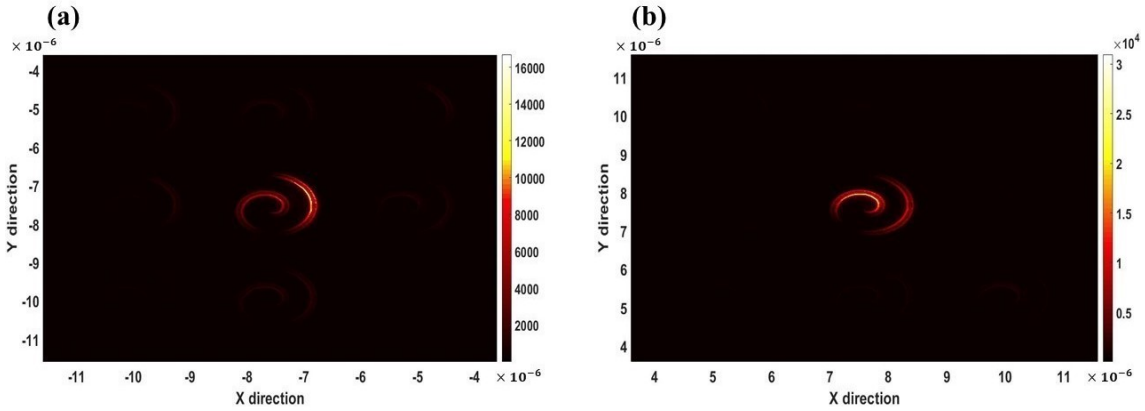

Figure 5.7: The normalized near electric field ($\left|\frac{E}{E_0}\right|^2$) pattern of spiral-shaped plasmoinc structure in the compact device configuration illuminated with linear polarized light while the designed metalens in the backside is dual-focal. Hence each chip on the surface will be excited with opposite handedness.**a** excited by LCP and **b** excited by RCP.

surface in such a way that their central coordinates are located on **x=8**μm**, y=0** and **x=-8**μm**, y=0**. On the other hand, the metalens is designed to focus the light in these central coordinates. Hence, when we illuminate our structure with linear polarized light, each chip will be excited separately with opposite handedness polarization. As illustrated in Fig.5.7, the chip that is located at **x=8**μm**, y=0** (Fig.5.7 (b)) is excited with RCP light and the chip which is placed at **x=-8**μm**, y=0** (Fig.5.7 (a)) is excited with LCP. The near field patterns in both cases presented in figure5.7 clearly show the difference in excited polarization handedness. Extending this configuration with multifocal metalens results in more selective excitation at the same time.

5.5 Summary

In this chapter, we introduced a lens-free illumination system to illuminate plasmonic structures with a compact device. Here, both lens and plasmonic structures are designed on one chip; a metalens is designed on the backside of a chip, and on the other side, a plasmonic structure is patterned. We showed that we could significantly boost the near field enhancement by using this system, which is essential

for biosensing applications, and also take advantage of this device for polarization filter visualizer. Integrating this compact device with multifocal metalenses results in selective excitation of multi chips on the same surface with different polarization modes, which can be crucial for sensitive surface reaction control. The role of focal shift phenomenon was obviously observed to achieve the highest possible efficiency as it is crucial to determine the substrate thickness.

Chapter 6

CONCLUSION

In this thesis, we have investigated the metalenses that are one of the most valuable metasurfaces nowadays. In the last few years, due to the applicability of lenses in the visible region, the metalenses working in this range of wavelengths have been studied extensively. However, working on the metalenses operating at UV and mid-IR region is still immature. On the other hand, the possible advantages of metalens integration with other photonic circuits have not been studied clearly.

Here, by taking advantage of FDTD simulations, we have numerically studied two crucial perspectives of metalenses that define their functionalities: The focal shift phenomenon and multifocal focusing pattern. The first one has been investigated in the mid-IR regime, and the latter has been perused in the UV range. In the end, we have studied the metalens integrated with a plasmonic structure in a single device to have a lens-free illumination system, and then we examined its potential applications.

Unlike the previous studies that believed the Fresnel number is the only parameter associated with the focal shift phenomenon, we showed the numerical aperture (NA) as an effective parameter to predict the focal deviation. We designed metalenses working at 3 and 4 μm, and then we analyzed the focal shift value at each designed NA. The metalenses were designed based on the PB method, and right circular polarized light was used as the incident illumination. After our investigations, we introduced a critical NA (NA_C) in which the focal shift reaches its minimum value. Based on our studies, the NA_C is dependent on the working wavelength (it is around 0.65 for our designs), and its effect on the focal deviation is more evident in the metalenses with lower diameter.

Next, we numerically designed a single-material metalens with a tunable multifocal pattern working in the UV region. Here, the metalens nanoblocks and their

substrate are both from Al_2O_3. We tested our designed metalens at 210, 263, 305, and 368 nm, and it showed great functionality at all of these wavelengths. By taking advantage of new phase engineering methods and regional designing, we could reach a multifocal pattern in which the position of each focal point can be easily adjusted in x, y, and z directions. Based on this design method, a linear polarized light is illuminated to the lens, and then we could have an even number of focal points in which half of them are right circular polarized (RCP), and half of them are left circular polarized (LCP). Here, the number of focal points can be adjusted by the regional designing technique in addition to phase engineering. Due to the tunability of focal spots based on the design parameters, these multifocal metalenses can be great candidates for polarization filters.

In the end, we numerically studied and introduced a lens-free illumination system in which on the one side of the device there is metalens, and on the other side, a plasmonic structure is patterned. We designed our hybrid metalens to operate at 6 μm, which can work under both right and left circularly polarized illuminations. Then, we chose a spiral shape plasmonic structure for the top surface. The resonance wavelength of the spiral shape plasmonic structure is set to be 6 μm under RCP and LCP light. Comparing the functionality of this compact device with the plasmonic system without metalens, we could find a high near-field enhancement as a result of this integration happened in the plasmonic system. Also, we can use this integrated device to illuminate a single unit cell instead of the whole structure. More importantly, by taking advantage of the phase engineering method that we implemented in the UV region, we can use these integrated devices to illuminate multi chips on the surface with different polarization modes.

BIBLIOGRAPHY

[1] Q. Zhang, F. Dong, H. Li, Z. Wang, G. Liang, Z. Zhang, Z. Wen, Z. Shang, G. Chen, L. Dai, *et al.*, "High-numerical-aperture dielectric metalens for super-resolution focusing of oblique incident light," *Advanced Optical Materials*, vol. 8, no. 9, p. 1901885, 2020.

[2] M. Li, S. K. Cushing, and N. Wu, "Plasmon-enhanced optical sensors: a review," *Analyst*, vol. 140, no. 2, pp. 386–406, 2015.

[3] "Lumerical website." `https:lumerical.com/`.

[4] M. Khorasaninejad, W. T. Chen, R. C. Devlin, J. Oh, A. Y. Zhu, and F. Capasso, "Metalenses at visible wavelengths: Diffraction-limited focusing and subwavelength resolution imaging," *Science*, vol. 352, no. 6290, pp. 1190–1194, 2016.

[5] A. V. Kildishev, A. Boltasseva, and V. M. Shalaev, "Planar photonics with metasurfaces," *Science*, vol. 339, no. 6125, p. 1232009, 2013.

[6] C. M. Soukoulis and M. Wegener, "Optical metamaterials—more bulky and less lossy," *Science*, vol. 330, no. 6011, pp. 1633–1634, 2010.

[7] C. U. Hail, A.-K. U. Michel, D. Poulikakos, and H. Eghlidi, "Optical metasurfaces: evolving from passive to adaptive," *Advanced Optical Materials*, vol. 7, no. 14, p. 1801786, 2019.

[8] D. Neshev and I. Aharonovich, "Optical metasurfaces: new generation building blocks for multi-functional optics," *Light: Science & Applications*, vol. 7, no. 1, pp. 1–5, 2018.

[9] E. Arbabi, *Metasurfaces: beyond diffractive and refractive optics*. PhD thesis, California Institute of Technology, 2019.

[10] C. L. Holloway, E. F. Kuester, J. A. Gordon, J. O'Hara, J. Booth, and D. R. Smith, "An overview of the theory and applications of metasurfaces: The two-dimensional equivalents of metamaterials," *IEEE Antennas and Propagation Magazine*, vol. 54, no. 2, pp. 10–35, 2012.

[11] I. Staude and J. Schilling, "Metamaterial-inspired silicon nanophotonics," *Nature Photonics*, vol. 11, no. 5, pp. 274–284, 2017.

[12] J. Scheuer, "Optical metasurfaces are coming of age: Short-and long-term opportunities for commercial applications," *ACS Photonics*, vol. 7, no. 6, pp. 1323–1354, 2020.

[13] P. R. West, J. L. Stewart, A. V. Kildishev, V. M. Shalaev, V. V. Shkunov, F. Strohkendl, Y. A. Zakharenkov, R. K. Dodds, and R. Byren, "All-dielectric subwavelength metasurface focusing lens," *Optics Express*, vol. 22, no. 21, pp. 26212–26221, 2014.

[14] L. Cong, N. Xu, J. Gu, R. Singh, J. Han, and W. Zhang, "Highly flexible broadband terahertz metamaterial quarter-wave plate," *Laser & Photonics Reviews*, vol. 8, no. 4, pp. 626–632, 2014.

[15] K. E. Chong, I. Staude, A. James, J. Dominguez, S. Liu, S. Campione, G. S. Subramania, T. S. Luk, M. Decker, D. N. Neshev, *et al.*, "Polarization-independent silicon metadevices for efficient optical wavefront control," *Nano Letters*, vol. 15, no. 8, pp. 5369–5374, 2015.

[16] V. Egorov, M. Eitan, and J. Scheuer, "Genetically optimized all-dielectric metasurfaces," *Optics Express*, vol. 25, no. 3, pp. 2583–2593, 2017.

[17] S. Larouche, Y.-J. Tsai, T. Tyler, N. M. Jokerst, and D. R. Smith, "Infrared

metamaterial phase holograms," *Nature Materials*, vol. 11, no. 5, pp. 450–454, 2012.

[18] F. Ali and S. Aksu, "A narrow-band multi-resonant metamaterial in near-ir," *Materials*, vol. 13, no. 22, p. 5140, 2020.

[19] N. Yu and F. Capasso, "Flat optics with designer metasurfaces," *Nature Materials*, vol. 13, no. 2, pp. 139–150, 2014.

[20] H. Yu, Z. Zhou, Y. Qi, X. Zhang, and Q.-H. Wei, "Pancharatnam–berry optical lenses," *JOSA B*, vol. 36, no. 5, pp. D107–D111, 2019.

[21] C. Zhang, S. Divitt, Q. Fan, W. Zhu, A. Agrawal, Y. Lu, T. Xu, and H. J. Lezec, "Low-loss metasurface optics down to the deep ultraviolet region," *Light: Science & Applications*, vol. 9, no. 1, pp. 1–10, 2020.

[22] W. Cai and V. M. Shalaev, *Optical Metamaterials*, vol. 10. Springer, 2010.

[23] G. Singh, "R. ni, and a. marwaha,"a review of metamaterials and its applications,"," *International Journal of Engineering Trends and Technology*, vol. 19, no. 6, pp. 305–310, 2015.

[24] F. Ali, *Investigation of dual-narrowband plasmonic perfect absorbers at visible frequencies for biosensing*. PhD thesis, Bilkent University, 2019.

[25] A. Sihvola, "Metamaterials in electromagnetics," *Metamaterials*, vol. 1, no. 1, pp. 2–11, 2007.

[26] N. Mattiucci, M. Bloemer, N. Aközbek, and G. D'Aguanno, "Impedance matched thin metamaterials make metals absorbing," *Scientific Reports*, vol. 3, no. 1, pp. 1–11, 2013.

[27] M. Kadic, G. W. Milton, M. van Hecke, and M. Wegener, "3d metamaterials," *Nature Reviews Physics*, vol. 1, no. 3, pp. 198–210, 2019.

[28] S. M. Kamali, E. Arbabi, A. Arbabi, and A. Faraon, "A review of dielectric optical metasurfaces for wavefront control," *Nanophotonics*, vol. 7, no. 6, pp. 1041–1068, 2018.

[29] N. M. Estakhri and A. Alù, "Recent progress in gradient metasurfaces," *J. Opt. Soc. Am B*, vol. 33, no. 2, pp. A21–A30, 2016.

[30] S. Chang, X. Guo, and X. Ni, "Optical metasurfaces: progress and applications," *Annual Review of Materials Research*, vol. 48, pp. 279–302, 2018.

[31] B. Liu, K. Song, and J. Xiao, "Two-dimensional optical metasurfaces: From plasmons to dielectrics," *Advances in Condensed Matter Physics*, vol. 2019, 2019.

[32] R. Adato, A. A. Yanik, J. J. Amsden, D. L. Kaplan, F. G. Omenetto, M. K. Hong, S. Erramilli, and H. Altug, "Ultra-sensitive vibrational spectroscopy of protein monolayers with plasmonic nanoantenna arrays," *Proceedings of the National Academy of Sciences*, vol. 106, no. 46, pp. 19227–19232, 2009.

[33] P. Bharadwaj, B. Deutsch, and L. Novotny, "Optical antennas," *Advances in Optics and Photonics*, vol. 1, no. 3, pp. 438–483, 2009.

[34] V.-C. Su, C. H. Chu, G. Sun, and D. P. Tsai, "Advances in optical metasurfaces: fabrication and applications," *Optics Express*, vol. 26, no. 10, pp. 13148–13182, 2018.

[35] W. T. Chen and F. Capasso, "Will flat optics appear in everyday life anytime soon?," *Applied Physics Letters*, vol. 118, no. 10, p. 100503, 2021.

[36] Z. H. Jiang, S. Yun, L. Lin, J. A. Bossard, D. H. Werner, and T. S. Mayer, "Tailoring dispersion for broadband low-loss optical metamaterials using deep-subwavelength inclusions," *Scientific Reports*, vol. 3, no. 1, pp. 1–9, 2013.

[37] M. Khorasaninejad and F. Capasso, "Metalenses: Versatile multifunctional photonic components," *Science*, vol. 358, no. 6367, 2017.

[38] Y. Peng, *Numerical Study of Metalens*. PhD thesis, University of Michigan-Dearborn, 2018.

[39] W. Liu, H. Cheng, J. Tian, and S. Chen, "Diffractive metalens: from fundamentals, practical applications to current trends," *Advances in Physics: X*, vol. 5, no. 1, p. 1742584, 2020.

[40] W. T. Chen, A. Y. Zhu, V. Sanjeev, M. Khorasaninejad, Z. Shi, E. Lee, and F. Capasso, "A broadband achromatic metalens for focusing and imaging in the visible," *Nature Nanotechnology*, vol. 13, no. 3, pp. 220–226, 2018.

[41] Z.-B. Fan, H.-Y. Qiu, H.-L. Zhang, X.-N. Pang, L.-D. Zhou, L. Liu, H. Ren, Q.-H. Wang, and J.-W. Dong, "A broadband achromatic metalens array for integral imaging in the visible," *Light: Science & Applications*, vol. 8, no. 1, pp. 1–10, 2019.

[42] H. Zhou, L. Chen, F. Shen, K. Guo, and Z. Guo, "Broadband achromatic metalens in the midinfrared range," *Physical Review Applied*, vol. 11, no. 2, p. 024066, 2019.

[43] W. Liu, D. Ma, Z. Li, H. Cheng, D.-Y. Choi, J. Tian, and S. Chen, "Aberration-corrected three-dimensional positioning with a single-shot metalens array," *Optica*, vol. 7, no. 12, pp. 1706–1713, 2020.

[44] J. Engelberg and U. Levy, "The advantages of metalenses over diffractive lenses," *Nature Communications*, vol. 11, no. 1, pp. 1–4, 2020.

[45] Y. Yuan, B. Yao, J. Cao, X. Zang, D. Yu, A. V. Balakin, A. P. Shkurinov, and Y. Zhu, "Geometry phase for generating multiple focal points with different polarization states," *Optics Express*, vol. 28, no. 19, pp. 28452–28464, 2020.

[46] Y. Du, L. Shi, M. Hong, H. Li, D. Li, and M. Liu, "A surface plasmon resonance biosensor based on gold nanoparticle array," *Optics Communications*, vol. 298, pp. 232–236, 2013.

[47] J. Gosciniak, F. B. Atar, B. Corbett, and M. Rasras, "Plasmonic schottky photodetector with metal stripe embedded into semiconductor and with a cmos-compatible titanium nitride," *Scientific Reports*, vol. 9, no. 1, pp. 1–12, 2019.

[48] Y. Avitzour, Y. A. Urzhumov, and G. Shvets, "Wide-angle infrared absorber based on a negative-index plasmonic metamaterial," *Physical Review B*, vol. 79, no. 4, p. 045131, 2009.

[49] S. Haxha, F. AbdelMalek, F. Ouerghi, M. Charlton, A. Aggoun, and X. Fang, "Metamaterial superlenses operating at visible wavelength for imaging applications," *Scientific Reports*, vol. 8, no. 1, pp. 1–15, 2018.

[50] B. Wood, "Metamaterials and invisibility," *Comptes Rendus Physique*, vol. 10, no. 5, pp. 379–390, 2009.

[51] S. Kasani, K. Curtin, and N. Wu, "A review of 2d and 3d plasmonic nanostructure array patterns: fabrication, light management and sensing applications," *Nanophotonics*, vol. 8, no. 12, pp. 2065–2089, 2019.

[52] P. Andrew and W. Barnes, "Energy transfer across a metal film mediated by surface plasmon polaritons," *Science*, vol. 306, no. 5698, pp. 1002–1005, 2004.

[53] S. D. Gedney, "Introduction to the finite-difference time-domain (fdtd) method for electromagnetics," *Synthesis Lectures on Computational Electromagnetics*, vol. 6, no. 1, pp. 1–250, 2011.

[54] D. Sullivan, J. Liu, and M. Kuzyk, "Three-dimensional optical pulse simulation using the fdtd method," *IEEE transactions on microwave theory and techniques*, vol. 48, no. 7, pp. 1127–1133, 2000.

[55] M. Khorasaninejad, W. Chen, A. Zhu, J. Oh, R. Devlin, D. Rousso, and F. Capasso, "Multispectral chiral imaging with a metalens," *Nano Letters*, vol. 16, no. 7, pp. 4595–4600, 2016.

[56] M. Khorasaninejad, A. Y. Zhu, C. Roques-Carmes, W. T. Chen, J. Oh, I. Mishra, R. C. Devlin, and F. Capasso, "Polarization-insensitive metalenses at visible wavelengths," *Nano Letters*, vol. 16, no. 11, pp. 7229–7234, 2016.

[57] E. Bayati, A. Zhan, S. Colburn, M. V. Zhelyeznyakov, and A. Majumdar, "Role of refractive index in metalens performance," *Applied Optics*, vol. 58, no. 6, pp. 1460–1466, 2019.

[58] M. Khorasaninejad, W. T. Chen, R. C. Devlin, J. Oh, A. Y. Zhu, and F. Capasso, "Metalenses at visible wavelengths: Diffraction-limited focusing and subwavelength resolution imaging," *Science*, vol. 352, no. 6290, pp. 1190–1194, 2016.

[59] J. C. Gutiérrez-Vega, "Pancharatnam–berry phase of optical systems," *Optics Letters*, vol. 36, no. 7, pp. 1143–1145, 2011.

[60] M. Khorasaninejad and K. B. Crozier, "Silicon nanofin grating as a miniature chirality-distinguishing beam-splitter," *Nature Communications*, vol. 5, no. 1, pp. 1–6, 2014.

[61] M. K. Chen, Y. Wu, L. Feng, Q. Fan, M. Lu, T. Xu, and D. P. Tsai, "Principles, functions, and applications of optical meta-lens," *Advanced Optical Materials*, vol. 9, no. 4, p. 2001414, 2021.

[62] X. Fu, H. Liang, and J. Li, "Metalenses: from design principles to functional applications," *Frontiers of Optoelectronics*, pp. 1–17, 2021.

[63] Y. Ke, Y. Liu, J. Zhou, Y. Liu, H. Luo, and S. Wen, "Optical integration of pancharatnam-berry phase lens and dynamical phase lens," *Applied Physics Letters*, vol. 108, no. 10, p. 101102, 2016.

[64] F. Ali and S. Aksu, "A hybrid broadband metalens operating at ultraviolet frequencies," *Scientific Reports*, vol. 11, no. 1, pp. 1–8, 2021.

[65] H. Dong, F. Wang, R. Liang, Z. Wei, H. Meng, L.-H. Jiang, H. Cen, L. Wang, S. Qin, and C. Wang, "Visible-wavelength metalenses for diffraction-limited focusing of double polarization and vortex beams," *Optical Materials Express*, vol. 7, no. 11, pp. 4029–4037, 2017.

[66] S. Lipson, "Optical physics, 3rd edn," *Book Reviews*, vol. 38, no. 1, pp. 94–95, 1997.

[67] A. Arbabi, Y. Horie, A. J. Ball, M. Bagheri, and A. Faraon, "Subwavelength-thick lenses with high numerical apertures and large efficiency based on high-contrast transmitarrays," *Nature Communications*, vol. 6, no. 1, pp. 1–6, 2015.

[68] S. Banerji, M. Meem, A. Majumder, F. G. Vasquez, B. Sensale-Rodriguez, and R. Menon, "Imaging with flat optics: metalenses or diffractive lenses?," *Optica*, vol. 6, no. 6, pp. 805–810, 2019.

[69] Y. Liang, H. Liu, F. Wang, H. Meng, J. Guo, J. Li, and Z. Wei, "High-efficiency, near-diffraction limited, dielectric metasurface lenses based on crystalline titanium dioxide at visible wavelengths," *Nanomaterials*, vol. 8, no. 5, p. 288, 2018.

[70] E. Bayati, R. Pestourie, S. Colburn, Z. Lin, S. G. Johnson, and A. Majumdar, "Inverse designed metalenses with extended depth of focus," *ACS photonics*, vol. 7, no. 4, pp. 873–878, 2020.

[71] W. Liu, Z. Li, H. Cheng, C. Tang, J. Li, S. Zhang, S. Chen, and J. Tian, "Metasurface enabled wide-angle fourier lens," *Advanced Materials*, vol. 30, no. 23, p. 1706368, 2018.

[72] R. Paniagua-Dominguez, Y. F. Yu, E. Khaidarov, S. Choi, V. Leong, R. M. Bakker, X. Liang, Y. H. Fu, V. Valuckas, L. A. Krivitsky, *et al.*, "A metalens

with a near-unity numerical aperture," *Nano Letters*, vol. 18, no. 3, pp. 2124–2132, 2018.

[73] S. He, Z. Wang, Q. Liu, and W. Wang, "Study of focal shift effect in planar gan high contrast grating lenses," *Optics Express*, vol. 23, no. 23, pp. 29360–29368, 2015.

[74] Y. Yu and H. Zappe, "Theory and implementation of focal shift of plasmonic lenses," *Optics Letters*, vol. 37, no. 9, pp. 1592–1594, 2012.

[75] R. Ma, Y. Li, Y. Liu, Z. Yu, X. Long, L. Chen, D. Wu, and H. Ye, "Focal shift of nano-optical lens affected by periodic resonance with substrate," *IEEE Photonics Journal*, vol. 8, no. 6, pp. 1–9, 2016.

[76] S. Tian, H. Guo, J. Hu, and S. Zhuang, "Dielectric longitudinal bifocal metalens with adjustable intensity and high focusing efficiency," *Optics Express*, vol. 27, no. 2, pp. 680–688, 2019.

[77] A. Özdemir, N. Yılmaz, S. A. Alboon, Y. Takashima, and H. Kurt, "Analysis of the focusing crosstalk effects of broadband all-dielectric planar metasurface microlens arrays for ultra-compact optical device applications," *OSA Continuum*, vol. 1, no. 2, pp. 506–520, 2018.

[78] B. Hu, Q. J. Wang, and Y. Zhang, "Systematic study of the focal shift effect in planar plasmonic slit lenses," *Nanotechnology*, vol. 23, no. 44, p. 444002, 2012.

[79] Y. Gao, J. Liu, X. Zhang, Y. Wang, Y. Song, S. Liu, and Y. Zhang, "Analysis of focal-shift effect in planar metallic nanoslit lenses," *Optics Express*, vol. 20, no. 2, pp. 1320–1329, 2012.

[80] Y. Li, "A high-accuracy formula for fast evaluation of the effect of focal shift," *Journal of Modern Optics*, vol. 38, no. 9, pp. 1815–1819, 1991.

[81] M. Ye, V. Ray, D. Wu, and Y. S. Yi, "Metalens with artificial focus pattern," *IEEE Photonics Technology Letters*, vol. 32, no. 5, pp. 251–254, 2020.

[82] M. Kang, Y. Ra'di, D. Farfan, and A. Alù, "Efficient focusing with large numerical aperture using a hybrid metalens," *Physical Review Applied*, vol. 13, no. 4, p. 044016, 2020.

[83] F. Aieta, P. Genevet, M. A. Kats, N. Yu, R. Blanchard, Z. Gaburro, and F. Capasso, "Aberration-free ultrathin flat lenses and axicons at telecom wavelengths based on plasmonic metasurfaces," *Nano Letters*, vol. 12, no. 9, pp. 4932–4936, 2012.

[84] H. Yang, G. Li, G. Cao, Z. Zhao, F. Yu, X. Chen, and W. Lu, "Polarization-independent metalens constructed of antennas without rotational invariance," *Optics Letters*, vol. 42, no. 19, pp. 3996–3999, 2017.

[85] W. T. Chen, A. Y. Zhu, and F. Capasso, "Flat optics with dispersion-engineered metasurfaces," *Nature Reviews Materials*, vol. 5, no. 8, pp. 604–620, 2020.

[86] G. Zheng, H. Mühlenbernd, M. Kenney, G. Li, T. Zentgraf, and S. Zhang, "Metasurface holograms reaching 80% efficiency," *Nature Nanotechnology*, vol. 10, no. 4, pp. 308–312, 2015.

[87] P. Genevet, F. Capasso, F. Aieta, M. Khorasaninejad, and R. Devlin, "Recent advances in planar optics: from plasmonic to dielectric metasurfaces," *Optica*, vol. 4, no. 1, pp. 139–152, 2017.

[88] P. Zhang, Y. Tan, W. Liu, and W. Chen, "Methods for optical phase retardation measurement: a review," *Science China Technological Sciences*, vol. 56, no. 5, pp. 1155–1164, 2013.

[89] A. Wang, Z. Chen, and Y. Dan, "Planar metalenses in the mid-infrared," *AIP Advances*, vol. 9, no. 8, p. 085327, 2019.

[90] M. Born and E. Wolf, *Principle of optics, 1999*. Cambridge University Press, New York.

[91] S. Wang, E. Bernabeu, and J. Alda, "Unified and generalized fresnel numbers," *Optical and Quantum Electronics*, vol. 24, no. 12, pp. 1351–1358, 1992.

[92] J. W. Goodman, "Introduction to fourier optics, roberts & co," *Publishers, Englewood, Colorado*, 2005.

[93] H. Dong, F. Wang, R. Liang, Z. Wei, H. Meng, L.-H. Jiang, H. Cen, L. Wang, S. Qin, and C. Wang, "Visible-wavelength metalenses for diffraction-limited focusing of double polarization and vortex beams," *Optical Materials Express*, vol. 7, no. 11, pp. 4029–4037, 2017.

[94] N. Yu, P. Genevet, M. A. Kats, F. Aieta, J.-P. Tetienne, F. Capasso, and Z. Gaburro, "Light propagation with phase discontinuities: generalized laws of reflection and refraction," *Science*, vol. 334, no. 6054, pp. 333–337, 2011.

[95] H. Chung and O. D. Miller, "High-na achromatic metalenses by inverse design," *Optics Express*, vol. 28, no. 5, pp. 6945–6965, 2020.

[96] R. N. Day and M. W. Davidson, "The fluorescent protein palette: tools for cellular imaging," *Chemical Society Reviews*, vol. 38, no. 10, pp. 2887–2921, 2009.

[97] A. D. Ludlow, M. M. Boyd, J. Ye, E. Peik, and P. O. Schmidt, "Optical atomic clocks," *Reviews of Modern Physics*, vol. 87, no. 2, p. 637, 2015.

[98] L. Guo, S. Xu, R. Wan, T. Li, L. Xiong, L. Wang, and W. Zhu, "Design of aluminum nitride metalens in the ultraviolet spectrum," *Journal of Nanophotonics*, vol. 12, no. 4, p. 043513, 2018.

[99] J.-S. Park, S. Zhang, A. She, W. T. Chen, P. Lin, K. M. Yousef, J.-X. Cheng, and F. Capasso, "All-glass, large metalens at visible wavelength using deep-

ultraviolet projection lithography," *Nano Letters*, vol. 19, no. 12, pp. 8673–8682, 2019.

[100] N. Ravindra, P. Ganapathy, and J. Choi, "Energy gap–refractive index relations in semiconductors–an overview," *Infrared Physics & Technology*, vol. 50, no. 1, pp. 21–29, 2007.

[101] S. Kanwal, J. Wen, B. Yu, X. Chen, D. Kumar, Y. Kang, C. Bai, S. Ubaid, and D. Zhang, "Polarization insensitive, broadband, near diffraction-limited metalens in ultraviolet region," *Nanomaterials*, vol. 10, no. 8, p. 1439, 2020.

[102] L. Guo, Z. Hu, R. Wan, L. Long, T. Li, J. Yan, Y. Lin, L. Zhang, W. Zhu, and L. Wang, "Design of aluminum nitride metalens for broadband ultraviolet incidence routing," *Nanophotonics*, vol. 8, no. 1, pp. 171–180, 2019.

[103] M. Khorasaninejad, A. Y. Zhu, C. Roques-Carmes, W. T. Chen, J. Oh, I. Mishra, R. C. Devlin, and F. Capasso, "Polarization-insensitive metalenses at visible wavelengths," *Nano Letters*, vol. 16, no. 11, pp. 7229–7234, 2016.

[104] S. Kanwal, J. Wen, B. Yu, X. Chen, D. Kumar, Y. Kang, C. Bai, S. Ubaid, and D. Zhang, "Polarization insensitive, broadband, near diffraction-limited metalens in ultraviolet region," *Nanomaterials*, vol. 10, no. 8, p. 1439, 2020.

[105] Z. Shen, S. Zhou, X. Li, S. Ge, P. Chen, W. Hu, and Y. Lu, "Liquid crystal integrated metalens with tunable chromatic aberration," *Advanced Photonics*, vol. 2, no. 3, p. 036002, 2020.

[106] W. T. Chen, A. Y. Zhu, V. Sanjeev, M. Khorasaninejad, Z. Shi, E. Lee, and F. Capasso, "A broadband achromatic metalens for focusing and imaging in the visible," *Nature Nanotechnology*, vol. 13, no. 3, pp. 220–226, 2018.

[107] M. Kang, Y. Ra'di, D. Farfan, and A. Alù, "Efficient focusing with large numerical aperture using a hybrid metalens," *Physical Review Applied*, vol. 13, no. 4, p. 044016, 2020.

[108] Y. Bao, Q. Jiang, Y. Kang, X. Zhu, and Z. Fang, "Enhanced optical performance of multifocal metalens with conic shapes," *Light: Science & Applications*, vol. 6, no. 10, pp. e17071–e17071, 2017.

[109] X. Chen, M. Chen, M. Q. Mehmood, D. Wen, F. Yue, C.-W. Qiu, and S. Zhang, "Longitudinal multifoci metalens for circularly polarized light," *Advanced Optical Materials*, vol. 3, no. 9, pp. 1201–1206, 2015.

[110] C. Williams, Y. Montelongo, and T. D. Wilkinson, "Plasmonic metalens for narrowband dual-focus imaging," *Advanced Optical Materials*, vol. 5, no. 24, p. 1700811, 2017.

[111] Q. Chen, Y. Li, Y. Han, D. Deng, D. Yang, Y. Zhang, Y. Liu, and J. Gao, "High numerical aperture multifocal metalens based on pancharatnam–berry phase optical elements," *Applied Optics*, vol. 57, no. 27, pp. 7891–7894, 2018.

[112] R. Lin and X. Li, "Multifocal metalens based on multilayer pancharatnam–berry phase elements architecture," *Optics Letters*, vol. 44, no. 11, pp. 2819–2822, 2019.

[113] B. Huang, W. Bai, H. Jia, J. Han, P. Guo, J. Wu, and J. Yang, "Multifocal coplane metalens based on computer-generated holography for multiple visible wavelengths," *Results in Physics*, vol. 17, p. 103085, 2020.

[114] E. D. Palik, *Handbook of optical constants of solids*, vol. 3. Academic press, 1998.

[115] S. Kanwal, J. Wen, B. Yu, D. Kumar, X. Chen, Y. Kang, C. Bai, and D. Zhang, "High-efficiency, broadband, near diffraction-limited, dielectric metalens in ultraviolet spectrum," *Nanomaterials*, vol. 10, no. 3, p. 490, 2020.

[116] Z. Shen, L. Su, X.-C. Yuan, and Y.-C. Shen, "Trapping and rotating of a metallic particle trimer with optical vortex," *Applied Physics Letters*, vol. 109, no. 24, p. 241901, 2016.

[117] P. L. POLAVARAPU and J. HE, "Chiral analysis using mid-ir vibrational cd spectroscopy," *Analytical Chemistry (Washington, DC)*, vol. 76, no. 3, pp. 61A–67A, 2004.

[118] W. A Paiva-Marques, F. Reyes Gómez, O. N Oliveira, and J. R. Mejía-Salazar, "Chiral plasmonics and their potential for point-of-care biosensing applications," *Sensors*, vol. 20, no. 3, p. 944, 2020.

[119] E. Hendry, T. Carpy, J. Johnston, M. Popland, R. Mikhaylovskiy, A. Lapthorn, S. Kelly, L. Barron, N. Gadegaard, and M. Kadodwala, "Ultrasensitive detection and characterization of biomolecules using superchiral fields," *Nature Nanotechnology*, vol. 5, no. 11, pp. 783–787, 2010.

[120] J. McConathy and M. J. Owens, "Stereochemistry in drug action," *Primary Care Companion to the Journal of Clinical Psychiatry*, vol. 5, no. 2, p. 70, 2003.

[121] K. Singh, P. Shakya, A. Kumar, S. Alok, M. Kamal, and S. Singh, "Stereochemistry and its role in drug design," *International Journal of Pharmaceutical Sciences and Research*, vol. 5, no. 11, pp. 4644–4659, 2014.

[122] V. E. Bochenkov and T. I. Shabatina, "Chiral plasmonic biosensors," *Biosensors*, vol. 8, no. 4, p. 120, 2018.

[123] S. M. Kelly, T. J. Jess, and N. C. Price, "How to study proteins by circular dichroism," *Biochimica et Biophysica Acta (BBA)-Proteins and Proteomics*, vol. 1751, no. 2, pp. 119–139, 2005.

[124] A. G. Mark, J. G. Gibbs, T.-C. Lee, and P. Fischer, "Hybrid nanocolloids with programmed three-dimensional shape and material composition," *Nature Materials*, vol. 12, no. 9, pp. 802–807, 2013.

[125] S. Zu, Y. Bao, and Z. Fang, "Planar plasmonic chiral nanostructures," *Nanoscale*, vol. 8, no. 7, pp. 3900–3905, 2016.

[126] M. Schaferling, N. Engheta, H. Giessen, and T. Weiss, "Reducing the complexity: Enantioselective chiral near-fields by diagonal slit and mirror configuration," *ACS Photonics*, vol. 3, no. 6, pp. 1076–1084, 2016.

[127] T. Wu, J. Ren, R. Wang, and X. Zhang, "Competition of chiroptical effect caused by nanostructure and chiral molecules," *The Journal of Physical Chemistry C*, vol. 118, no. 35, pp. 20529–20537, 2014.

[128] Y. Tang and A. E. Cohen, "Optical chirality and its interaction with matter," *Physical Review Letters*, vol. 104, no. 16, p. 163901, 2010.

[129] S. Yoo and Q.-H. Park, "Metamaterials and chiral sensing: a review of fundamentals and applications," *Nanophotonics*, vol. 8, no. 2, pp. 249–261, 2019.

[130] M. Schaferling, X. Yin, N. Engheta, and H. Giessen, "Helical plasmonic nanostructures as prototypical chiral near-field sources," *ACS Photonics*, vol. 1, no. 6, pp. 530–537, 2014.

[131] S. K. Kailasa, J. R. Koduru, M. L. Desai, T. J. Park, R. K. Singhal, and H. Basu, "Recent progress on surface chemistry of plasmonic metal nanoparticles for colorimetric assay of drugs in pharmaceutical and biological samples," *TrAC Trends in Analytical Chemistry*, vol. 105, pp. 106–120, 2018.

[132] A. Kakkanattu, N. Eerqing, S. Ghamari, and F. Vollmer, "Review of optical sensing and manipulation of chiral molecules and nanostructures with the focus on plasmonic enhancements," *Optics Express*, vol. 29, no. 8, pp. 12543–12579, 2021.

[133] W. Wang, L. V. Besteiro, T. Liu, C. Wu, J. Sun, P. Yu, L. Chang, Z. Wang, and A. O. Govorov, "Generation of hot electrons with chiral metamaterial perfect absorbers: giant optical chirality for polarization-sensitive photochemistry," *ACS Photonics*, vol. 6, no. 12, pp. 3241–3252, 2019.

[134] W. Li, Z. J. Coppens, L. V. Besteiro, W. Wang, A. O. Govorov, and J. Valentine, "Circularly polarized light detection with hot electrons in chiral plasmonic metamaterials," *Nature Communications*, vol. 6, no. 1, pp. 1–7, 2015.

[135] L. K. Khorashad, L. V. Besteiro, M. A. Correa-Duarte, S. Burger, Z. M. Wang, and A. O. Govorov, "Hot electrons generated in chiral plasmonic nanocrystals as a mechanism for surface photochemistry and chiral growth," *Journal of the American Chemical Society*, vol. 142, no. 9, pp. 4193–4205, 2020.

[136] E. Mohammadi, K. Tsakmakidis, A.-N. Askarpour, P. Dehkhoda, A. Tavakoli, and H. Altug, "Nanophotonic platforms for enhanced chiral sensing," *ACS Photonics*, vol. 5, no. 7, pp. 2669–2675, 2018.

[137] L. D. Barron, *Molecular light scattering and optical activity*. Cambridge University Press, 2009.